ISSN 1854-0171

ACTA GEOTECHNICA SLOVENICA

2017/1
VOL. 14

ISSN: 1854-0171

ACTA GEOTECHNICA SLOVENICA

Ustanovitelji | Founders

Univerza v Mariboru, Fakulteta za gradbeništvo, prometno inženirstvo in arhitekturo
University of Maribor, Faculty of Civil Engineering, Transportation Engineering and Architecture

Univerza v Ljubljani, Fakulteta za gradbeništvo in geodezijo
University of Ljubljana, Faculty of Civil and Geodetic Engineering

Univerza v Ljubljani, Naravoslovnotehniška fakulteta
University of Ljubljana, Faculty of Natural Sciences and Engineering

Slovensko geotehniško društvo
Slovenian Geotechnical Society

Društvo za podzemne in geotehniške konstrukcije
Society for Underground and Geotechnical Constructions

Izdajatelj | Publisher

Univerza v Mariboru, Fakulteta za gradbeništvo, prometno inženirstvo in arhitekturo
Faculty of Civil Engineering, Transportation Engineering and Architecture

Odgovorni urednik | Editor–in–Chief

Bojana Dolinar — University of Maribor

Uredniki | Co–Editors

Jakob Likar	Geoportal d.o.o.
Janko Logar	University of Ljubljana
Borut Macuh	University of Maribor
Stanislav Škrabl	University of Maribor
Milivoj Vulić	University of Ljubljana
Bojan Žlender	University of Maribor

Posvetovalni uredniki | Advisory Editors

Heinz Brandl	Vienna University of Technology
Chandrakant. S. Desai	University of Arizona
Bojan Majes	University of Ljubljana
Pedro Seco e Pinto	National Laboratory of Civil Eng.

Lektor | Proof–Reader

Paul McGuiness

Naklada | Circulation

200 izvodov - issues

Cena | Price

25 EUR/letnik - 25 EUR/vol.; (50 EUR for institutions/za institucije)

Tisk | Print

Tiskarna Saje

Revija redno izhaja dvakrat letno. Članki v reviji so recenzirani s strani priznanih mednarodnih strokovnjakov. Baze podatkov v katerih je revija indeksirana: SCIE - Science Citation Index Expanded, JCR – Journal Citation Reports / Science Edition, ICONDA - The international Construction database, GeoRef. Izid publikacije je finančno podprla Javna agencija za raziskovalno dejavnost Republike Slovenije iz naslova razpisa za sofinanciranje domačih periodičnih publikacij.

Naslov uredništva | Address

ACTA GEOTECHNICA SLOVENICA
Univerza v Mariboru, Fakulteta za gradbeništvo, prometno inženirstvo in arhitekturo
Smetanova ulica 17, 2000 Maribor, Slovenija
Telefon / Telephone: +386 (0)2 22 94 300
Faks / Fax: +386 (0)2 25 24 179
E-pošta / E-mail: ags@uni-mb.si

Spletni naslov | web Address

http://www.fg.uni-mb.si/journal-ags/

The journal is published twice a year. Papers are peer reviewed by renowned international experts. Indexation data bases of the journal: SCIE - Science Citation Index Expanded, JCR – Journal Citation Reports / Science Edition, ICONDA- The international Construction database, GeoRef. The publication was financially supported by Slovenian Research Agency according to the Tender for co-financing of domestic periodicals.

KONTROLA KVALITETE PRI GRADNJI NASIPOV IZ JALOVINE

Wojciech Tschuschke
Poznan University of Life Sciences,
Institute of Construction and Geoengineering
Wojska Polskiego 28, 60-637 Poznań, Poljska

Magdalena Wróżyńska *(vodilni avtor)*
Poznan University of Life Sciences,
Institute of Construction and Geoengineering
Wojska Polskiego 28, 60-637 Poznań, Poljska
E-pošta: mwalczak@up.poznan.pl

Jędrzej Wierzbicki
Adam Mickiewicz University,
Institute of Geology
Maków Polnych 16, 61-606 Poznań, Poljska

Ključne besede

flotacijski sedimenti, jezovi iz jalovine, geotehnični kontrolni preizkusi

Izvleček

Rudarska industrija dnevno proizvaja velike količine rudarske jalovine. Pri izkoriščanju bakrove rude na Poljskem ostanki po flotaciji predstavljajo 95 % izkopane hribine, vsi ti ostanki so deponirani na odlagališča, ki so podprta z zunanjimi jezovi. Trajnost in stabilnost teh zemljinskih objektov je odločilno za varno delovanje celotnega objekta. Izbira ustrezne kakovosti zemljin za gradnjo jezov predstavlja ključni dejavnik za omejevanje tveganja njegove potencialne porušitve. Zelo veliki depoji zahtevajo zadostno velike količine zemljine za gradnjo nasipov. Alternativa temu klasičnemu pristopu predstavlja uporaba odložene jalovine. Pri tej rešitvi se zniža količina rudniških odpadkov, ki so shranjeni v depojih jalovine, ni treba izkoriščati nahajališča naravnih zemljin in poveča se potencialna kapaciteta predvidenih depojev. Prispevek prikazuje principe tehnologije gradnje jezov za akumuliranje vode; kriterije za izbiro primerne granulacije zemljin in fizikalnih parametrov sedimentov za uporabo v gradnji jezov; principe kontrole kvalitete za zemeljska dela; in metodologijo geotehničnih kontrolnih preizkusov. Prav tako so razloženi učinki uporabljene tehnologije na stanje naravnega okolja.

QUALITY CONTROL FOR THE CONSTRUCTION OF A TAILINGS DAM

Wojciech Tschuschke
Poznan University of Life Sciences,
Institute of Construction and Geoengineering
Wojska Polskiego 28, 60-637 Poznań, Poland

Magdalena Wróżyńska *(corresponding author)*
Poznan University of Life Sciences,
Institute of Construction and Geoengineering
Wojska Polskiego 28, 60-637 Poznań, Poland
E-mail: mwalczak@up.poznan.pl

Jędrzej Wierzbicki
Adam Mickiewicz University,
Institute of Geology
Maków Polnych 16, 61-606 Poznań, Poland

Keywords

post-flotation sediments; tailings dams; geotechnical control tests

Abstract

Every day the mining industry produces large amounts of mine tailings. In the case of copper ores exploited in Poland, the post-flotation tailings constitute 95% of the excavated rock and all the tailings are deposited in dumps, which are supported by outer dams. The durability and stability of these earth structures determine the safe operation of the entire object. The selection of adequate-quality soils for the construction of the dams is a crucial factor limiting the risk of its potential failure. Very large depositories require sufficiently large amounts of soil for the construction of the dams. An alternative to this classic approach is the use of the deposited tailings. In this solution the amount of mine wastes stored in the depository is reduced, there is no need to exploit the deposits of natural soils and the potential capacity of the depository increases. This paper presents the principles of the construction technology for hydraulically filled dams; the criteria for the selection of proper soil gradation and the physical properties of the sediments to be used in the construction of the dams; the principles of quality control for earth works; and the methodology of the geotechnical control tests. The effects of the applied technology on the condition of the natural environment are also discussed.

1 INTRODUCTION

Competent waste management in accordance with legal regulations at the site of their deposition is a priority for properly managed and exploited waste depositories. This problem becomes particularly significant when deposited waste products can be economically re-used. Such a situation occurs, e.g., in the case of wastes classified as neutral to the environment. The category of such wastes frequently includes mining wastes, distinguished by two indicators: varied composition, dependent on the site and technology of the produced tailings, and their considerable volume. In open-pit mines it is most typically overburden soil removed from the layers over the deposit, while in deep mines it is the output coming from the construction of the mine and the exploitation of the deposit. Thus, formally the suitability of this output as engineering construction material should be similar to that of natural soils. However, in practice the material after its processing differs from the material deposited into the dump with regard to its strength. A key element of this change results from the fact that the rock material of the continuous structure changes after crushing into granular three-phase material. A very good example of such material is provided by post-flotation tailings from copper ore processing. The utilization of post-flotation tailings as a construction material suitable for earth

structures on the one hand requires a determination of its index and strength properties, and on the other the identification of the type, purpose and parameters of the structure, where the material is to be used.

The aim of this paper is to define the physical criteria for evaluating the quality of tailings used to construct dams based on strength criteria. As a result a new approach for the quality assessment is proposed in terms of a relationship between the relative density and compaction index for the tailings [3].

1 THE OBJECT

Poland is a world-leading producer of copper and silver, exploiting non-ferrous metal ores located in the south-western part of the country, where the entire copper-ore mining and processing industry is found. The output from all the deep mines is subjected first to mechanical treatment and next to the flotation processes, the product of which is copper concentrate and post-flotation wastes, which need to be properly managed. On the global scale post-flotation tailings constitute approximately 95% of the excavated deposit, which due to the volume of production results in the need to manage approximately 25 million Mg waste annually. Starting from 1997 all post-flotation tailings are transported to a single depository, which has recently been officially named the Żelazny Most Mining Tailings Storage Facility (OUOW Żelazny Most). The amount of wastes deposited over the years of the facility's operation has resulted in the construction of a hydro-engineering mega-structure, the second (after the Chinese Great Wall) engineering structure seen from space.

The size of the object is indicated by its parameters: the amount of deposited tailings – over 500 million m^3; storage area – 14 km^2; the capacity of the tailings pond - 7 million m^3; the length of the dams surrounding the depository – 14.3 km; and the height of the highest dams – over 60 m (Fig. 1). Post-flotation tailings are transported to the depository by the hydraulic method, first under pressure and then by gravity, in the form of a soil-water mixture with a density of 1.11–1.15 Mg/m^3. The wastes mixture is discharged into the depository from pipelines located on the crests of the external dams surrounding the depository (Fig. 2). After the discharge the coarse particles settle on the beach, whereas the finer ones flow with water towards the pond located in the central part of the depository. Due to sedimentation of the finer material in the pond the cleaned water is captured by intake towers and transported back to the mines to the secondary technological cycle. Guidelines

Figure 1. General view of the OUOW Żelazny Most [KGHM Polska Miedź S.A.].

Figure 2. Spigotting of post-flotation tailings at the Żelazny Most depository.

for the safe operation of the depository require the maintenance of the water line at a minimum distance of 200 m from the dam crest, which determines the beach slope, naturally oscillating around 1%.

Tailings are always discharged into the depository beach within one of the 26 separated alluvial fan sections from outlet pipes of 20 cm in diameter, located 20 m from one another (Fig. 2). As was shown in practice, such a spacing of discharge pipes ensures a uniform coverage of the beach with the discharged tailings.

The development of the depository is based on the upstream method, constructing the higher embankments on the spigotted beaches. The new embankments are formed using tailings deposited on the beaches near the dams [11]. The height of the embankments amounts to 2.5 m and it is adapted to the re-arrangement of the spigotting pipelines. The annual increase of the dam height is on average 1.3 m [3].

2 CHARACTERISTICS OF THE DEPOSITED TAILINGS

Post-flotation tailings produced from ores genetically connected with dolomites and copper shales are characterized by a considerable grain angularity, while those from sandstones have a finer morphology or even a preserved original grain shape in deposits with a weaker binder. The basic component of the fraction of less than 0.06 mm comprises chips of carbonate rocks, while in the coarser fraction of quartz is the dominant material, occurring mostly in the fraction of 0.25–0.1 mm. The shale content decreases with a reduction of the grain diameter. The characteristics of the tailings connected with their original geomorphology determine the mechanical properties of the material to be used in the construction of earth dams.

The tailings that are gravitationally spigotted on the beach undergo the natural process of sedimentation segregation, as a result of which coarser fractions are deposited in the vicinity of the tailing-discharge sites, while finer fractions flow with water over the surface of the beach towards the pond. The finest tailings (carbonate-clay tailings) are excluded from the spigotting process, as material that cannot be used for the construction of the embankments. These wastes are discharged directly inside the depository to seal the bottom of the pond. The spigotting of the tailings is a cyclic process, in which a fragment of the beach is elevated by several dozen centimetres at a time. Then the beach undergoes a drying stage, lasting up to 2 months, followed by another spigotting process. The technology of the hydraulic transport of the tailings to the depository, spigotting of the beach, the process of drainage, drying and beach formation cause significant effects, i.e., the spatial heterogeneity of the tailings' compaction and specific macrostructure characterized by horizontal laminations. The number and thickness of the laminations with the finest grains increase with the distance from the dams, limiting the range of the sedimentation zone for deposits suitable for the rise of the dams. Sediments deposited in that zone have to meet specific compactibility criteria, and as a consequence, also the bearing capacity, since they additionally form the subsoil for new embankments constructed by the upstream method [2]. A diagram for the depository section with an arbitrary division into zones and grading envelopes for the Żelazny Most depository is presented in Figs. 3 and 4.

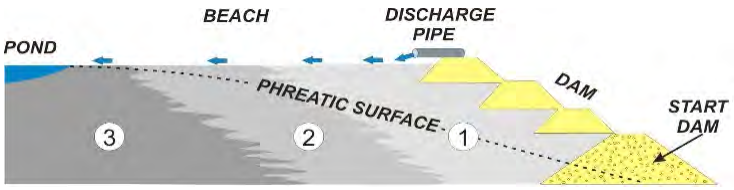

Figure 3. Diagram of a section of a depository fragment divided into tailings-sedimentation zones differing in grain size (zone 1 – coarse tailings, zone 2 – mixed sand-silty deposits, zone 3 – fine tailings and slimes).

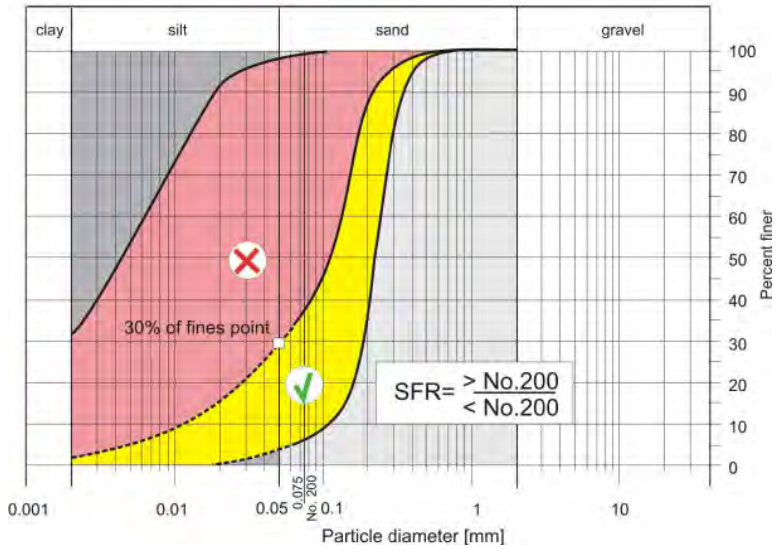

Figure 4. Areas of particle size variation in deposited tailings divided into suitable waste (d_{30} > 0.05 mm) and inadequate waste (d_{30} < 0.05 mm) for dam construction.

3 CRITERIA FOR THE SELECTION OF MATERIAL FOR THE DAM CONSTRUCTION

Due to the necessity to continuously increase the depository capacity, the processes of engineering design, tailings deposition and dam construction are realized in parallel. The adopted method of upstream development results in a situation when only the starter dams made from natural soils are founded on the subsoil. Successive stages of the development are realized from drained sediments deposited on beaches. The design of the depository development requires the geotechnical identification of the deposited sediments. The geotechnical parameters of the sediments change with the distance from the dams, while they also depend on the type of rock from which they originate, the applied processing, the disposal technology, the seepage and the consolidation processes. Only some of the deposited sediments can be used as a construction material for new higher embankments. Extremely fine silty deposits exhibit the properties of a plastic material with limited shear strength [2]. Sandy deposits have the characteristics of a non-cohesive material with much greater rigidity and shear strength. Such materials can be well described by compactibility indexes. Assuming the strength criterion as the starting point for the determination of the suitability of deposits for construction purposes, a series of tests was performed in a direct shear apparatus at a sediment compaction corresponding to the maximum dry density from the Proctor test, Fig. 5. Samples of sediments were differentiated in terms of their grain size distribution, identified by the *SFR* (ratio of sand to fines < 0.074mm), according to the ASTM standard [4]. The correlation was identified on the basis of model tests between the internal friction angle, determined in a direct shear apparatus, and the grain size parameter *SFR* used in the determination of the physical criterion of sediment suitability, Fig. 6.

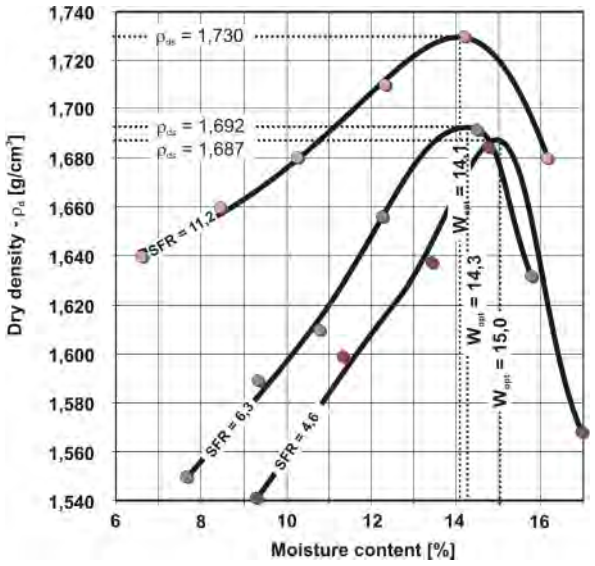

Figure 5. Example curves of the compactibility for post-flotation tailings from the Proctor test (ρ_{ds} - maximum dry density, w_{opt} – optimum moisture content).

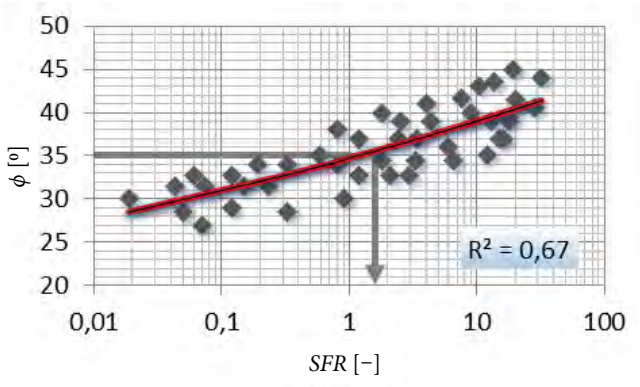

Figure 6. Correlation between the internal friction angle (ϕ) and the *SFR* coefficient for compacted tailings at a natural moisture content equal ±5% of the optimum moisture content.

Samples of post-flotation tailings were compacted at a moisture content similar to the optimal moisture content (typically slightly lower) and as was shown in this analysis, this factor had no significant effect on the low value of the coefficient of determination of equation 1. Factors having a significant effect on the values of the internal friction angle of the deposits with a specific grain size expressed by the *SFR* value are other grain size parameters, e.g., the coefficient of uniformity and the genesis of the deposits.

This dependence can be presented using the following equation (1).

$$\phi = 34.71 \cdot SFR^{0.05} \qquad (1)$$

Relatively high values of the internal friction angles result from the high angularity of the sediment grains. On the basis of the stability analysis it can be assumed that in order to meet the strength criterion ($\phi > 35^0$) at the required compaction, the sediments embedded in the dams should have *SFR* > 2, which corresponds to a limitation of the silt content in the sediments up to 30%.

The area of grain size variability in sediments classified as suitable for dam construction is presented in Fig. 4.

The identification of the distribution and the potential prediction of changes in sediment grain size in the beach profile and cross-section is the basic information for the

selection of the sediment for the construction of dams and a determination of the geotechnical parameters for an analysis of object stability. The process of sediment deposition results in a situation when the hydraulically filled beach is a heterogeneous medium of random character. Identification of the grain size of the sediments, being a function of the location in space, can be considered as a deterministic problem for a heterogeneous medium [7]. The probability of the occurrence of sediments with varying grain size at a specific distance from the dam can be investigated by clustering sediments into groups with a similar grain size or by the so-called continuous distribution method for one of the adopted measures of the grain size distribution curve, Fig. 7, [6], [1], [7] and [8]. It results from the analysis of Fig. 7 that the previously determined gradation criterion (sand content > 70%) is met by sediments deposited in the zone of the beach adjacent to the dam at a distance of up to 200 m (the yellow zone in Fig. 7). Thus, it was this zone of the beach that was designated as a potential zone for earth works, from which the sediments may be used for dam construction. An advantage of the earth

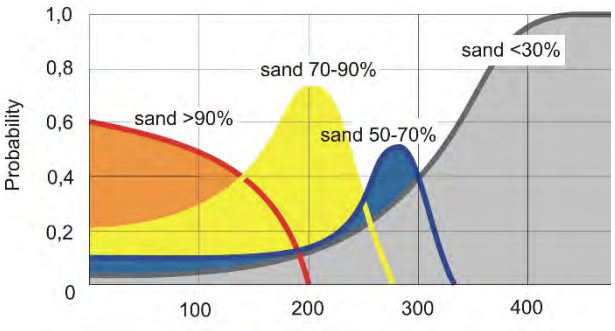

Figure 7. Probability of grain size distribution of tailings deposited on the depository beach depending on the distance from the discharge location.

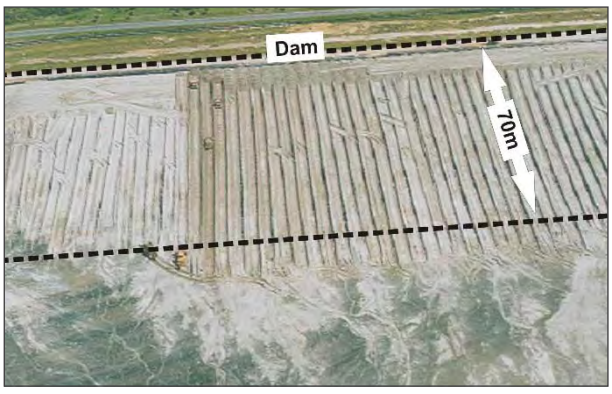

Figure 8. A fragment of the formed beach with the separated zone of deposits suitable for embedding in the dam. The view of the zone of tailings used for dam construction.

work in the identified zone of the beach is the mixing of sediments with different grain sizes, together with the elimination of laminations of cohesive deposits formed in the course of hydraulic filling and compaction of the subsoil for future embankments.

The conditions specified above for the construction of dams from the material deposited in the depository constituted the basis for the development of a procedure defining the manner and sequence of operations:

- Spigotting of a specified fragment of the beach with post-flotation tailings,
- Drainage and drying of deposited sediments in the beach to a moisture content corresponding to the optimal moisture content,
- Collection of hydraulically deposited sediments from a beach section of 70 m in width by bulldozers (at this stage the beach is further compacted for the successive stages of the dam's construction), (Fig. 8).
- Formation of a 0.5-m-thick layer of a new embankment,
- Compaction of the formed layer using a vibrating roll until the required compaction criterion is met,
- Quality control of the performed earth work,
- A repetition of the entire cycle until the complete module of the 2.5-m-high embankment is obtained, together with the final geotechnical acceptance test.

4 QUALITY CONTROL OF PERFORMED EARTH WORKS

The structures of high, hydraulically filled dams from post-flotation tailings surrounding the object require a strict observation of the technological regime and particularly careful quality-control tests of the performed earth work.

Meeting the criteria of the grain size distribution and compaction of the material built in the dam is a necessary pre-condition for the safe operation of the object, guaranteeing its stability and durability. Within the framework of control tests, testing is performed on an on-going basis by the surface method after the formation and compaction of a successive layer of 0.5 m in thickness and the final verification tests by the penetration test after the completion of the construction stage of the 2.5-m-high embankment. The surface tests are based on standard methods, i.e., isotope and volumetric tests [10]. In the isotope method the moisture content and the density of sediments in the controlled layer are determined and, as a consequence, its relative compaction index – R (dry density – ρ_d to maximum dry density – ρ_{ds}), (Fig. 5). In the latter method laboratory

analyses of the physical parameters are performed on the collected sediment samples, and together with the Proctor test results (Fig. 5) they enable a determination of the relative compaction and additionally a verification of the grain size criterion. An original solution in this respect is provided by the cone-penetration test CPT, [5] and [7]. In this method the penetration characteristics are recorded, i.e., the cone resistance - q_c and the friction ratio - R_f, which are indicators for the assessment of the relative density – D_r and the grain size in sediments over the entire analysed profile. The sediments embedded in the dams meet the compaction criterion, when the condition described by equation 2 is met, which can also be clearly seen on the q_c plot (parts of the q_c profile in Fig. 9, above the red line, representing equation (2)).

for $D_r > 70\%$:

$$q_c > \exp\left(\left(36.81 \cdot \ln\left(\sigma_{v0}\right) + 733\right) / \left(17 \cdot \sigma_{v0}^{0.0876}\right)\right) \qquad (2)$$

where: q_c – cone resistance and σ_{v0} –total vertical stress.

To verify the measures of sediment compaction it is possible to evaluate the relative compaction index - R by the relative density – D_r on the basis of a correlation dependence expressed by equation (3), [9].

$$R = 0.769 + 0.231 \cdot D_r \qquad (3)$$

where: R – relative compaction index and D_r – relative density.

The required criterion for the sediment grain size distribution (silt content < 30%) expressed by the CPT parameters is determined by the condition $R_f < 1.3\%$, [5] and [7]. In contrast, the area limited by the criterion $R_f < 1.3\%$ meets the grain size distribution criteria (below the red line in the parts of the R_f diagram).

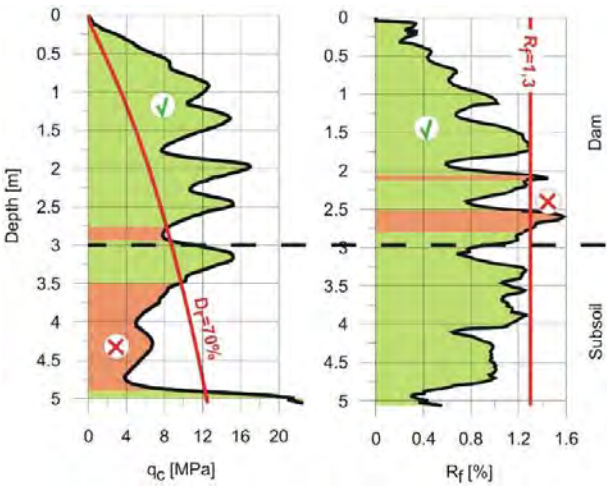

Figure 9. CPT results at the background of the quality criterion.

An example of the interpretation of the CPT results in order to identify the grain size distribution and the relative density of sediments in the profile of the new embankment is presented in Fig. 9.

It should be noted that the application of the commonly used CPT soil-behaviour charts to the quality control of the dam construction does not yield the expected results due to the specific grain size distribution and the mineral composition of the tested sediments, [7].

5 THE IMPACT OF THE DAM-DEVELOPMENT TECHNOLOGY ON THE NATURAL ENVIRONMENT

From the point of view of the environmentally safe operation of the Żelazny Most Mining Tailings Storage Facility the following important problems should be addressed [11], [2]:

- Assurance of the object's stability,
- Limitation of the migration of contaminated saline waters from the depository to the ground waters,
- Limitation of dusting.

In the case of the first two problems the applied technology of a gradual rise of the dams by the construction of higher embankments from post-flotation tailings previously deposited in the depository does not generally differ from the conventional methods of dam construction. In the case of a risk of stability loss, in the threatened sections of the dam, the loading berms are constructed. The migration of saline waters from the depository to the subsoil is reduced thanks to the construction of a comprehensive drainage system consisting of multi-floor circumferential drainage, drainage of the starter dam, drainage ditches at the dam toe and finally the barrier of deep-drainage wells at the close forefield. In contrast to the previous aspects, the hazard connected with dusting is a specific characteristic of the Żelazny Most facility. Post-flotation tailings deposited on the beach and used in the dam construction are characterized by the capacity to dry rapidly. Dry sediments, free of the binding force, are exposed to the action of wind and are easily transported outside the depository area, forming fine dust that is suspended in the air. The impact of dust on the environment is so intense that as a counter-measure the surfaces of the beach and the dams are covered with an air-sprayed bituminous emulsion supplemented by water curtains activated during strong winds.

6 CONCLUDING REMARKS

The presented technology of a gradual stage construction of the dams from post-flotation tailings deposited with wet disposal technology has at least one spectacular economic advantage. The use of wastes for the formation of dams on one hand reduces the amount of wastes stored in the depository, while on the other hand it eliminates the need to exploit deposits of natural soils and transport them to the crest of the highest embankments. In the case of a huge facility such as Żelazny Most, in which the annual dam development requires approximately 300,000 m^3 of soil, savings connected with the applied technology cover two basic cost components, i.e., the elimination of fees for the disposal of sediments built in the dams and no need to extract and transport natural soils for the dam's construction. It is also worth mentioning that due to crushing of the mine output the post-flotation tailings have the characteristics of fine-grained broken aggregates, easy to compact and having favourable shear-strength parameters, provided that the strict technological regime of the dam's construction is maintained. This regime has to be carefully controlled by different specific geotechnical control tests. A certain disadvantage of the described technology can be connected with the environmental impact due to periodic intensive dusting of the dried sediments embedded in the dams. However, this can be solved by the application of appropriate counter-measures reducing dust emissions to areas adjacent to the depository.

REFERENCES

[1] Gołębiewska, A., Lipiński, M.J. 2001. Measures for characterization of grain size distribution of post floatation tailings. Proc. of the 12th Polish National Conference on Soil Mechanics and Foundation Engineering, Szczecin-Międzyzdroje, Poland, (1a), pp. 211-219.

[2] Jamiolkowski, M. 2014. Soil mechanics and the observational method: challenges at the Żelazny Most copper tailings disposal facility. Géotechnique, 64, 8, 590-619. doi: 10.1680/geot.14.RL.002

[3] Jamiolkowski, M., Carrier, W. D., Chandler, R. J., Høeg, K., Świerczyński, W., Wolski, W. 2010. The geotechnical problems of the second world largest copper tailings pond at Zelazny Most, Poland. Proc. of the 17th SEAGC South East Asian Geotechnical Conference, Taipei, Taiwan (eds. J. C. C. Li and M. L. Lin), vol. 2, pp. 12-27.

[4] Lipiński, M.J., Wolski, W., Fioravante, V., Jamiolkowski, M.B. 1997. Preliminary evaluation of hazard due to liquefaction for Żelazny Most tailings pond. Proc. of 14th International Conference on Soil Mechanics and Foundation Engineering, Hamburg, (3), pp. 1843-1846.

[5] Młynarek, Z., Tschuschke, W., Welling, E. 1998. Control of strength parameters of tailings used for construction of reservoir dams. Proc. of the 5th International Conference on Tailings and Mine Waste, Fort Collins, Colorado, USA, pp. 213-221.

[6] Pordzik, P., Tschuschke, W., Wierzbicki, J. 2001. Statistical evaluation of tailings grain size distribution of the Żelazny Most Reservoir dams. Proc. of 12th Polish National Conference on Soil Mechanics and Foundation Engineering, Szczecin-Międzyzdroje, Poland, (1b), pp. 181-191.

[7] Tschuschke, W. 2006. Cone penetration tests in-post floatation sediments. Silesian University of Technology, Civil Engineering Gliwice, Poland (110).

[8] Tschuschke, W., Wierzbicki, J. 2012. Use of post-flotation copper tailings in the construction of dump dams. 2nd International Conference on Geotechnique, Construction Materials and Environment, Kuala Lumpur, Malaysia.

[9] Tschuschke, W., Gogolik, S., Kroll, M., Walczak, M. 2015. Tailings density indicators in the context of earthworks acceptance criteria. 17th National Conference on Soil Mechanics and Geotechnical Engineering, Łódź, (in print).

[10] Wierzbicki, J., Niedzielski, A., Waliński, M., Wołyński, W. 2004. The quality control of postflotation reservoir dam by determination of relative compaction index in various methods. Geotechnical and Geophysical Site Characterization Viana da Fonseca & Mayne (eds.). Millpress, Rotterdam, pp. 1371-1375.

[11] Wolski, W. 2003. Tailings dams – selected question. Proc. of 13th European Conference on Soil Mechanics and Geotechnical Engineering, Vanicek et al. (eds.), Prague, (3), pp. 167-176.

VREDNOTENJE KOEFICIENTA PREPUSTNOSTI ZA NAPOVEDOVANJE NABREKALNIH LASTNOSTI ZBITIH EKSPANZIVNIH ZEMLJIN

Hakan Güneyli
Çukurova University,
Dept. Geological Engineering
01330 Balcalı, Adana, Turčija
E-pošta: hguneyli@cukurova.edu.tr

Ključne besede

nabrekalne lastnosti, gradacija, prepustnost, stopnja primarnega nabrekanja

Izvleček

Nabrekanje ekspanzivnih zemljin je zelo pomembna lastnost v geotehniki, saj lahko povzroča visoko škodo na gradbenih objektih. Za projektiranje zadostno varnih in ekonomičnih inženirskih projektov morajo biti nabrekalne lastnosti dobro znane.

Neposredna določitev nabrekalnih lastnosti zahteva veliko časa in finančnih sredstev ter vključuje resen eksperimentalni napor. Druga možnost je, da se uporabi ena od tehnik za posredno ocenjevanje, ki so bile razvite s pomočjo empiričnih modelov regresije, le te so na voljo v literaturi ter pogosto uporabljene v praksi. Te empirične tehnike ocenjevanja so bile na splošno podane kot funkcija lastnosti zemljine, te so: konsistenčne meje, gostota, vlažnost, količina in vrsta glinene frakcije ter kationska izmenjalna kapaciteta.

Članek opisuje odvisnost odstotka nabrekanja (S%) in tlaka nabrekanja (σ_{sp}) dobljenega iz preizkusa prostega nabrekanja (FS) in preizkusa nabrekanja pri konstantnem volumnu (CVS) ter primarnega časa nabrekanja (PST). V pričujoči študiji predstavlja primarni čas nabrekanja, novo karakteristiko nabrekanja, v katerem skoraj 90 % nabrekanja nastopi kot deformacija, koeficient prepustnosti (k) pa je nadzorovan s spreminjanjem granulometrije zbitih nabrekljivih zemljin. Poleg tega sta bila stopnja primarnega nabrekanja (C_{ps}), ki predstavlja naklon krivulje odstotka nabrekanja (S%) v odvisnosti od logaritma časa v območju primarnega nabrekanja, in razmerje (C_{ps}/k) uporabljena za analiziranje njunih zvez z nabrekalnimi lastnostmi.

S pomočjo empirične metode te študije je mogoče, dodatno ali skupaj s konvencionalnimi parametri, posredno oceniti odstotek nabrekanja (S%), tlak nabrekanja (σ_{sp}) in primarni čas nabrekanja (PST) v odvisnosti od k, C_{ps} in C_{ps}/k. Korelacijski koeficienti regresijske analize kažejo na trdne odnose med nabrekalnimi lastnostmi in indeksi predlaganimi v tej študiji, ter potrjujejo, da se te empirične enačbe lahko varno uporabljajo za napoved v inženirski praksi.

ASSESSMENTS OF THE HYDRAULIC CONDUCTIVITY FOR PREDICTING THE SWELLING CHARACTERISTICS OF COMPACTED EXPANSIVE SOILS

Hakan Güneyli
Çukurova University,
Dept. Geological Engineering
01330 Balcalı, Adana, Turkey
E-mail: hguneyli@cukurova.edu.tr

Keywords

swelling characteristics, gradation, hydraulic conductivity, rate of primary swelling

Abstract

The swelling behaviour of expansive soils is significant in geotechnical engineering since it causes severe damage to civil structures. The swelling characteristics need to be well known for satisfactorily safe and economic engineering designs. A direct determination of the swelling characteristics requires considerable time and money, involving serious experimental effort. Alternatively, several indirect estimation techniques developed using empirical regression models available in literature are widely used in practice. These empirical estimation techniques have generally been assessed as a function of the soil properties, i.e., consistency limits, density, moisture content, clay fraction and type, and cation-exchange capacity.

This paper describes the dependence of the percentage swell (S%) and the swell pressure (σ_{sp}) obtained from a free-swell (FS) test and a constant-volume swell (CVS) test, and the primary swell time (PST), in which almost 90% of the swelling occurs as strain, which is considered as a new swelling characteristic in this study, on the hydraulic conductivity (k) controlled by a change in the gradation of compacted expansive soils. In addition, the rate of primary swelling (C_{ps}), which is the primary swelling phase's slope of the curve of percentage swell vs. log time, and the ratio of (C_{ps}/k) were used to analyse their relationships with the swelling characteristics.

This study provides the empirical methods that can be utilized to obtain indirect estimations of the percentage swell (S%), swell pressure (σ_{sp}) and primary swell time (PST) depending on k, C_{ps} and C_{ps}/k, in addition to, or with, the conventional parameters. The correlation coefficients of the regression analysis, having high performance, and indicating strong relationships between the swelling characteristics and the indices proposed in this study, state that these empirical prediction equations can be used safely in engineering practice.

1 INTRODUCTION

In many regions around the world, expansive soils are problematic for civil engineering projects such as low-rise buildings, embankments, airports, irrigation structures, roads and pavements, etc., some of which cannot be easily repaired. Such constructions over expansive soils having volume-change potential can suffer from considerable damage, irrespective of the project type, unless the swelling behaviour is taken into account. It has been recognized in geotechnical engineering that the swelling and shrinkage of expansive soils depending on moisture changing can result in significant distress, and

therefore in serious damage to the structures on such soils [1, 2, 3]. A number of swelling-soil problems and damage in buildings caused by such ground movements have been well documented in the literature [e.g., 1, 2, 4, 5, 6, 7, 8, 9, 10, 11].

Numerous techniques, i.e., oedometer methods, methylene blue test, and empirical (indirect) methods developed to estimate the swell potentials of expansive soils are available [e.g., 11, 12, 13, 14, 15, 16, 17, 18, 19]. Empirical methods, used widely in geotechnical engineering, are generally needed in preliminary site investigations and in the case of the presence of a number of check points on the project area. Empirical methods for estimating the swelling characteristics are related to the soils' physical/chemical properties of the Atterberg limits (i.e., liquid limit, (LL), plastic limit (PL)), dry density, linear shrinkage (LS) and plasticity index (PI), clay type and content, coefficient of linear extensibility, cation exchange capacity, initial degree of saturation and exchangeable bases [e.g.,13, 20, 21, 22, 23, 24, 25, 26, 27, 28, 29, 30, 31, 32, 33]. So far the investigations aimed at developing the swelling-prediction models have been based on relationships between the swelling potential (i.e., the percentage swell, *S*%), and/or the swell pressure and the soil properties mentioned above, assumed as a function of the swelling. In addition to these, Dananaj et al. [34] in their study, which only four data points of compacted different bentonites were used and correlated, reported an exponential dependence and a negative logarithmic relationship between the hydraulic conductivity (coefficient of permeability, *k*) and the percentage swell (swelling potential).

This study primarily focuses on the relationships between the swelling characteristics and the hydraulic conductivity controlled by the granulometric change of the clay soils. In this context, a method using two expansive clays with various percentages of uniform quartz sand was selected as a case study to generate a better understanding of the swelling behaviour of compacted fine-grained soils with different granulometries. The influence of the hydraulic conductivity (*k*) related to the content of uniform quartz sand in two different types of compacted clay-sand mixtures on the swelling characteristics, which were obtained from swelling tests using a conventional odeometer test device, was firstly investigated. In addition, the effects of granulometric change controlled by the increase in the sand ratio on the swelling characteristics of the percentage swell, swell pressure obtained from both the free swell test and the constant-volume swell test, and the primary swell time as a new term was also assessed in terms of graphical and statistical methods. By considering that *hydraulic conductivity, the rate of primary swelling* and the indices of *the rate of primary swelling-to-hydraulic conductivity* are functions of swelling, correlations between these variables and the swelling characteristics were made. Thus, the empirical prediction formulas for the swelling characteristic were derived using simple and multi-regression analysis.

2 MATERIAL

For the laboratory investigation of the changes in the swelling characteristics developed by clay-sand mixtures

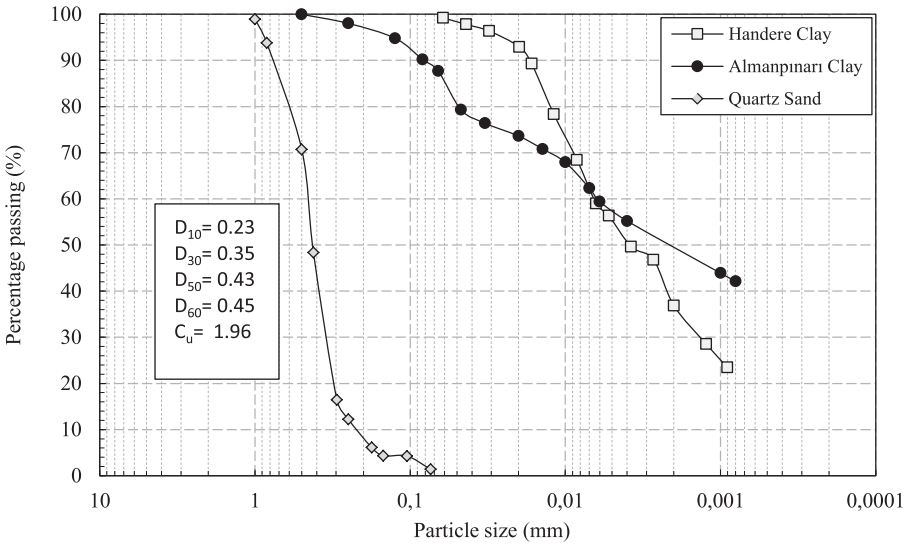

Figure 1. Particle size distributions for the sand and soils used during the experimental study.

with various granulometry techniques, two different clays, i.e., Handere Clay and Almanpınarı Clay, and a uniform quartz sand were used.

Specific gravity analysis, particle size analysis and Atterberg limit tests were performed to classify the clays and the quartz sand in accordance with the Unified Soil Classification System (USCS). The tests were performed on all the used samples according to the test procedures outlined in ASTM D 854-10 [35], ASTM D 422-63 [36], ASTM D 4318-10 [37] and ASTM D 427-98 [38], respectively. The characteristics of all the materials are summarized in Tables 1 and 2.

2.1 Clays

Two clay soils named Handere Clay and Almanpınarı Clay were used in this investigation. Handere Clay was derived from claystone layers of the Handere formation (Pliocene), north of the Adana region (Turkey), while Almanpınarı clay was derived from the clay formation in limestone layers aged U. Cretaceous, south of the Osmaniye region (Turkey). The depths of sampling were 0.5–1.0 m. Handere Clay contains mainly smectite, known to be expansive, and lesser amounts of illite and chlorite [39]. It has a liquid limit, LL=54; a plastic limit, PL=24; and a specific gravity, G_s=2.65. Almanpınarı Clay predominantly illite [40] known as moderate expansive has a liquid limit, LL=37; a plastic limit, PL=17; and a specific gravity, G_s=2.67.

Table 1. Index Properties, Classifications and compaction parameters of the tested soils.

Soil Name		Almanpınarı clay	Handere clay	Quartz Sand
LL (%)		37	54	
PL (%)		17	24	
PI (%)		20	30	
SL (%) (Shrinkage Limit)		9	13	
R (Shrinkage ratio)		1.99	1.95	
L_S (%) (Linear shrinkage)		9	14	
Specific gravity, G_s		2.67	2.74	2.63
Fines content (%)		92	99	
Sand size 4.75-0.075mm (%)		12	1	100
Silt size 0.075-0.002 mm (%)		33	62	
Clay size (%)<0.002mm		55	37	
Activity		0.42	0.5	
Initial void ratio (e_0)		0.589	0.662	
Classification	USCS	CI	CH	SP
	Group Name	Inorganic clays of medium plasticity	Inorganic clays of high plasticity	Poorly graded sand
Standard Proctor compaction	MDD (kg/m^3)	1683	1621	
	OMC (%)	19.4	19.3	

2.2 Sand

A commercially available quartz sand named Hebilli, derived from Mersin province (south of Turkey) was used in soil-sand mixtures. Grain size analyses (by sieving) of the sand are also shown in Fig. 1. It is a uniform, yellowish quartz sand (with a SiO_2 content of 99.47%) and classified as poorly graded sand (SP) according to the Unified Soil Classification System (USCS). Grain-size data of the sand indicate a mean diameter D_{50}=0.43 mm, a coefficient of uniformity C_u=1.96, a coefficient of curvature C_c=1.18 and an effective diameter D_{10}=0.23 mm (Table 1).

3 SAMPLE PREPARATION

The sample-preparation technique was the same for all the specimens. The specimen preparation for the tests was performed at room temperature. Sand–clay mixtures were prepared on a dry-weight basis by using oven-dried (at 60 °C) sand and clay. The required amount of sand and clay were weighed, and mixed carefully in a dry state, until a homogeneous mixture was obtained.

For each of the two clays mentioned above, six artificial soil specimens were prepared by adding 0, 10, 20, 30, 40 and 50% of ,the uniform quartz sand by weight, in dry conditions, taking account of their natural grain content of sand size. In this way mentioned above, using two types of clay and one type uniform sand, two sets of artificial soil samples consisting of different clay-sand ratios were prepared. Following the oven drying, the sand-clay mixtures were compacted using a Proctor mould at values of optimum moisture content (OMC) and maximum dry density (MDD) obtained from the compaction curves.

Compacted soil samples in the swelling tests were used in order to provide homogeneity and eliminate the macro and micro cracks. In addition to that, the compacted specimens were preferred to provide the uniformity of the factors such as moisture content (w), void ratio (e) and natural density (γ_n) on swelling, as well. Therefore, Standard Proctor compaction tests according to *ASTM D 698-07698-07* [41] were performed on each mixture

to determine the compaction curves. The maximum dry densities and the optimum moisture contents of these artificial soils were achieved by applying an energy level of 600 kN-m/m^3, equal to the standard compactive effort recommended *by ASTM D 698-07698-07* [41].

The compaction curves of each mixture were displayed in Fig. 2 and 3. All the mixtures had bell-shaped compaction curves. From Fig. 2 and Table 2, it is clear that the values of MDD and OMC range between 1683–1881 kg/m^3 and 19.4–12 % for the mixtures of Almanpınarı Clay-Quartz Sand, respectively. On the other hand, as seen in Fig. 3 and Table 2, the values of MDD and OMC for the mixtures of Handere Clay-Quartz Sand are 1621–1791 kg/m^3 and 19.0–13.2 %, respectively.

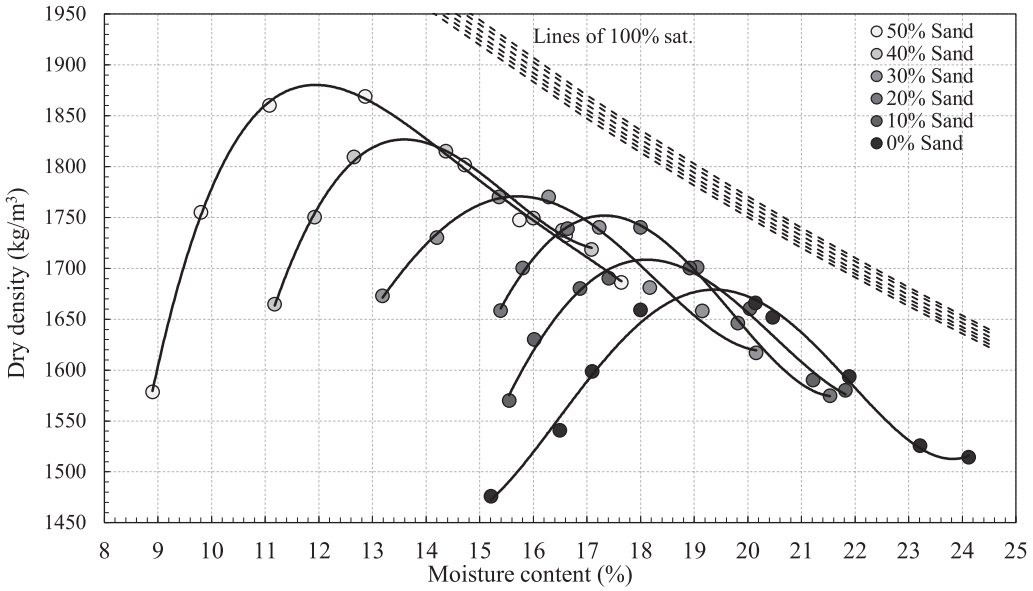

Figure 2. Graph of Standard Proctor compaction curves of Almanpınarı Clay and its mixtures with sand.

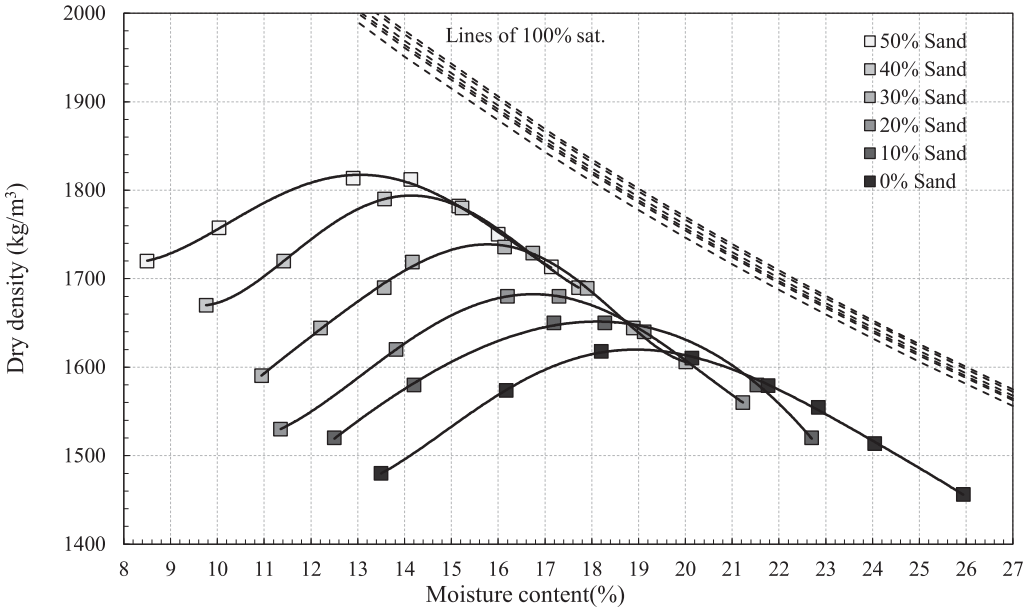

Figure 3. Graph of Standard Proctor compaction curves of Handere Clay and its mixtures with sand.

Table 2. Compaction parameters (Optimum moisture content [OMC], Maximum dry density [MDD], initial void ratio (e_0) and saturation degree [s(%)]) of soil-sand mixtures.

Clay Name	Almanpınarı Clay				Handere Clay			
Sand content (%)	MDD (kg/m^3)	OMC (%)	e_0	s(%)	MDD (kg/m^3)	OMC (%)	e_0	s(%)
50	1881	12.0	0.426	74.9	1791	13.2	0.499	71.0
40	1825	13.6	0.479	76.5	1787	14.2	0.513	74.8
30	1774	15.8	0.527	81.1	1754	15.8	0.545	78.6
20	1754	17.4	0.551	85.8	1683	16.8	0.617	74.2
10	1713	18.2	0.594	83.6	1652	18.1	0.653	75.6
0	1683	19.4	0.629	84.5	1621	19.0	0.690	75.5

After compaction, the soil was immediately extruded from the mould using a hydraulic jack. The side friction causing damage to the soil sample during the intrusion and extrusion was minimized by lightly lubricating the inner surface of the mould. After sampling, all the samples were covered with a stretch film and aluminium folio and stored in a wet room for one week to guarantee good moisture equilibration and homogeneity.

4 METHOD

Both the free-swell (FS) tests (constant stress tests) and the constant-volume swell (CVS) tests on the clay-sand mixtures were performed to measure the swelling deformation (percentage swell, S%) and the swell pressure. All the swelling tests were conducted in the conventional oedometer test device. The FS tests and CVS tests in accordance with *ASTM D4546-96: method A and C* [42] were carried out on two different fine-grained, compacted soil sets containing various proportions of quartz sand, i.e., from 0 to 50%.

All the artificial soils were tested in a standard fixed ring, 50 mm diameter and 20 mm height. However, a ring thinner than usual was used to reduce possible distribution. On the other hand, the side friction between the ring and the soil specimen, causing damage to the soil specimen during the intrusion, was minimized by lightly lubricating the inner surface of the ring with grease. Afterwards, the ring was intruded into the compacted soil-sand mixture using a hydraulic jack. The deformation caused by swelling or consolidation during the wetting is only in the vertical direction. The tests were performed with distilled water in order to avoid the possible effects of ion exchange.

In order to determine the percentage swell and the swell pressure (provided from FS tests) of the compacted pure clays and clay–sand mixtures, free-swell (FS) tests were performed. The sample in the ring was placed between two porous stones, loaded with a seating pressure (σ_{se}) of 1.0 kPa, and oedometer cell was fully inundated with distilled water. After the specimen was allowed to swell, readings of the dial gauge were periodically recorded for up to 18 days (Fig. 4). The percentage swell (S%) was then calculated as an increase in the length in relation to the initial thickness of the specimen. The deformation was considered to be finished when the variation in the indicator on the displacement transducer was less than 0.01 mm after an interval of 24 hours. After completion of the swell, the pressure maintained in the vertical direction (by conducting *ASTM D 2435* [43]) and necessary to achieve the initial void ratio/height of the specimen was calculated as the swell pressure (σ_{sp}).

The constant-volume swell (CVS) tests, another method to determine the swell pressure, were also conducted on all the specimens. In the CVS tests the vertical pressure increment was applied constantly to keep the volume of the specimen unchanged/or to prevent swelling. The vertical stress, which was provided to fully complete the swell or needed to prevent the swell, was considered as the swell pressure (σ_{sp}) of the specimen at a certain dry density.

The results of FS and CVS tests on the pure clays and the mixtures having various sand contents and the effect of the sand content on swell percentage and pressure of the soils were given in Table 3 and Fig. 5 and 6, respectively.

In order to compare the hydraulic conductivity (k) and the swelling characteristics, finally, the permeability tests were conducted on the compacted artificial soil specimens with the same properties as those used in the swell tests. For this purpose, falling-head permeability tests in accordance with *ASTM D 5856–95* [44] were performed. Each test was repeated three times and used the average values of these three tests results.

Correlations, and simple and multi-regression analysis, were carried out to identify the related variables effecting the swelling phenomena. The individual variables (parameters) focused on in this study, such as the content of quartz sand, the hydraulic conductivity and the rate of primary swelling, were compared to obtain correlations, and calculated estimates of the swelling characteristics of the percentage swell, swell pressure and the primary swell time, and the statistical relationships. The correlation coefficients of the relationships between the various properties and the experimentally obtained measurements (values) were used to derive prediction formulas for the swelling characteristics, and to analyse the confidence of those correlative functions.

5 EXPERIMENTAL RESULTS AND ANALYSIS

The swelling characteristics and the initial hydraulic conductivity (k) corresponding to the clay specimens having various sand contents are summarized in Table 3 for two clay types. Fig. 4a-b shows the log time vs. percentage swell for six different gradations of two different soil sets. The percentage swell (S%) is described as the ratio of the quantity of swell to the initial thickness of the soil specimen represented as a percentage. As can be seen in Fig. 4a-b, the enhancement in S% is relatively fast during the initial phases, and it gradually approaches the ultimate grade. Even after a period of 13–18 days, there was a gradual and slow increase in S%. On the other hand, the time to reach the ultimate swell level is a maximum for the specimens of pure clay for both clay types.

Yule and Ritchie [45] and Gray and Allbrook [46] reported there to be no relationship between clay percentage and soil swelling, and Karuiki and var der Meer [28] stated there were poor correlations among them. ElKholy [47] reported that the increasing coarse fraction in clay decreases exponentially both the percentage swell and the swell pressure. On the other hand, Rao et al. [48], Gürtuğ et al. [49] and Mishra et al. [50] stated there was a linear decrease for similar situations, whereas Cui et al. [51] suggested that with the increase in sand content of bentonite-sand mixtures, the percentage swell shows a sigmoid decrease, and the swelling pressure obtained from the CVS tests decrease exponentially. It is clear that there is no consensus on this subject in the literature, which is summarized partly above.

Fig. 5 presents the relationships between percentage swell (S%) and sand content for the clays. The figure indicates that the increase in sand content decreases almost linearly S%. The results about the effects of coarse particle content in clay soils on S% exhibit similarities to those found by Gürtuğ et al. [49] and Mishra et al. [50]. The addition of quartz sand up to 10% leads to an

Table 3. Percentage swell (S%), swell pressure (obtained from FS and CVS tests) hydraulic conductivity (k), completion time of primary swelling (PST), and rate of primary swelling (C_{ps}) at different sand contents of the clay soils studied.

Sand Content (%)	Percent Swell, S%	Swell Pressure [for FS tests] σ_{sp} (kPa)	Swell Pressure [for CVS tests] σ_{sp} (kPa)	Hydraulic conductivity, k (cm/sec)	Primary swell Time, PST (min)	Rate of primary swelling, C_{ps} (S%/min)
Almanpınarı clay						
0	8.2	764.9	192.2	3.66E-08	360	0.0195
10	6.0	684.9	163.9	5.71E-08	320	0.0175
20	4.2	412.9	144.1	5.69E-08	248	0.0148
30	2.6	258.4	122.5	9.28E-08	288	0.0068
40	1.8	170.6	86.6	1.57E-07	210	0.0078
50	1.2	121.6	62.5	1.70E-07	173	0.0051
Handere clay						
0	10.5	1026.8	454.4	1.44E-08	1490	0.0107
10	8.1	779.6	224.3	2.04E-08	1450	0.0075
20	7.9	774.5	169.2	2.06E-08	1350	0.0074
30	6.7	653.9	169.4	2.61E-08	1040	0.0068
40	4.5	445.2	107.3	4.26E-08	675	0.0059
50	2.4	233.3	48.2	5.37E-08	640	0.0030

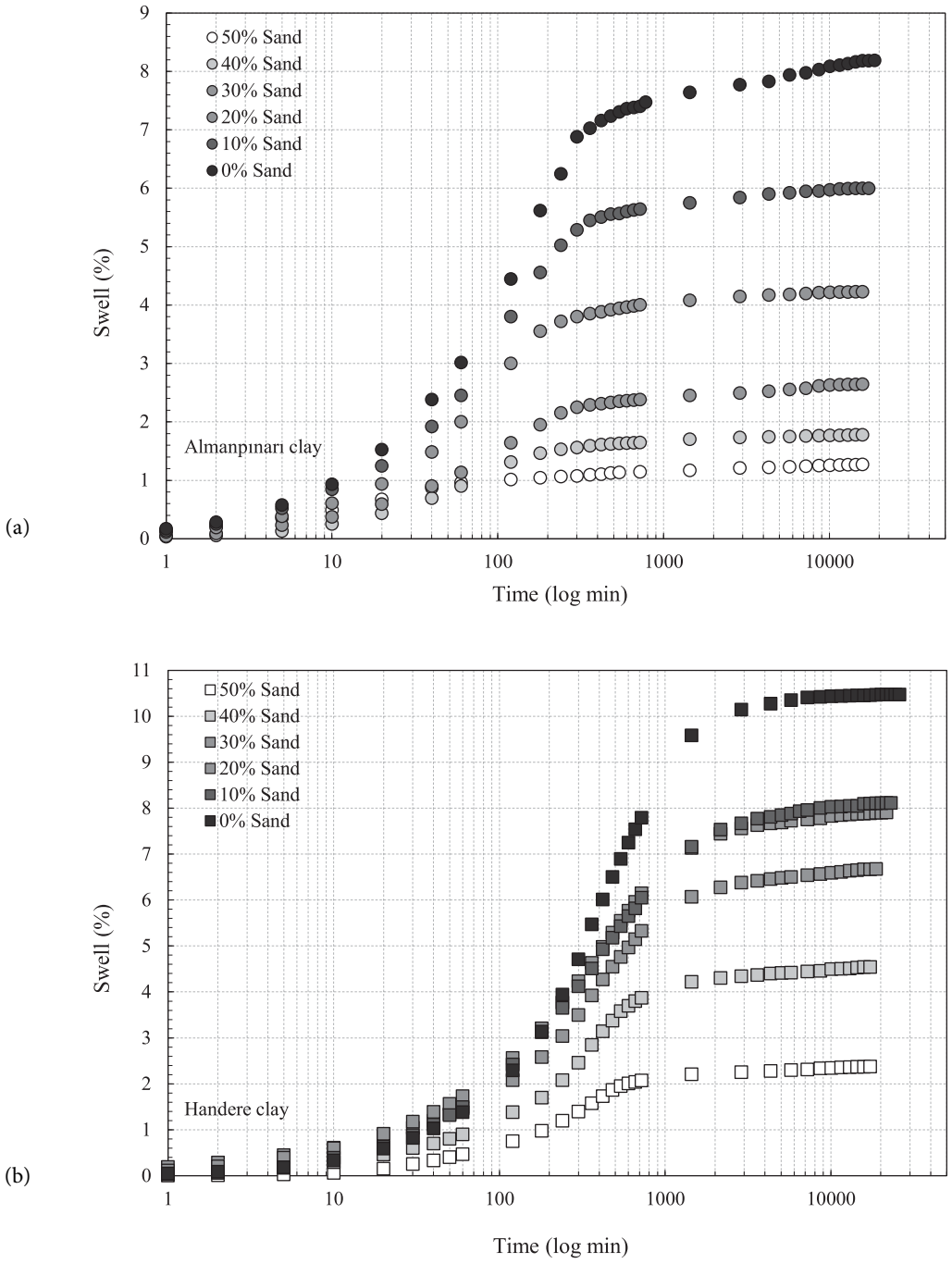

Figure 4. (a). Log time vs. percentage swell relationship for Almanpınarı clay and its mixtures with the quartz sand (b). Handere clay and its mixtures with the quartz sand.

approximately 14 and 16% reduction in *S*% for Handere and Almanpınarı clays, respectively (Fig. 5). Despite the fact that the clays tested in this study have distinct swelling characteristics (Table 3), an increase of the sand content creates very close or almost same effect on *S*% for them. Fig. 6 shows the swell pressure (σ_{sp}) values obtained from both the FS and CVS tests vs. sand content for Handere and Almanpınarı clays. The results indicate that there are strong negative correlations between the sand content and σ_{sp}.

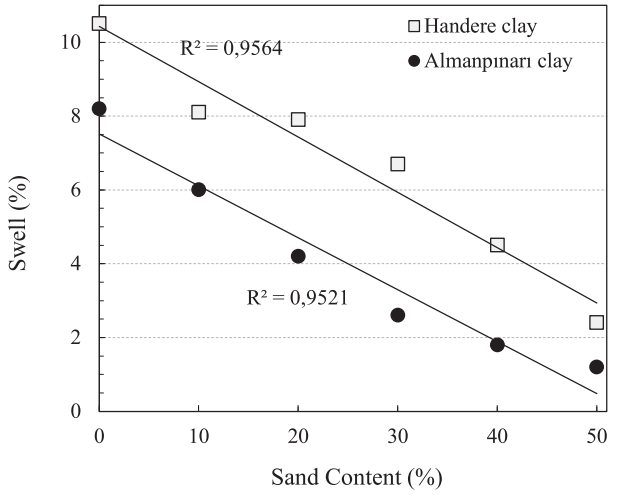

Figure 5. Sand content vs. percentage swell.

The correlation coefficient in the statistics was classified as strong, medium and weak for R≥0.8, 0.8<R<0.2 and R≤0.2, respectively [52]. As expected, compared to σ_{sp} and sand content of clay it appears that σ_{sp} decreases linearly as the sand content increases. An increase in the sand content of 10% leads to a decrease in σ_{sp} obtained from the FS test of average 159 and 129 kPa (or 24 and 30.1%) for Handere clay, and from CVS test of average 81 and 26 kPa (33.4 and 19.8%) for Handere clay and Almapınarı clay, respectively. Consequently, although the relations between the sand content and *S*% for the clays tested in this study are quite similar, the relations between sand content and σ_{sp} are unique, i.e., they depend on the clay type.

Based on the test results, σ_{sp} values obtained from the FS tests are greater than those obtained from the CVS

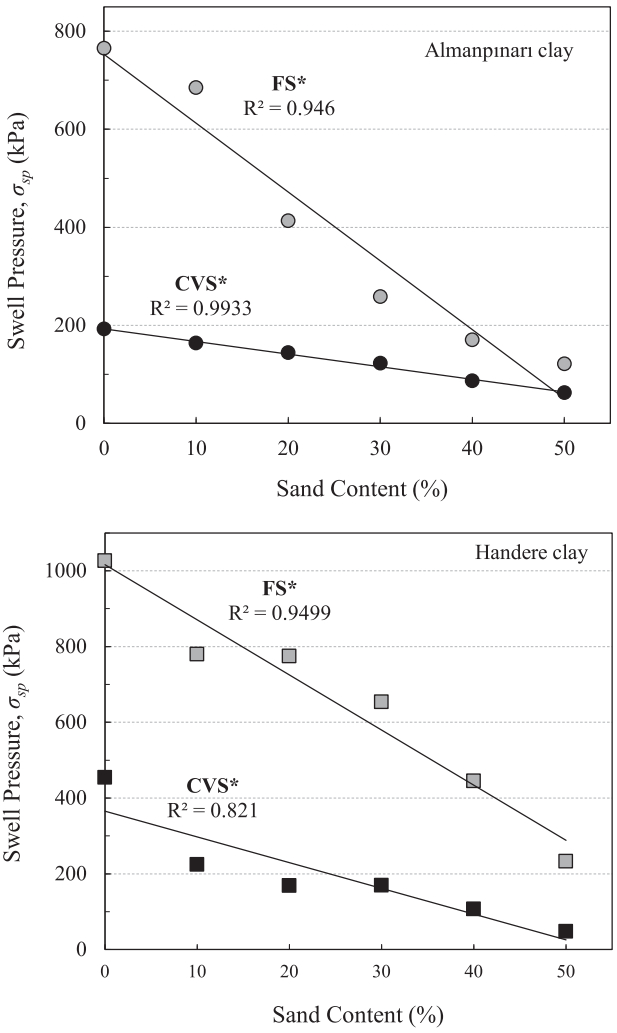

Figure 6. Effect of uniform quartz sand content on the swell pressure obtained from free-swell (FS*) and constant-volume swell (CVS*) tests for the specimens used in this study.

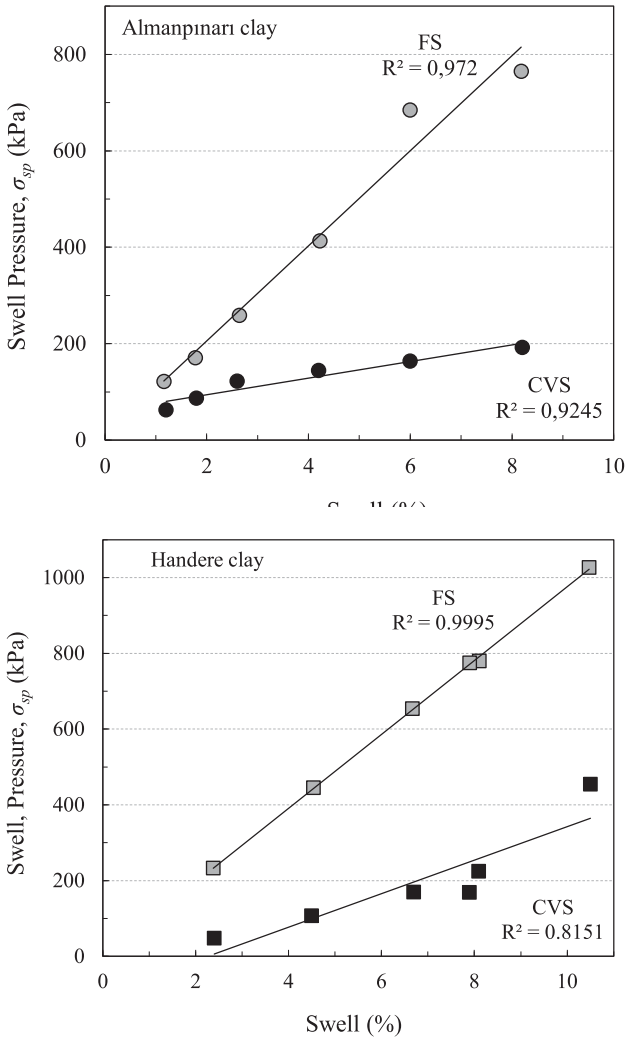

Figure 7. Percentage swell vs. swell pressure obtained from FS and CVS tests.

tests. The difference in the amount of σ_{sp} values between FS and CVS tests reduces with the quartz sand addition. However, considering the reducing as a ratio of σ_{sp} from FS test to σ_{sp} from CVS test [$\sigma_{sp(FS)}/\sigma_{sp(CVS)}$], when the sand content increases from 0 to %50, the reducing ratio ranges from 2.3 to 4.8 for Handere clay, whereas it is from 4.0 to 1.9 for Almanpınarı clay. This indicates that the difference between σ_{sp} obtained from FS and CVS test, and the change in that ratio mentioned above most probably is due to the clay type and its mineralogy.

Fig. 7 submits *S*% vs. σ_{sp} from the results obtained on the two clays with the six different sand contents (gradations). Linear-regression lines were fitted to all the data. Due to the linear-regression analysis, statistically quite meaningful relations were obtained between *S*% and σ_{sp} (for both FS and CVS). Quite similar attenuation relationships emerged between *S*% and σ_{sp} . Regardless of the clay type and the sand content, distinctive relationships from both the FS and CVS tests for the two clays were obtained between *S*% and σ_{sp} (Fig. 8). As seen in Fig. 8-a, an almost perfect linear relationship of the results obtained especially from the FS tests occurred. The results of the regression equations and the correlation coefficients for *S*% and σ_{sp} , which were derived from all the soils tested in this study, are listed in Table 4, as Eq. 1-2, and shown in Fig. 8a-b.

Table 4. Simple regression analysis results.

Regression equation	Correlation (judgment coefficient)	Equation Number
$\sigma_{sp(FS)}$=96.94*S*%+9.42	*R*=0.994	(1)
$\sigma_{sp(CVS)}$=30.12*S*%+1.14	*R*=0.852	(2)
PST=8E-05$k^{-0.926}$	*R*=0.919	(3)
S%=1E-05[C_{PS}/k]+1.89	*R*=0.943	(4)
$\sigma_{sp(FS)}$=0.0013[C_{PS}/k]+194.06	*R*=0.934	(5)
$\sigma_{sp(CVS)}$=0.0004[C_{PS}/k]+43.31	*R*=0.919	(6)

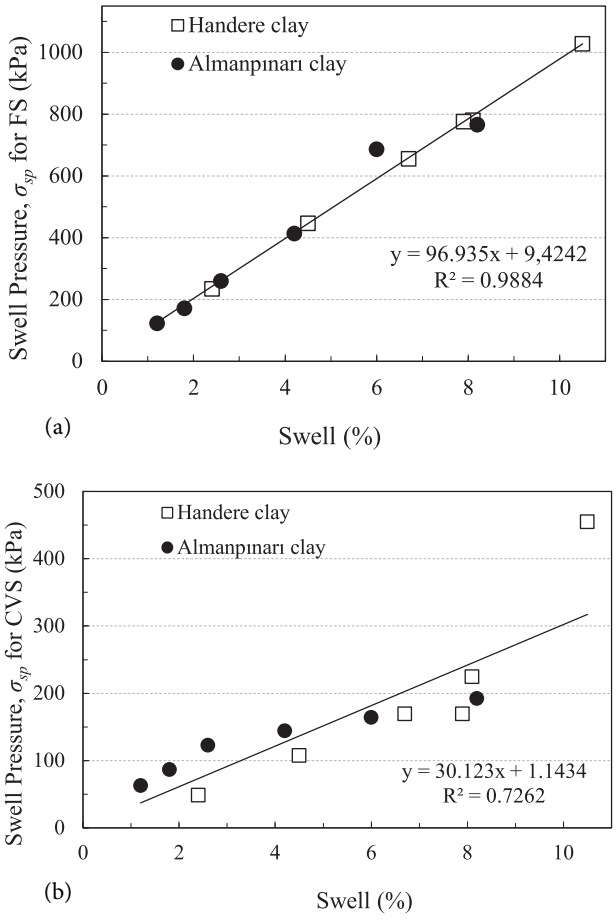

Figure 8. (a). Swell pressure obtained from FS test vs. swell percentage relationship, (b). Swell pressure obtained from CVS test vs. swell percentage relationship.

The main phases that can be expressed as the initial swelling or inter-void swelling [51], the primary swelling, and the secondary swelling are seen in the graph of *S*% vs. log time (Fig. 4). The S-shaped curve in this graph consists of three distinct slopes defined by the phases mentioned above. It is clear that the parameters of the swelling time and *S*% of the primary swelling as a function of swelling process can also be determined clearly. Sridharan and Gürtuğ [53] pointed out the similarity between the S-shaped curves of the *S*% vs. log time and the strain-log time for the consolidation process, indicating a diffusion process founded and those S-shaped curves expressed by Feda [53], and thus proposed an equation of $C_{as}=\Delta(\delta H_c/H) / \Delta\log_{10}t$ based on this resemblance, where $\Delta(\delta H_c/H)$ is the ratio of the secondary swelling, δH_c to the thickness of the sample, *H* during the time period of t1 to t2.

The primary swelling has an almost linear curve in the *S*% vs. log time plot, and is also similar to the linear portion of the strain-log time curve representing the primary consolidation (compression). Consequently, based on the similar analogical comparison, the *rate of primary swelling (C_{ps})* can be defined as the slope of the curve of *S*% vs. log time, and formulated as

$$C_{ps} = \frac{\Delta S}{\Delta \log t} \qquad (7)$$

where ΔS, (*S*2-*S*1) is the magnitude of change in *S*% during the time period of *t*1 to *t*2.
$\Delta\log t=\log t2-\log t1$

An examination of Fig. 4 a-b shows that the shape of *S*% vs. log time is typically similar to an *S* for all the specimens tested in this study. From Fig. 4 a-b it is clear that the slope of the curve in the initial and primary portions increases as the sand content of the soil decreases (or the clay fraction increases). This increment is quite particular, especially in the primary swelling portion, even though there are some exceptions in the phase of the initial swelling. It is clear that the completion time of the primary swelling or the primary swelling time (*PST*), which can be determined by means of the graphical method seen in Fig. 9, decreases with increasing of sand content. Fig. 10 indicates that there is an apparent negative linear relationship, which is unique for each clay type, between the primary swelling time and the sand content.

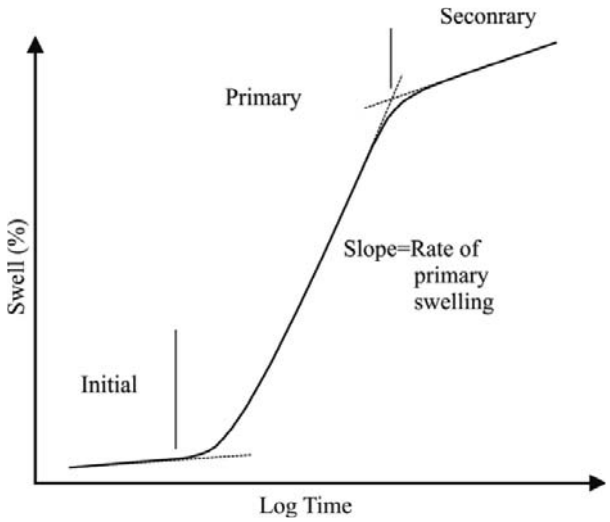

Figure 9. Schematic diagram showing the separation of the initial, primary, and secondary swellings [42, 51 and 53].

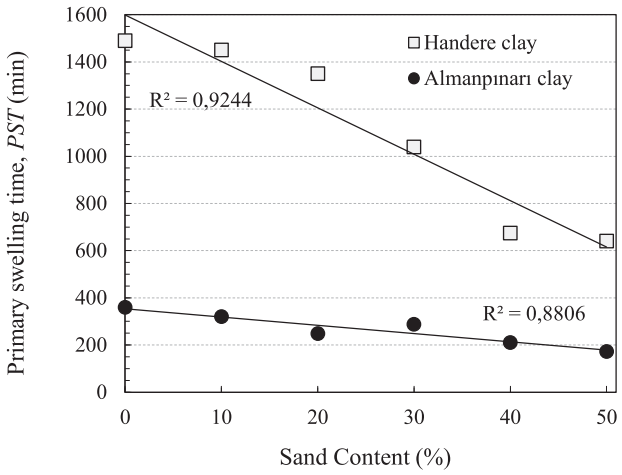

Figure 10. Effect of uniform quartz sand content on the primary swelling time, *PST*.

Compared to the rate of primary swelling (C_{ps}), considered as a parameter relating to the swelling behaviour, corresponding to *S*% and σ_{sp}, it is clear that C_{ps} increases linearly as both *S*% swell and σ_{sp} (obtained from both FS and CVS tests) increase, having strong correlation coefficients (Fig 11 and 12). Although it is clear that *S*% and σ_{sp} are closely related to C_{ps}, each relation is unique for the two clay types. It is clear from Fig. 11 and 12 that the relationships between C_{ps} and *S*%, and the σ_{sp} shows significant positive correlations between these parameters. The relationships between C_{ps} and the primary swell time (*PST*), almost 90% of swelling, as strain occurs in this phase, exhibits particular positive correlations between the two parameters depending on the clay type (Fig. 13), i.e., the steeper slope of the curve *S*% vs. log time, the longer time that the primary swelling occurs during the swelling. These strong correlations clearly indicate that C_{ps} is a function of the swelling and can be used in a prediction of the swelling characteristics (of *S*%, σ_{sp} and *PST*).

To check the effect of the hydraulic conductivity (*k*) on the swelling characteristics of *S*%, σ_{sp}, and *PST*, a series of comparisons was performed on the measurements obtained for the two clay specimens containing various sand-content ratios. It was reported that *k* and the void ratio of the soil-bentonite mixtures increase during swelling process [50 and 55]. Therefore, the initial *k* values were used in the correlations. Fig. 14 presents the relationship between *k* and the sand content in the two different clays used in this study. As expected, the figure shows that *k* increasingly varied with the sand content in the clay as well. A further increase in the sand content from 0 to %50 increased *k* only from 1.44×10^{-8} to 5.37×10^{-8} cm/sec and from 3.66×10^{-8} to 1.70×10^{-7} cm/

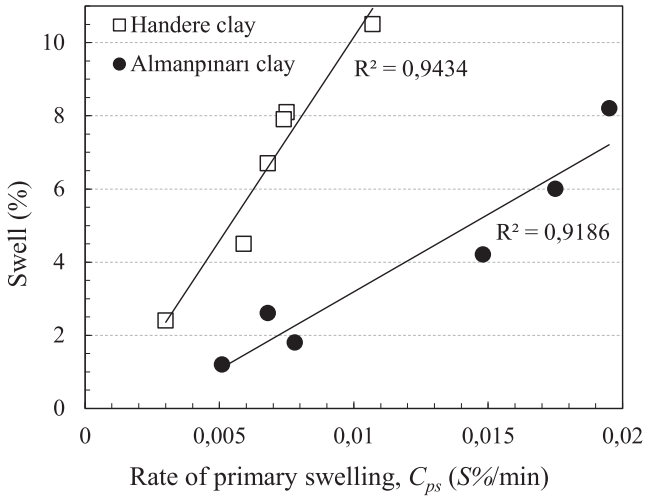

Figure 11. Relationship between the percentage swell and the rate of primary swelling.

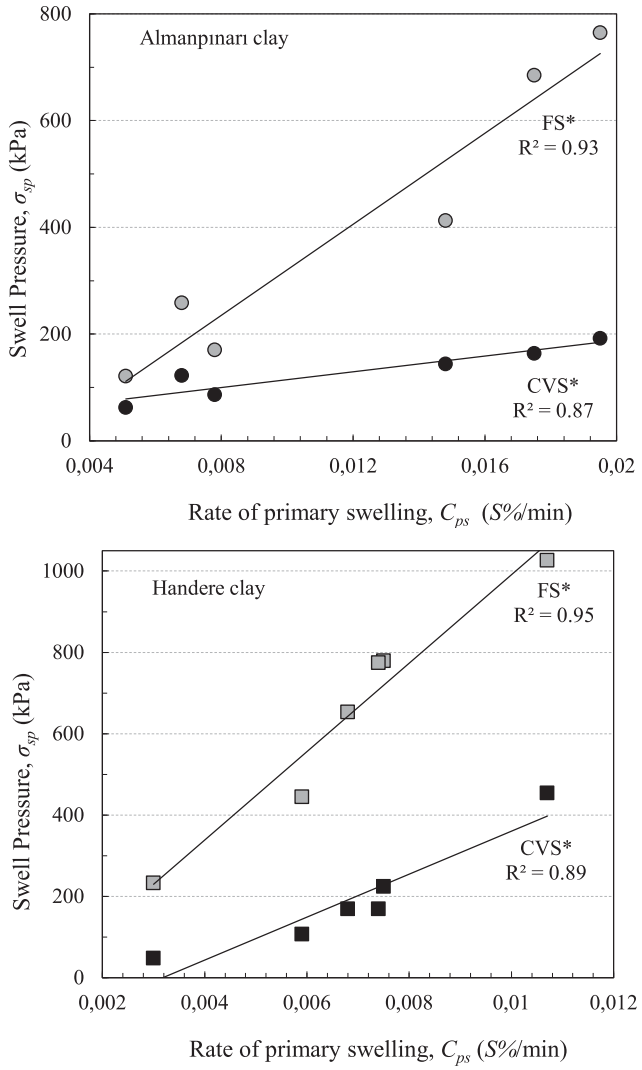

Figure 12. Relationship between the swell pressure and the rate of primary swelling (FS is the data obtained from the free-swell test, and CVS from the constant-volume swell test).

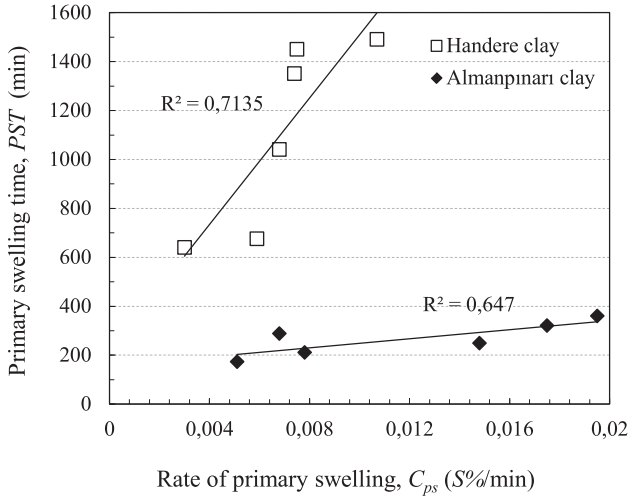

Figure 13. Relationship between the primary swelling time, *PST* and the rate of primary swelling, C_{ps}.

sec for the mixtures of Handere clay and Almanpınarı clay, respectively. The data from Fig. 14 and Table 3 show that the increase in k with the addition of quartz sand was much more for the Almanpınarı clay than that for the Handere clay, while the initial (for 100% clay) k values of these two different clays were relatively close to each other.

The hydraulic conductivity (k) of the mixtures was plotted in Fig. 15 and 16 as a function of S% and σ_{sp}, respectively. The results shown in Fig. 15 and 16 show that both S% and σ_{sp} (kPa) have an exponential decrease with an increase in k. The comparison of k corresponding to the values of S% and σ_{sp} indicates that there are negative relationships between k and both S% and σ_{sp}. The relationship between k and S% is seen in Fig. 15. The figure shows that the position and slope of the respective curves change in particular. The curve of Almanpınarı clay with higher k tends to locate upwards and has a greater slope than that of the Handere clay. The decrease in k with an increase in S% was quite steep

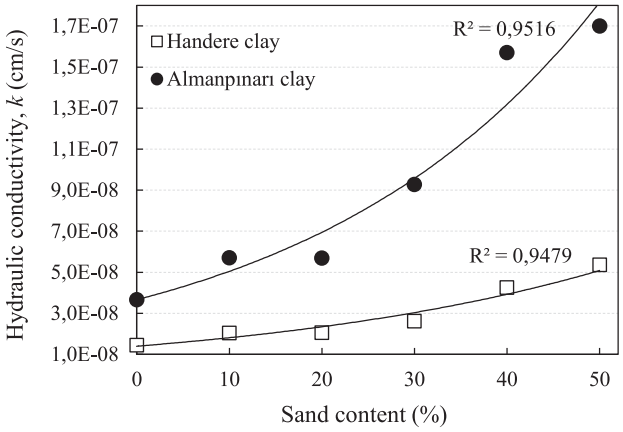

Figure 14. Hydraulic conductivity, k vs. sand content.

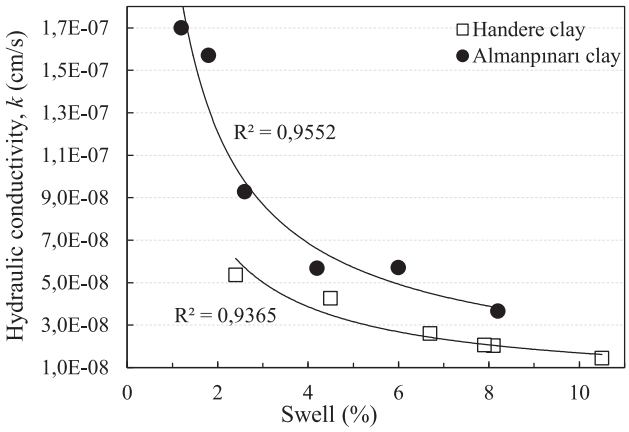

Figure 15. Hydraulic conductivity, k vs. percentage swell.

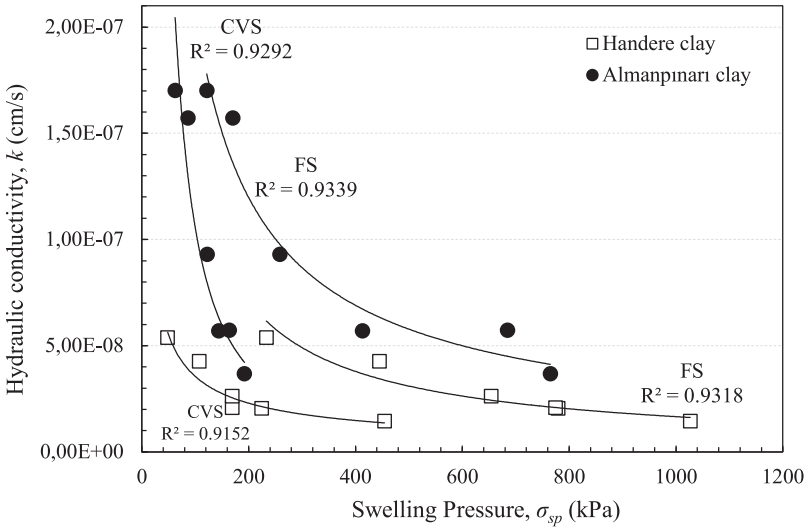

Figure 16. Hydraulic conductivity (k) vs. swell pressure.

in the beginning where k decreased from 1.7×10^{-7} to 5.69×10^{-8}cm/sec with an increase in S% from 1.2 to 4.2%, and remained nearly constant afterwards for the Almanpınarı clay, while this variation was relatively less for the Handere clay than that of the Almanpınarı clay.

A similar status to that mentioned above can be seen between k and σ_{sp} obtained from both FS and CVS tests (Fig. 16). Consequently, it is clear that k has a significant negative influence on the swelling behaviour of a clay depending on the changing gradation, and can be evaluated as a function of the swelling properties of S% and σ_{sp}. The reduction in S% and σ_{sp} due to the increase in k can be explained in terms of the decrease in the amount of clay leading to swelling phenomena, while the sand particles (non-swelling material) increase, resulting in the increase in k.

Consequently, the data from Fig. 15 and 16 show that there is no clear relationship between k and the corresponding swelling parameters for these two different types of clay. On the other hand, an assessment of a particular clay type and its mixtures with sand indicates that a clay sample with higher k depending on gradation possess a smaller S% and σ_{sp}.

The hydraulic conductivity (k) followed a similar trend (hyperbolic, i.e., exponential) with the primary swelling time (*PST*) as well. Irrespective of the clay type and the sand content, a unique relationship having a strong negative correlation coefficient (R=0.919) for all the specimens was obtained between *PST* and k (Fig. 17). Similar to Fig. 14-16, the k for the clay-sand mixtures exhibited a steep decline from 1.70×10^{-7} to 2.61×10^{-8} cm/sec with an increase in *PST* from 173 to 1040 min, and much less change for a further increase in *PST*. With an increase in k, the interaction volume increases and the clay particle becomes free to move at higher water contents, resulting in an increase in the interparticle distance as a function of time and consequently the *PST* reduces. Based on this *PST* is an exponential function of k, and on the simple regression analysis, it can be defined as

$$PST=8\text{E-}05k^{-0.926} \quad (R=0.919) \qquad (3)$$

where *PST* is primary swelling time; and k is the hydraulic conductivity.

In order to show the relationship between the values experimentally measured and predicted, the *PST* predicted by Eq. (3) is compared with the measured values from the tests, as shown in Fig. 18. The figure shows that the predicted values are very close to the measured values. The cross-correlation between the predicted and measured data indicated a strong coefficient of correlation (R=0.8862), and that the measured *PST* is 1.1177 times the predicted *PST*.

An examination of Fig. 19 shows that the rate of primary swelling (C_{ps}) decreases with the increment of the k depending upon the type of clay. The figure also shows that the position and slope of the respective curves differ significantly. The curve of Handere clay with lower k tends to locate downwards and gives a lesser slope. Therefore, it can be assumed that k is of a function of C_{ps} as well, and this inverse proportion between them is unique for each soil type.

Taking into account that the hydraulic conductivity (k) and the rate of primary swelling (C_{ps}) are functions of

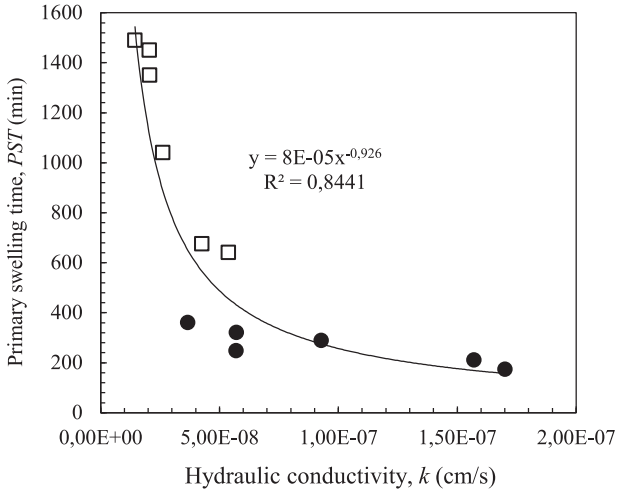

Figure 17. Hydraulic conductivity, *k* vs. primary swelling time, *PST* relationship for all the mixtures tested.

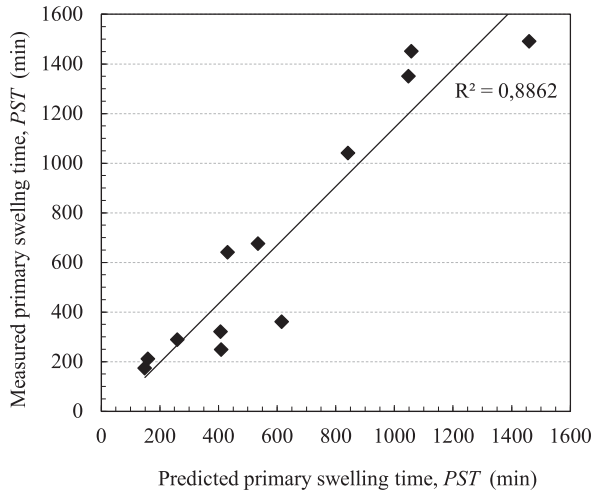

Figure 18. Measured primary swelling time, *PST* vs. predicted primary swelling time for all the test results.

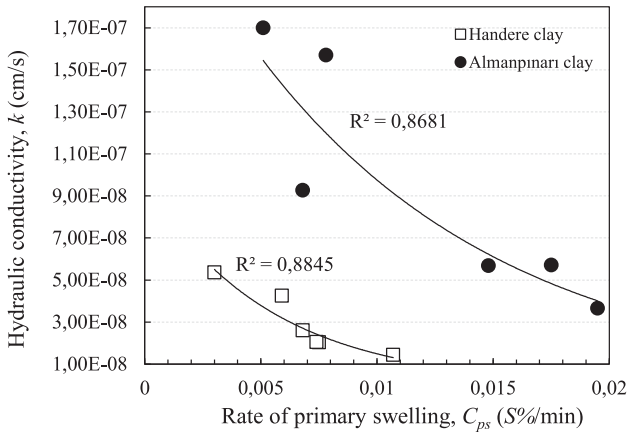

Figure 19. Hydraulic conductivity, *k* vs. the rate of primary swelling, C_{ps}.

the swelling process, and related to each other, the ratio of $[C_{ps}/k]$ as an indices (where C_{ps} normalized by *k*) in the estimate models that were focused to find the main swelling characteristics of *S*% and σ_{sp} was used to obtain the general linear prediction equations. Thus, the indices of $[C_{ps}/k]$ was assessed to determine *S*% and σ_{sp} obtained for both FS and CVS tests, as a function of them (Fig. 20, 21 and 22, Eq. 4-6). The graphs seen in Fig. 20-22, offering to evaluate multi (more than two) parameters depending on soil type, indicate that the value of this index can be assessed as a variable to predict the main swelling characteristics of *S*% and σ_{sp}. The data indicate that a straight line could fit the indices of $[C_{ps}/k]$ against *S*% and σ_{sp} (kPa). The slope of the straight lines for each function has a downward trend with the ratio of $[C_{ps}/k]$ from 3.00×10^4 to 7.43×10^5, which means that the index would increase *S*% and σ_{sp}. Based on a graphical correlation method and the simple regression analysis, *S*% and σ_{sp} can be defined as

$$S\%=1E\text{-}05[C_{ps}/k]+1.89 \quad (R=0.943) \quad (4)$$

$$\sigma_{sp(FS)}=0.0013[C_{ps}/k]+194.06 \quad (R=0.934) \quad (5)$$

$$\sigma_{sp(CVS)}=0.0004[C_{ps}/k]+43.311 \quad (R=0.919) \quad (6)$$

where *S*% is the percentage swell; $\sigma_{sp(FS)}$ is the swell pressure for the FS test; $\sigma_{sp(CVS)}$ is the swell pressure for the CVS test; C_{ps} is the rate of primary swelling (*S*%/min); *k* is hydraulic conductivity (cm/sec).

Eq. (1-6) indicated that the simple correlations between the main swelling characteristics and the factors controlling them were especially evaluated in this study for the clay-sand mixtures. Whereas independent variables (controlling factors) are correlated one another in the simple correlation (or regression), multiple regression analysis is more advantageous than the simple regression analysis in order to determine the dependent major variables that can account for the variation in the dependent variables of *S*%, σ_{sp} and *PST*. Even though strong correla-

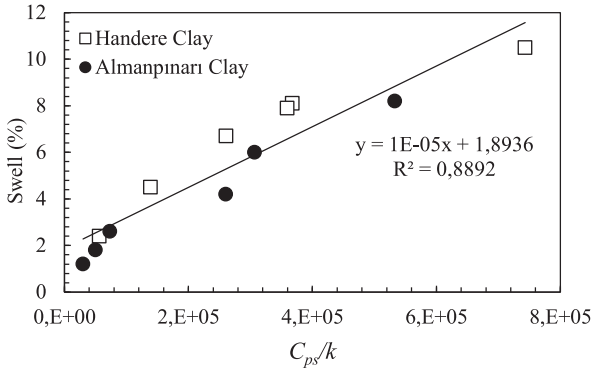

Figure 20. Relationship between the percentage swell and the ratio of the primary swelling rate to the hydraulic conductivity.

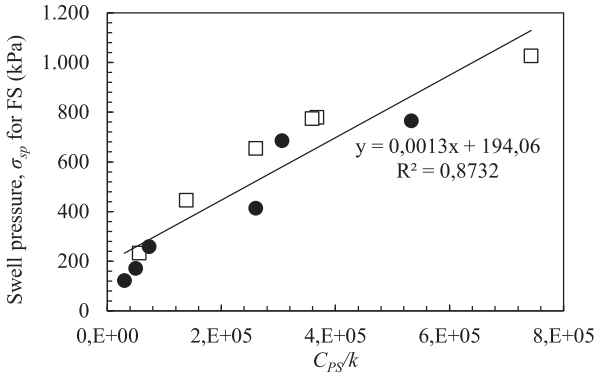

Figure 21. Relationship between the ratio of the primary swelling rate to the hydraulic conductivity and the swell pressure obtained from the FS test.

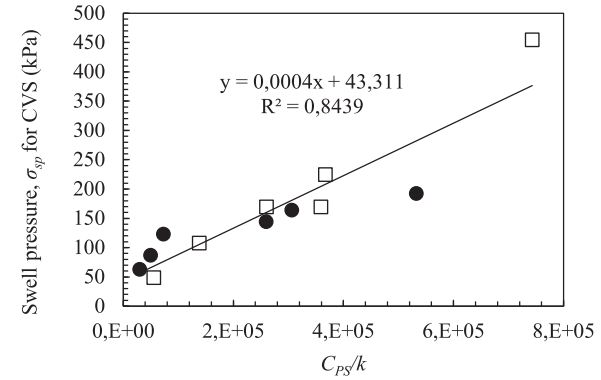

Figure 22. Relationship between the ratio of the primary swelling rate to the hydraulic conductivity and the swell pressure obtained from the CVS test.

tions among the controlling factors taken into account, in this investigation they were provided for Eqs. (1-6) and the related graphs, the multiple regression analysis were also conducted using two or three independent variables such as k, C_{ps} and the measured σ_{sp}. The multiple regression equations and their correlation coefficients are listed in Table 5. All the equations derived using the multiple regression analysis had strong correlations, ranging from 0.833 to 0.883. These data also indicate that the proposed regression relation expressions can quantifiably describe the relationship between the swelling characteristics of S%, σ_{sp} and PST, and the swelling parameters of k and C_{ps} , proposed firstly in this study.

6 DISCUSSION

The test results indicate that the increase in amount of sand in the clay decreases linearly the percentage swell (S%) and the swell pressures (σ_{sp}) obtained from both FS and CVS tests. The reduction of S% with sand addition is almost the same as the percentage for each clay type, and it can be suggested as a general expression that an increase in sand content of 10% leads to an almost 15% decrease in S%. However, the negative relationship between the sand content and σ_{sp} is linear, and it varies according to clay type. In addition to that, the difference between $\sigma_{sp(FS)}$ and $\sigma_{sp(CVS)}$ at the same sand content displays the differences depending on the clay type.

An examination of the relationship between S% and σ_{sp} indicates that, irrespective of the clay type and the sand content, there are strong positive linear correlations between them, especially for the swell pressure (σ_{sp}) values obtained from the FS tests (Fig. 8 and Table 4). Eqs. (1 and 2) derived from the correlations mentioned above can provide reliable predictions for the swell pressures of both $\sigma_{sp(FS)}$ and $\sigma_{sp(CVS)}$ using S% determined experimentally.

In this study, it is suggested that the primary swell time (PST) is a main swelling characteristic, such as S% and σ_{sp}, since approximately 90% of the swelling takes place in the primary swelling phase, and the completion time of this process could be important and critical for light engineering structures, i.e., motorways, railways, pipelines, and energy and water transmission lines, for which backfill applications are needed. In addition to PST, the rate of primary swelling (C_{ps}), the primary swelling phase's slope of the curve of S% vs. log time, is firstly used to predict the swelling characteristics as a parameter of the swelling process. An examination of the results indicates that C_{ps} vs. the swelling characteristics can be taken as linearly related, and C_{ps} can be confidently used in prediction formulas for swelling characteristics (Fig. 11-13 and Table 4-5).

Based on the correlations of k vs. the swelling characteristics (Fig. 15-16), it is shown that there are negative exponential relationships between k and S%, and σ_{sp} depending on the clay type. With an increase in k up

Table 5. Multiple regression analysis results.

Regression equation	Correlation (judgment) coefficient	Equation Number
S%=6.739-44035373.278k +143.416C_{ps}	R=0.857	(8)
$\sigma_{sp(FS)}$=644.403-4237790362.192k+15642.539C_{ps}	R=0.862	(9)
$\sigma_{sp(CVS)}$=0.457$\sigma_{sp(FS)}$+866084896.466k-2827.656C_{ps}-106.12	R=0.883	(10)
PST=1595.385-(8080928775.177)k-(43036.038C_{ps})	R=0.833	(11)

to 2.06×10^{-8} and 5.69×10^{-8} corresponding to the sand content of 20% for Handere clay and Almanpınarı clay, respectively, the swelling characteristics of the percentage swell and the swell pressures decrease dramatically. As can be seen in Fig. 17, a similar relationship and curve using all the data was obtained for *k* vs *PST*, which showed a steep decrease from 1.70×10^{-7} to 2.61×10^{-8} cm/sec with an increase in *PST* from 173 to 1040 min (from about 3 to 24 hours), and much less change for a further increase in *PST*. Thus, regardless of the clay type and fraction it is clear that *k* is directly a function of *PST*, and Eq. 3 derived from this strong correlation can provide a good estimation of *PST* using *k* (Fig. 17). The examination of *k* vs C_{ps} seen in Fig. 19 indicates that similar trends and negative exponential relationships exist, and *k* has a direct effect on C_{ps} depending on the clay type.

In order to provide general linear functions as prediction equations including, multi parameters, and without the variable of the clay type effect, the ratio of $[C_{ps}/k]$ as an indices was correlated to the main swelling characteristics of *S*% and σ_{sp}. Eqs. (4-6) having strong positive correlation coefficients ranging from 0.919 to 0.943 state that *S*% and σ_{sp} can be estimated rather closely to the experimental values by means of the indices of $[C_{ps}/k]$.

As can be seen in Table 5, the effect of *k* and C_{ps} on the swelling characteristics of *S*%, $\sigma_{sp(FS)}$, $\sigma_{sp(CVS)}$ and *PST* were analysed, and prediction equations with strong correlation coefficients ranging from 0.833 to 0.862 were obtained by means of multiple regression analysis method. The multiple regression analyses also indicate that *k* and C_{ps} are the parameters that directly affect the swelling, and can confidently be evaluated functions of swelling. Although the prediction equations of 8-11 (Table 5) derived from the multiple regression analyses have strong correlations, Eqs. (1-6) provided by simple regression analyses will most probably give more realistic results since they have stronger correlation coefficients, varying from 0.852 to 0.994 (Table 4) than those of Eqs. (8-11). Besides comparing the correlation coefficient, since *k* is a direct function of *PST*, the Eqs. (3) providing a prediction of *PST* will be more meaningful than Eqs. (11) as well.

Although the literature contains a number of empirical models for prediction of the swelling parameters, the relationships and predictive equations derived in this study are mainly about the effect of varying hydraulic conductivity, which depends on granulometric change, on the swelling behaviour of an expansive soil. Therefore, the predictive equations in the literature are not comparable to the equations proposed in this study.

Reliable swelling prediction equations (formulas) can contribute in terms of time and economy in engineering applications, such as road, railway and airport constructions on areas consisting of expansive soils that include a large number of checkpoints necessary for many costly and time-consuming test process. Utilizing more than one prediction method in drawing conclusions as to the swelling of an expansive soil is quite essential [25]. In this context, the results and examinations in this study introduce the fact that *k* and C_{ps} are also the parameters directly affecting the swelling behaviour of expansive soils depending on changing the gradation, and can be safely used in prediction formulas for swelling characteristics.

It should be pointed out that the above results and predictive equations were obtained using only two different high and moderate expansive clays, and limited to a range of uniform quartz sand content up to 50%. Although strong statistical relationships between *k* and C_{ps} , and swelling were obtained, further research is necessary to check the validity of these results and the derived equations for other soil types having different physic-mechanical properties.

7 CONCLUSIONS

Numerous series of laboratory tests were performed to investigate the effect of a change of uniform quartz sand content and of hydraulic conductivity caused by varying gradation on the swelling of compacted clay specimens. In order to realize such an objective comparative survey, two different clay soils were prepared for free-swelling tests and constant-volume swelling tests, and tested under similar conditions in accordance with the same technical standards. From the data and observations presented in this paper the following conclusions can be drawn:

1. The increase in the content of uniform quartz sand decreases almost linearly the percentage swell (*S*%). Regardless of the clay type, the addition of quartz sand by 10% leads to an average 15% reduction in the swelling percentage. The swell pressures that are obtained from both the free-swell tests and the constant-volume swell tests decreases linearly as the sand content increases as well; however, the amount of decrease is controlled by the clay type.
2. Based on correlations between the percentage swell and the swell pressures, irrespective of the clay type and the sand content, there are strong negative linear relationships between them. Prediction equations derived from these correlations can provide reliable predictions for swell pressures obtained from both the free-swell and constant-volume swelling tests using the values of the percentage swell (*S*%) determined experimentally.

3. The rate of primary swelling (C_{ps}), which is the primary swelling phase's slope of the curve of percentage swell vs. log time, corresponding to the swelling characteristics is discussed. The correlations indicate that the rate of primary swelling as a parameter of the swelling process can be safely used in the prediction of swelling characteristics such as the percentage swell, the swell pressure and the primary swelling time, in which almost 90% of swelling as strain occurs.
4. According to the correlations between the hydraulic conductivity (k) and the swelling characteristics controlled by a change in the gradation of a clay, both percentage swell and the swell pressures decrease exponentially with an increase of the hydraulic conductivity. On the other hand, the primary swelling time (*PST*), irrespective of the clay type, decreases as the hydraulic conductivity increases. Therefore, the primary swelling time can be reliably predicted using the correlation equations.
5. Based on the index that is the ratio of [C_{ps}/k] propounded to use multi parameters of swelling process, and to eliminate the effect of the clay type on swelling, considerable meaningful relationships having strong correlations between [C_{ps}/k] and the swelling characteristics have emerged. The prediction equations derived using the ratio of [C_{ps}/k] as an index can predict the swelling characteristics.

As an overall conclusion, this paper demonstrates that granulometric changing and hydraulic conductivity have an important influence on the swelling behaviour of cohesive soils. The relationships and formulas derived in this study are only valid for the varying gradation of a clay soil by adding uniform quartz sand up to 50%. In addition, the prediction formulas suggested in this study for compacted clay soils with various sand contents and hydraulic conductivities can be used safely in engineering practice.

REFERENCES

[1] Chen, F.H. 1988. Foundations on Expansive Soils. Elsevier Science Publishers, Amsterdam. The Netherlands.

[2] Basma, A.A. 1991. Estimating uplift of foundations due to expansion: a case history. Geotech. Eng. 22, 217–231.

[3] Nelson, D., Miller, D.J. 1992. Expansive Soils Problems and practice in Foundation and Pavement Engineering. John Wiley and Sons, NY. (ISBN: 978-0-471-18114-9)

[4] Ruwaih, I.A. 1987. Experiences with expansive soils in Saudi Arabia. Proceedings of the 6th International Conference on Expansive Soils. New Delhi, India, 317–322.

[5] Bell, F.G., Jermy, C.A. 1994. Building on clay soils which undergo volume changes. Architectural Sci. Rev. 37, 35–43. DOI:10.1080/00038628.1994.9697327

[6] Bell, F.G., Maud, R.R. 1995. Expansive clays and construction, especially of low-rise structures: a viewpoint from Natal, South Africa. Env. Eng. Geosci. I (1), 41–59. DOI:10.2113/gseegeosci.I.1.41

[7] Al-Homoud, A.S., Al-Suleiman, T.I. 1997. Loss in serviceability of pavements due to expansive clay subgrades. Env Eng Geosci. III (1), 277–294. DOI: 10.2113/gseegeosci.III.2.277

[8] Popa, A. 1997. Shrinkage-swelling phenomena effects on building. Proceedings of the International Symposium on Engineering geology and the Environment, Athens, Greece, 327–329.

[9] Derriche, Z., Iguechtal, L. 2000. Damage due to swelling soils in the region of In-Amenas: Algeria. Proceedings of GeoEng 2000, An International Conference on Geotechnical and Geological Engineering, Melbourne, Australia (on CD).

[10] Al-Shamrani, M.A., Dhowian, A.W. 2003. Experimental study of lateral restraint effects on the potential heave of expansive soils. Eng Geology. 69, 63–81. DOI:10.1016/S0013-7952(02)00248-X

[11] Erguler, Z.A., Ulusay, R. 2003. Engineering characteristics and environmental impacts of the expansive Ankara clay, and swelling maps for SW and central parts of the Ankara (Turkey) metropolitan area. Env. Geology 44, 8, 979-992. DOI:10.1007/s00254-003-0841-y

[12] Seed, H.B., Woodwart, R.J., Lundgren, R. 1962. Prediction of swelling potential for compacted clays. J. Soil Mech. Found. Div., ASCE, 88(4), 107-131.

[13] Komornik, A., David, D. 1969. Prediction of swelling pressure of clays. ASCE Proc. SM. FE. Div., 95 SM1, 209-225.

[14] Snethen, D.R. 1984. Evaluation of expedient methods for identification and classification of potentially expansive soils. Proceedings, 5th International Conference on Expansive Soils, Adelaide, 22–26.

[15] Sridharan, A., Rao, A.S., Sivapullaiah, P.V. 1986. Swelling pressure of clays. Geotech. Testing J., ASTM 9, 1, 24– 33. DOI: 10.1520/GTJ10608J

[16] Puppala, A., Punthutaecha, K., Vanapalli, S. 2006. Soil-water characteristic curves of stabilized expansive soils. J. Geotech. Geoenv. Eng. 132, 6, 736–751. DOI: 10.1061/(ASCE)1090-0241(2006)132:6(736

[17] Çokça, E. 2002. Relationship between methylene blue value, initial soil suction and swell percent of expansive soils. Turkish J. Eng. Environ. Sci. 26, 521-530.

[18] Chiappone, A., Marello, S., Scavia, C., Setti, M. 2004. Clay mineral characterization through the methylene blue test: comparison with other experimental techniques and applications of the method. Can. Geotech. J. 41, 1168-1178. DOI: 10.1139/t04-060

[19] Türköz, M., Tosun, H. 2011. The use of methylene blue test for predicting swell parameters of natural clay soils. Sci. Res. Ess. 6, 8, 1780-1792. DOI: 10.5897/SRE10.629

[20] Ranganatham, B.V., Satyanarayana, B. 1969. A rational method of predicting swelling potential, for compacted expansive clays. Proc. 6th Int.Conf. SM and FE, Canada 1, 92-96.

[21] Vijayvergiya, V.N., Ghazzaly, O.I. 1973. Prediction of

swelling potential of natural clays. Proceedings, 3rd Int. Research. and Eng. Conf. on Expansive Clays, 227–234.
[22] Nayak, N.V., Christensen, R.W. 1971. Swelling characteristics of compacted expansive soils. Clay and Clay Min. 19, 251-261.
[23] O'Neil, M.W., Ghazzally, O.I. 1977. Swell potential related to building performance. Journal of the Geotechnical Engineering Division, ASCE 103 (GT12), 1363–1379.
[24] Johnson, L.D., Snethen, D.R. 1978. Prediction of potential heave of swelling soils. Geotech. Testing J. 1, 117–124. DOI: 10.1520/GTJ10382J
[25] Kariuki, P.C., van der Meer, F. 2004. A unified swelling potential index for expansive soils. Eng. Geology 72, 1-8. DOI: 10.1016/S0013-7952(03)00159-5
[26] Weston, D.J. 1980. Expansive Roadbed Treatment for Southern Africa. Proceedings, 4th International Conference on Expansive Soils, 1, 339–360.
[27] Snethen, D.R. 1980. Characterization of expansive soils using soil suction data. Proceedings of the 4th International Conference on Expansive Soils, Boulder, Colorado, 18–23.
[28] Mowafy, M.Y., Bauer, G.E. 1985. Prediction of swelling pressure and factors affecting the swell behaviour of an expansive soil. Transport Res. Rec. 1032, 23-28.
[29] Rao, K.M., Babu, G.G., Rani, C.S. 2006. Influence of coarse fraction on swelling characteristics. E. J. Geotech. Eng. 11A, 0627.
[30] Erzin, Y., Erol, O. 2004. Correlations for quick prediction of swelling pressure. E. J. Geotech. Eng., 9F, 0476.
[31] Kariuki, P.C., van der Meer, F. 2003. Issues of effectiveness in empirical methods for describing swelling soils. International Journal of App. Earth Observation and Geoinformation 4, 231–241. DOI: 10.1016/S0303-2434(03)00005-9
[32] Yılmaz, I. 2006. Indirect estimation of the swelling percent and a new classification of soils depending on liquid limit and cation exchange capacity. Eng. Geology 85, 295–301. DOI:10.1016/j.enggeo.2006.02.005
[33] Rao, S.M., Ravi, K. 2015. Influence of initial degree of saturation on swell pressures of compacted Barmer bentonite specimens. Annals of Nuclear Energy 80, 303–311. DOI:10.1016/j.anucene.2015.02.019
[34] Dananaj, I., Frankovska, J., Janotka, I. 2005. The influence of smectite content on microstructure and geotechnical properties of calcium and sodium bentonites. App. Clay Sci. 28, 223-232. DOI: 10.1016/j.clay.2004.02.006
[35] ASTM D 854-10, 2010. Standard test methods for specific gravity of soil solids by water pycnometer. ASTM International, West Conshohocken, PA.
[36] ASTM D 422-63, 2007. Standard test method for particle-size analysis of soils. ASTM International, West Conshohocken, PA.
[37] ASTM D 4318-10, 2010. Standard test methods for liquid limit, plastic limit, and plasticity index of soils. West Conshohocken, PA.
[38] ASTM D 427–98, 2007. Standard Test method for shrinkage factors of soils by the mercury method. ASTM International, West Conshohocken, PA.
[39] Erdoğan, Y. 2015. Physicochemical Properties of Handere Clays and Their Use as a Building Material. Journal of Chemistry, ID:374245, 1-6. DOI: 10.1155/2015/374245
[40] Mirdallı, N., Halefoğlu, Y.Z., Sakarya, N. 2006. The investigation on the possible use of Almanpınarı red clay as a stain ceramics. J. Soc. Sci. Inst. Cukurova Uni. 15, 1, 229-234.
[41] ASTM D 698-07, 2012. Standard test methods for laboratory compaction characteristics of soil using standard effort (12,400 ft-lbf/ft3 (600 kN-m/m^3)). West Conshohocken, PA.
[42] ASTM D 4546, 1996. Standard test methods for one-dimensional swell or settlement potential of cohesive soils. ASTM International, West Conshohocken, PA.
[43] ASTM D2435, 2011. Standard test methods for one-dimensional consolidation properties of soils using incremental loading. ASTM International, West Conshohocken, PA.
[44] ASTM D 5856–95, 2002. Standard test method for measurement of hydraulic conductivity of porous material using a rigid-wall, compaction-mold permeameter. West Conshohocken, PA.
[45] Yule, D.F., Ritchie, J.T. 1980. Soil shrinkage relationships of Texas vertisols: 1 small cores. Soil Sci. Soc. Am. J. 44, 1285–1291. DOI:10.2136/sssaj1980.03615995004400060031x
[46] Gray, C.W., Allbrook, R. 2002. Relationships between shrinkage indices and soil properties in some New Zealand soils. Geoderma, 108, 3–4, 287–299. DOI:0.1016/S0016-7061(02)00136-2
[47] ElKholy, S.M. 2008. Improving the Characteristics of Expansive Soil Using Coarse-grained Soil. J. Eng. and Comp. Sci., Qassim Uni. 1, 71-81.
[48] Rao, M. 1988. A Proper Parameter for correlation of swell potential and swell index for remould expansive clays. M. Tech. Dissertation Submitted Dept. Civ. Eng., J.N.T.Uni. coll. Eng., Kakinada, India.
[49] Gürtuğ, Y., Banu, S., İklizler, M., Aytekin, M., Vekli, M. 2010. Prediction of swelling pressure of expansive soil stabilized with sand. Proceedings, 13th National Conference of Soil Mech. and Found. Eng. İstanbul Culture Uni. 793-802.
[50] Misra, A.K., Ohtsubo, M., Li, L., Higashi, T. 2011. Controlling factors of the swelling of various bentonites and their correlations with the hyraulic conductivity of soil-bentonite mixtures. App. Clay Sci. 52, 78-84. DOI:10.1016/j.clay.2011.01.033
[51] Cui, S-L., Zhang, H-Y., Zhang, M. 2012. Swelling characteristics of compacted GMZ bentonite-sand mixtures as a buffer/backfill material in China. Eng. Geology 141-142, 65-73. DOI:10.1016/j.enggeo.2012.05.004
[52] Smith, G.N. 1986. Probability and Statistic in Civil Engineering. Collins, London, 244.
[53] Sridharan, A., Gürtug, Y. 2004. Swelling behavior of compacted fine-grained soils. Eng. Geology 72, 9–18. DOI: 10.1016/S0013-7952(03)00161-3
[54] Feda, J. 1991. Creep of Soils. Elsevier, Amsterdam, 269.
[55] Komine, H. 2010. Predicting hydraulic conductivity of sand–bentonite mixture backfill before and after swelling deformation for underground disposal of radioactive wastes. Eng. Geo. 114, 123–134. DOI: 10.1016/j.enggeo.2010.04.009

DOLOČANJE KRIVULJE ZRNAVOSTI NEVEZLJIVIH ZEMLJIN Z UPORABO SLIKOVNE ANALIZE

Nihat Dipova
Akdeniz University,
Department of Civil Engineering
Antalya, Turčija
E-pošta: ndipova@akdeniz.edu.tr

Ključne besede

slikovna analiza, obdelava slike, velikost zrna, pesek

Izvleček

Tehnologija obdelave slik vključuje shranjevanje slik predmetov na računalnik in njihovo obdelavo z računalnikom za določen namen. Slikovna analiza je številčni izraz slikovne podobe predmetov s posnemanjem delovanja človeškega očesa in ustvarjanje številčnih podatkov za izračune, ki bodo izvedeni kasneje. Digitalna slikovna analiza zagotavlja možnost za hitro merjenje, za številne parametre inženirskih materialov lahko takšno merjenje zagotovimo v skoraj realnem času. Slikovna analiza se v geotehnični inženirski praksi uporablja šele kratek čas. Krivulja zrnavosti in oblika zrn sta temeljni lastnosti, ki se uporabljata za razlago izvora in obnašanja zemljin. Mehansko sejanje ima nekatere omejitve, npr.: ne meri se osna dimenzija delca, ni upoštevana oblika delcev, in zlasti za podolgovate in ploščate delce s sejalno analizo ne dobimo zanesljivih razmerij zrnavosti. V tej študiji je bila porazdelitev velikosti zrn peska določena z uporabo tehnike slikovne analize, uporabljeni so bili preprost aparat, neprofesionalne kamere in odprto-kodna programska oprema. Analiza se izvede tako, da se vzorec postavi na pregledno ploščo, ki je z ozadja osvetljena z belo osvetlitvijo. Digitalne slike se dobijo s pomočjo CCD DSLR kamere. Segmentacija delcev se dobi z nastavljanjem pragov slike, binarno kodo in označevanjem delcev, geometrijske meritve posameznega delca pa z uporabo avtomatizirane tehnike štetja slikovnih pik. Lokalni stiki ali omejeno prekrivanje so bili premagani s pomočjo transformacijske tehnike ločevanja. Isti vzorec je bil testiran s tradicionalno sejalno analizo. Primerjave rezultatov kažejo, da se krivulji zrnavosti dobljeni s slikovno in sejalno analiza dobro ujemata.

DETERMINING THE GRAIN SIZE DISTRIBUTION OF GRANULAR SOILS USING IMAGE ANALYSIS

Nihat Dipova
Akdeniz University,
Department of Civil Engineering
Antalya, Turkey
E-mail: ndipova@akdeniz.edu.tr

Keywords

image analysis, image processing, grain size, sand

Abstract

Image-processing technology includes storing the images of objects in a computer and processing them with the computer for a specified purpose. Image analysis is the numerical expression of the images of objects by means of mimicking the functioning of the human visual system and the generation of numerical data for calculations that will be made later. Digital image analysis provides the capability for rapid measurement, which can be made in near-real time, for numerous engineering parameters of materials. Recently, image analysis has been used in geotechnical engineering practices. Grain size distribution and grain shape are the most fundamental properties used to interpret the origin and behaviour of soils. Mechanical sieving has some limitations, e.g., it does not measure the axial dimension of a particle, particle shape is not taken into consideration, and especially for elongated and flat particles a sieve analysis will not yield a reliable measure. In this study the grain size distribution of sands has been determined following image-analysis techniques, using simple apparatus, non-professional cameras and open-code software. The sample is put on a transparent plate that is illuminated with a white backlight. The digital images were acquired with a CCD DSLR camera. The segmentation of the particles is achieved by image thresholding, binary coding and particle labeling. The geometrical measurements of each particle are obtained using an automated pixel-counting technique. Local contacts or limited overlaps were overcome using a watershed split. The same sample was tested by traditional sieve analysis. An image-analysis-based grain size distribution has been compared with a sieve-analysis distribution. The results show that the grain size distribution of the image-based analysis and the sieve analysis are in good agreement.

1 INTRODUCTION

Researchers in the geotechnical community understand that heterogeneity is a basic characteristic of geomaterials and employ considerable efforts for these heterogeneity problems. The grain size distribution (GSD) is one of the basic and most important properties of granular soils that exhibit heterogeneity. It is used in soil classification systems (such as USCS, AASHTO) and empirical estimation equations to estimate the permeability, shear strength, deformability and compactability. GSD is very important for geotechnical engineering. In site investigations of large engineering structures, in earthquakes and liquefaction research and before filter material selection, it is necessary to make a number of GSD analyses. The gradation of the in-situ soil often controls the groundwater drainage of the site. A poorly

graded soil will have better drainage than a well graded soil. When a fill material is being selected for a highway embankment or an earthen dam, the soil gradation is considered. A well-graded soil can be compacted more than a poorly graded soil. These types of projects may also have gradation requirements that must be met before the soil to be used is accepted. When options for ground-remediation techniques are being selected, the soil gradation is a controlling factor. In addition to geotechnical applications in geological and agricultural studies, GSD is widely used.

There are two common test methods to determine the GSD: mechanical sieving for the coarse-grained soils and sedimentation tests (pipette and hydrometer methods) for the fine-grained soils. In sieve analysis, the particle size is determined by a dimension that represents the sieve aperture through which the particle passes. Although the size distribution can be obtained roughly, the shape of a grain cannot be taken into consideration in these traditional methods. Moreover, sample drying before the test and the sieving procedure make this method time and effort consuming; hence, it is an expensive method. Digital image analysis would be a practical alternative to make GSD measurements easier.

Digital image analysis extracts information from objects that are captured by an imaging system. The digital image processing and analysis techniques can be summarized in four basic steps: taking photographs with a digital camera, storing the image file as a digital file, image processing to edit the digital images for specific analysis, and analysis of the modified image to quantify the properties of an object. Digital image processing and analysis are used for detailed works of many disciplines, including medicine, genetics, biology, textiles, food science, geology, physics, chemistry, agriculture, forestry, mining, computer engineering, civil engineering and environmental sciences. In the past decade image-analysis techniques have been used with increasing intensity in areas of geotechnical engineering such as deformation measurements [1, 2], failure analysis [3], porosity analysis [4, 5], grain size and shape analysis [6, 7, 8, 9, 10] and the determination of geotextile properties [11].

In this study the grain size distributions of sands are determined using a mechanical method with traditional sieves and image-analysis techniques using simple apparatus and consumer-grade cameras. A new approach to determine the mass-based distribution from 2D images is introduced. The results of these two techniques are compared. The advantages and limitations of the image-analysis-based grain size distribution determination are evaluated.

2 IMAGE PROCESSING AND ANALYSIS

Digital image processing (DIP) is the use of computer algorithms to create, process, communicate, and display digital images for specified purposes. After the processing of the digital images, digital image analysis (DIA) techniques are used for measurement, classification, database and statistical purposes. Some properties of the numbers of objects in an image (shape, dimension, area, location, boundary properties etc.) can be determined easily by means of DIA. Most DIP and DIA studies are based on binary modeling. A binary model consists of pixels that are quantized using only two values, 0 and 1, representing the full black and the full white colors, respectively. Editing of the binary images is often required to enhance the delineation of the individual object.

There are many types of software used for filtering, color and contrast adjustment, measurement, and classification. ImageJ [12] is commonly used image-processing and analysis software that was developed as a Java-based program by the National Institutes of Health (NIH). ImageJ and similar programs (e.g., Scion Image, ImageTool, Digimizer, Clemex, Image Pro Plus) are being used to solve numerous tasks in scientific disciplines, including the analysis of geo-materials (e.g., Szramek et al, [13], Polacci et al., [14]). These softwares are designed to process input images that can include rectangular raster files (e.g., *.tiff, *.jpg, *.gif, etc.) encoded in 8-bit grey-scale formats.

Developments in digital-imaging technology and image-processing/analysis software have provided the means for the development of new methods for particle size analysis based on image analysis [15, 16, 17, 18, 19]. In addition to a grain size distribution, using the digital image-analysis techniques other soil grain characteristics, such as sphericity, particle elongation, roundness, etc. can be readily quantified [20].

3 GRAIN SIZE OF GRANULAR SOILS

The grain size and shape are the most fundamental properties used to interpret the origin and behaviour of soils. Grain size distribution (GSD), also known as gradation, refers to the proportions by dry mass of a soil distributed over specified particle size ranges. Although there are several methods for measuring the GSD of fine-grained soils (such as pipette, hydrometer, laser diffraction, X-ray sedimentation), for the GSD of granular soil there is no current method more practical than sieve analysis. Laser diffraction can be used for

fine sands, but it cannot work over 3 mm in size and the amount of sample tested is very small. Therefore, the sieve analysis is an indispensable and widely used method in geotechnical applications.

Mechanical sieving is a simple method that is commonly used in the civil engineering disciplines. Although the size distribution can be obtained roughly, the shape of a particle is not easy to describe in simplified terms. The size of a spherical object or a cube can be described with one dimension; however, the particles in a soil mass are irregular and nonuniform in shape in general. In a sieve analysis, the size of a particle is related to the size of the square aperture in which the particle passes. The size distribution is calculated based on the mass of all the particles retained on a sieve. The method has some limitations; it does not measure the axial dimension of a particle [19]. Particle shape is not taken into consideration, especially for elongated and flat particles a sieve analysis will not yield a reliable measure [21, 22, 23, 24].

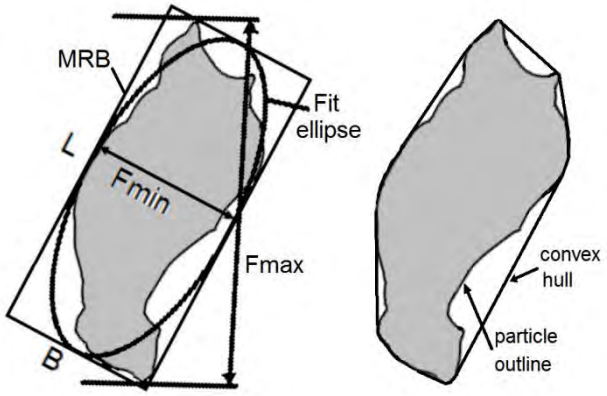

Figure 1. Dimension terms; F_{min}: Minimum Ferret's diameter, F_{max}: Maximum Ferret's diameter, MBR: Minimum bounding rectangle, B: Width, L: Length. Fit ellipse: Ellipse which fit in a MBR.

In reality, irregular particles need to be measured with more than one dimension. The maximum Ferret's diameter, F_{max} (also known as the maximum caliper) is the longest distance between any two points along the particle boundary. Similarly, the minimum caliper diameter of the particle is the minimum Ferret's diameter (F_{min}). The minimum bounding rectangle (MBR), also known as the bounding box, is an expression of the maximum extents of a 2-dimensional object that fits in a rectangle. The dimensions of the MBR can be used to obtain the dimensions of the fit ellipse (the ellipse that fits into the MBR) (Figure 1). Rectangularity and ellipticity are two index parameters that define the shape similarity of a particle to a rectangle or ellipse, respectively. A simple approach to measuring rectangularity is to use the ratio of the area of the region to the area of its minimum bounding rectangle (MBR). Similarly, ellipticity is the ratio of the area of the region to the area of an ellipse that fits in the minimum bounding rectangle (MBR).

4 METHODOLOGY

4.1 Imaging and Processing

The experimental arrangement used in the present work is simple and inexpensive. Figure 2 shows a schematic diagram of the imaging system. Sand samples to be analyzed were washed on a 0.075 mm sieve using tap water and dried in an oven. In practice an air-dried sample is adequate. The sand sample is put on a transparent glass plate that is illuminated with a white backlight. A high contrast between the soil grains and the background is supplied by backlight illumination. An upright mounted light and diffuser white plate under the glass plate provide uniform illumination and maintain a sufficient contrast. To increase the total image size

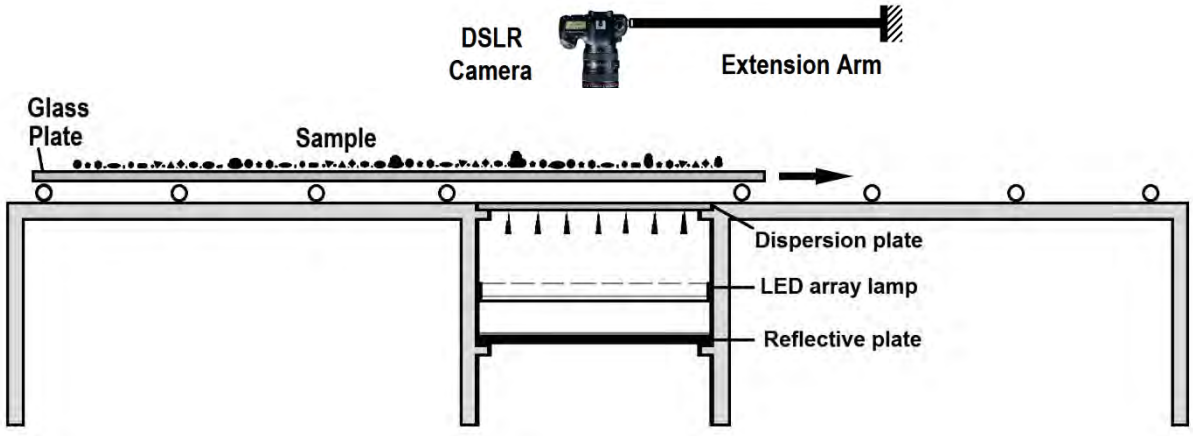

Figure 2. Experimental Set-Up.

without reducing the resolution, stitching consecutively taken pictures into a long strip picture provides a practical solution. In this technique, a camera that is mounted on a stage takes pictures continuously, while the glass plate moves laterally (Figure 2). The images of adjacent fields should be captured with at least a 30 % overlap.

Digital images have been acquired with a charged-coupled device (CCD) camera having a 15-megapixels resolution. To maintain high quality, a vibration-reduction (VR) lens and a remote-control device were used. Due to electronic noise in the camera system or nonuniformity in the background, random noise (dirt) occurs on an RGB (color) image. This problem can be effectively eliminated by filtering these noises, using noise-reduction filters. The segmentation of the particles is achieved by image thresholding, binary coding and particle labeling. The initial color image is converted into a binary image in which the particles are set to black (0), while the background is set to white (1).

Having a clear binary image after image processing, the geometrical measurements of each particle can be made by pixel counting. The true dimensions are determined by scaling. The soil sample should be placed sparsely, such that all individual grains should not overlap with each other. An overlap of the grains in the sample results in agglomeration. Local contacts or limited overlaps can be overcome using "watershed analysis", which has been proposed to determine the boundaries of objects in digital images [25, 26]. In the case of the crowded placement of particles, watershed analysis may not be sufficient or lead to reduced individual particle sizes.

4.2 Calculations

The chain code (Freeman chain code) and mid-crack code are popular coding techniques for determining the outline of binary images. These codes encode the boundary of the object as a sequence of steps, from pixel to pixel, all around the object. The chain code moves along the center of the border pixels, while the crack code moves along a sequence of "cracks" between two adjacent border pixels. In both ways the outline is a connected sequence of straight-line segments with specified lengths and directions (Figure 3).

The chain code is disadvantageous when the area and perimeter of a particle is to be calculated. The inside chain code underestimates the area and perimeter, while the outside chain code overestimates them. The mid-crack code in area and perimeter computation results in a lower error value compared to the chain code and therefore the mid-crack code may be desirable in outline tracing [27]. However, if the backlight is used, such as in our case,

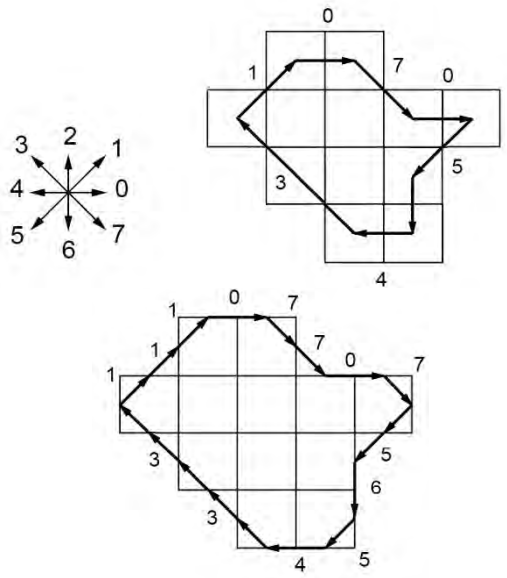

Figure 3. (a) 8 code words represent 8 directions (8-neighborhoud), (b) The Freeman chain code of the object, (c) The mid-crack code of the object.

the situation is reversed. The measured area of a particle based on pixel counting will be larger than the true particle area. When a backlight is used the background pixels have a gray-scale value equal to just 255. If a particle boundary intersects a background pixel, the projected light is diminished and its gray-scale value will be less than 255. Thus, Raschke and Hryciw [15] calculated the true particle area as equal to the pixel counted area minus one half the areas of the boundary pixels. Actually, this can be achieved by using the Freeman chain code approach instead of the mid-crack code. In this study the particle outlines were drawn using the chain code and the areas of this outline were calculated accordingly.

Using image-analysis techniques the projection areas of individual particles are calculated automatically. An area-based particle size distribution can be obtained easily; however, a mass-based distribution would be more realistic. The problem here is the pictures are in two dimensions and a measurement of the particle thickness is impossible. A uniform particle shape in soils such as a cube or a sphere is rare. However, soil particles are nonuniform, most of the particles have resemblance to standard geometries such as cube, prism, sphere and ellipsoid. In fact a cube is a rectangular prism with three equal dimensions. Similarly, a sphere is a special case of an ellipsoid. Therefore, the volume of particles similar to an ellipse and a rectangle projection area can be calculated automatically.

If soil particles are dropped onto a horizontal plane, they will always drop on their smallest dimension perpendic-

ular to that plane. Therefore, particle thickness should be the minimum dimension of a particle. The thickness and volume of particles cannot be obtained directly from the 2D images. Based on the assumption that particles from the same source should have more or less the same shape characteristics [16], the mean thickness of a particle from the breadth of the particle can be estimated as:

$$Mean\ thickness = breath \cdot \left[\frac{M}{\rho \cdot \sum_{i=1}^{n} (breath \cdot area)} \right] \quad (1)$$

where M is the total mass of the aggregate sample.

In Mora and Kwan's approach [16] the particle shape is supposed to be a polygonal prism. In reality the particle shape is irregular in 3D. However, some particles look like an ellipsoid (a sphere is a special form of an ellipse) and some a rectangular prism (a cube is a special form of a rectangle) (Figure 4). This assumption is more realistic and results in a smaller error.

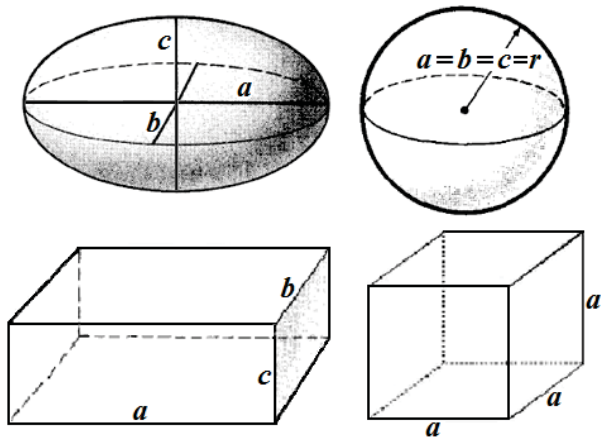

Figure 4. Ellipsoid (a sphere is a special form of ellipsoid) and rectangular prism (a cube is a special form of rectanglular prism) assumption for soil particles.

In 2D image analysis the rectangularity and ellipticity of the particles can be calculated. Therefore, in this study the volume of the particles have been calculated for ellipsoidal shape if the ellipticity is higher than the rectangularity, otherwise the volume is calculated for a rectangular prismatic shape. Initially, the thickness of particles is assumed to be equal to the medial dimension (b). The density of dry sand ranges between 2.64 and 2.67 g/cm^3, and a calculation of the mass, taking the dry density equal to 2.65, is reasonable. Dividing the weighted mass of the whole soil sample to a cumulative mass calculated according to the way explained above, a correction factor will be obtained (bracket in equation 1). Multiplying this by a medial dimension (b) of every individual particle, the thickness can be estimated (Equation 2).

$$Thickness = \left[\frac{M}{\rho \cdot \sum_{i=1}^{n} (volume)} \right] \cdot b \quad (2)$$

The grain size distribution curve is drawn as a semi-logarithmic graph of percent passing - particle diameter. In a sieve analysis the particle diameter is assumed to be equal to the sieve opening. In reality, the medial dimension or minimum Ferret's dimension of a particle in 2D passes through the diagonal of a square sieve aperture (Figure 5a). Therefore, the equivalent particle diameter (D_e) for 2D analysis should be calculated as;

$$D_e = F_{\min} / \sqrt{2} \quad (3)$$

(Figure 5a). In this study the images of particles are assumed to be ellipsoid or a rectangular prism according

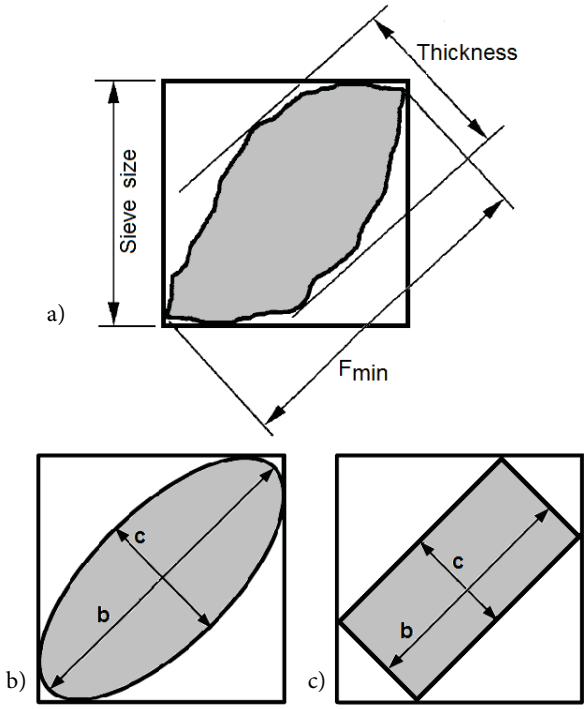

Figure 5. a) Minimum Ferret's dimension of a particle may pass through the diagonal of square sieve aperture, b) Ellipsoid assumption, c) Rectangular prism assumption.

to the shape similarity of a particle to an ellipse or a rectangle, respectively. Therefore, the equivalent particle diameter (D_e) should be:

$$D_e = \sqrt{\left(0.5 \cdot \left(b^2 + c^2\right)\right)} \quad (4)$$

for an ellipsoid (Figure 5b) and

$$D_e = \left(b + c\right) / \sqrt{2} \quad (5)$$

for a rectangular prism (Figure 5c).

4.3 Mechanical (sieve) analysis

A grain-size distribution by sieve analysis was performed in accordance with the procedure suggested by ASTMD422-63 [28]. Traditional grain-size distribution curves based on a sieve analysis are shown in figures 6-11.

5 RESULTS AND DISCUSSION

Six different samples were analyzed (Table 1). A 24 MP CCD DSLR camera, 300 mm / macro lens and remote control were used for the photography. In the binary images the grains were numbered and geometrical

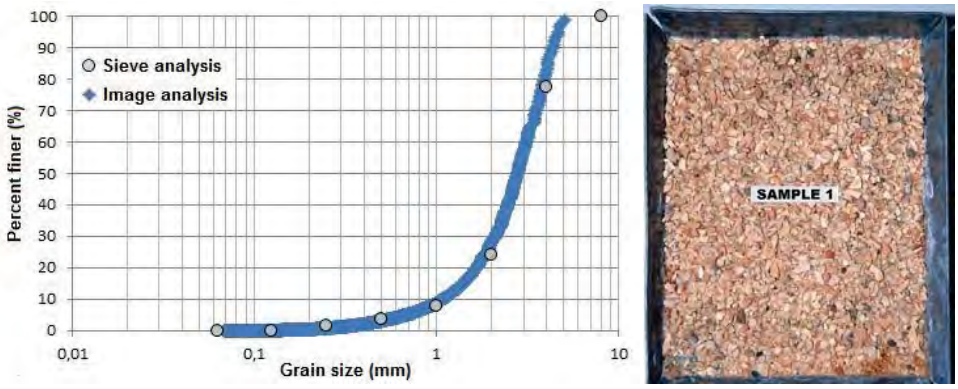

Figure 6. Comparison of sieve analysis and image analysis results for sample 1.

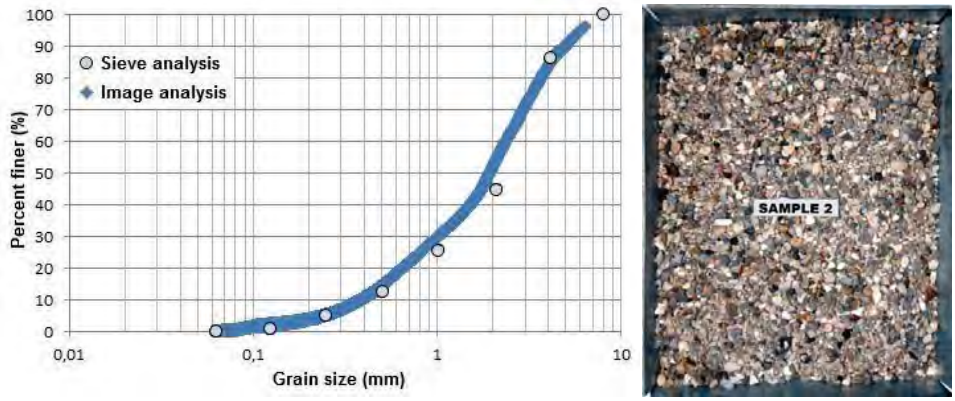

Figure 7. Comparison of sieve-analysis and image-analysis results for sample 2.

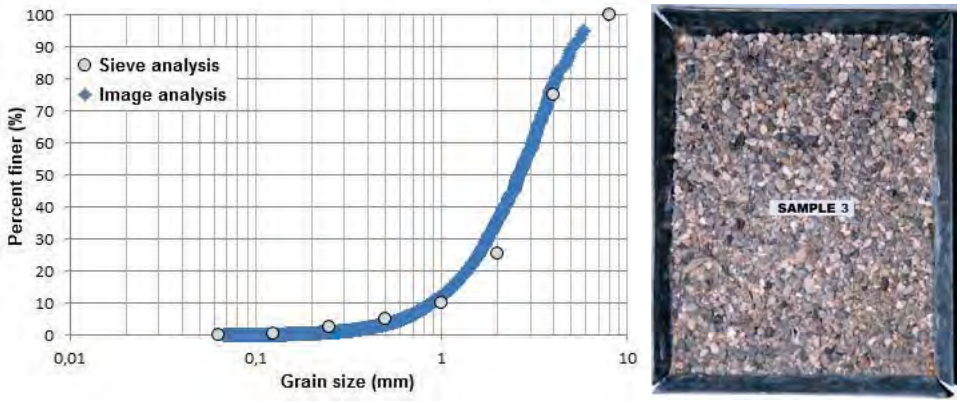

Figure 8. Comparison of sieve-analysis and image-analysis results for sample 3.

measurements of the grains were made automatically. F_{max}, F_{min} , the minimum boundary rectangle (MBR) and area measurements were made. The volume calculations were carried out with the assumption of a rectangular prism and ellipsoid. For every grain the equivalent grain size and percent finer values were calculated and plotted on semi-logarithmic graphs (Figure 6-11). The soil samples were also tested using a conventional sieve analysis technique for comparison purposes. Most parts of the grain size distributions determined using the sieve analysis and the image analysis are in good agreement.

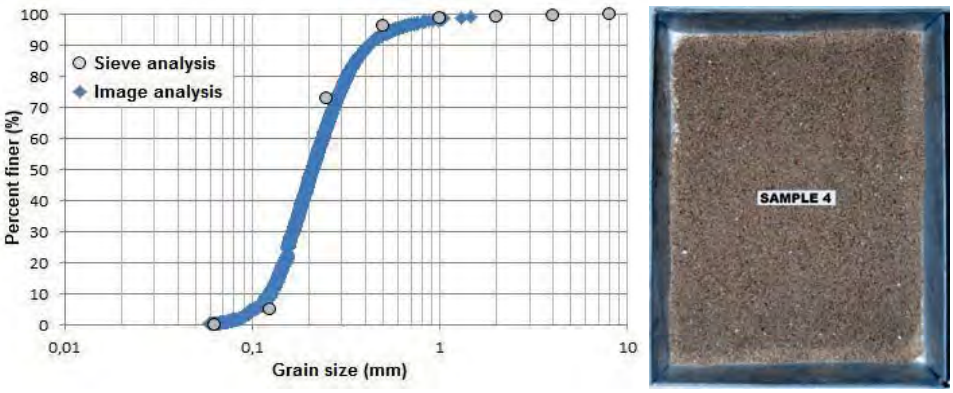

Figure 9. Comparison of sieve analysis and image analysis results for sample 4.

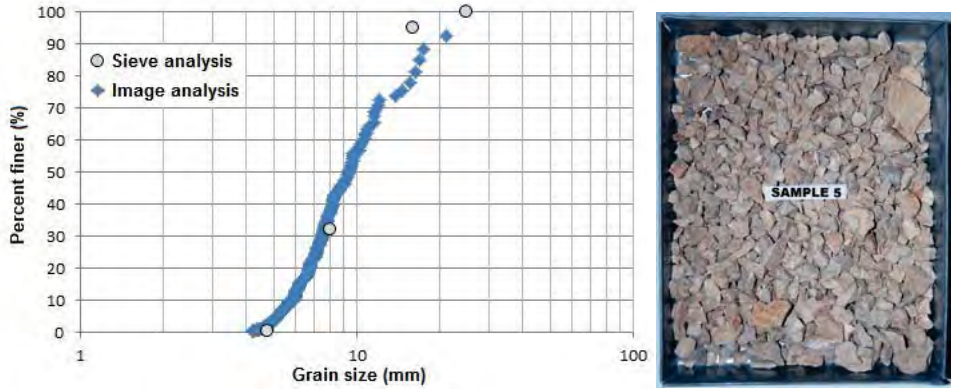

Figure 10. Comparison of sieve-analysis and image-analysis results for sample 5.

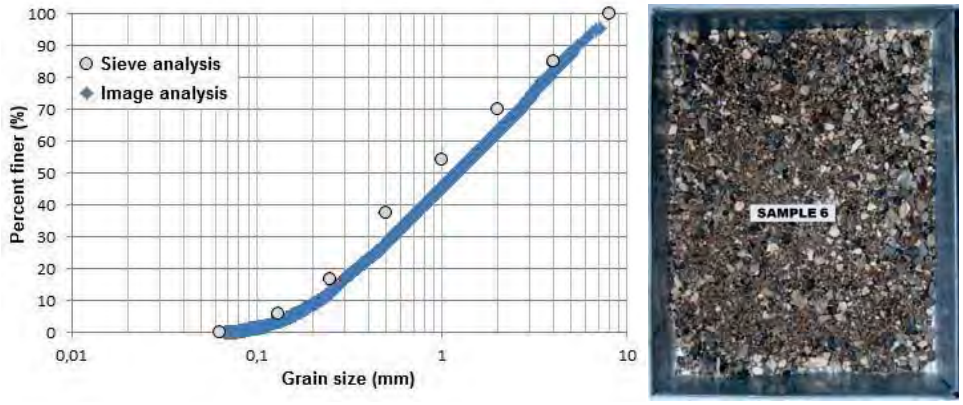

Figure11. Comparison of sieve-analysis and image-analysis results for sample 6.

Table 1. Summary of measurements made by image-analysis method.

#	D_{10} (mm)	D_{30} (mm)	D_{60} (mm)	C_u	C_c	Soil class (USCS)	Number of grains	L_{max} (mm) *	L_{mean} (mm) *	L_{min} (mm) *	Mass (g)
1	1.10	2.05	3.00	2.72	1.27	SP	25163	12.74	0.48	0.08	18.31
2	0.37	1.05	2.30	6.21	1.29	SW	71245	10.62	0.40	0.08	14.69
3	1.00	2.10	3.00	3.00	1.47	SP	31318	17.77	0.48	0.08	17.23
4	0.14	0.17	0.22	1.57	0.94	SP	100981	2.77	0.25	0.08	2.06
5	6.00	7.80	10.0	1.67	1.01	GP	246	38.08	13.21	6.07	225.2
6	0.20	0.40	1.20	6.05	1.03	SW	65245	11.32	0.42	0.08	14.26

* L_{max}, L_{mean}, L_{min} : Maximum, mean and minimum values of maximum grain dimension (L)

In contrast to a sieve analysis, in the image analysis method a fully dried sample is not required. In the air dry condition to allow grains to scatter is enough. This means both energy and time saving. Volume and mass determinations are necessary to obtain grain size curves analogous to the sieve analysis. Area based distributions are not realistic. The image analysis software used should enable measurements of geometrical features other than the perimeter and the area (such as Ferret's dimensions, MBR etc). If the target is to obtain a GSD curve analogous to sieve analysis, by using the methodology given in this study, the width of the grain (B or F_{min}) is utilized as an equivalent dimension. Otherwise, we can plot GSD curves freely by taking any dimension of the grains, such as F_{max} , L or the mean dimension.

A uniformly distributed backlight intensity is crucial. At the start of the study incandescent light bulbs, fluorescent bulbs and fluorescent bars were tried. Even using a thick dispersion plate, a uniform light intensity was not possible. A nonuniform light intensity causes a nonuniform background, and during binary coding, dark-gray portions of the background may be coded as a grain. Bulb lamps located at the centre caused a shadow under large grains located at the sides. Finally, a cool white LED array lamp having dimmer power adjustment gave the best results. In this way an uniform light intensity is possible and the grain shadows are eliminated.

6 CONCLUSIONS

1) This study shows that the grain size distributions of sands can be determined via image-analysis techniques and using a simple setup and a consumer-grade camera. The results of the image analysis were compared with conventional sieve analysis results. The distribution determined by the sieve analysis was concluded to be compatible with the conventional sieve analysis.
2) The image analysis used for the grain size distribution practice has advantages over conventional sieve analysis. While in sieve analysis the percentages for a certain range of grain size are determined, in the image-analysis method determining all the size properties of the each grain is possible.
3) The equivalent size in the sieve analysis can only be related to the median size of the grain. This is a limitation of the sieve method. However, in the image analysis the grain size distribution can be made for any of the grain dimensions.
4) Despite these advantages, the main limitation of the image-analysis method is the insufficiency of tests to represent the whole soil mass due to the use of a small amount of samples. This issue can be overcome by doing successive tests or increasing the length of the sliding table. In this case we need to spend more time and effort compared to previous, but this can be solved by improving the apparatus and writing special computer programs. This work hopes to be a first step towards the development of GSD application for image analysis and future work will include an improvement of the technique.

Acknowledgements

This study was supported by Akdeniz University (Antalya, Turkey), The Scientific Research Projects Coordination Unit (Project code: 2012.01.0102.011). This financial support is gratefully acknowledged.

REFERENCES

[1] Alshibli, K.A., Batiste, S.N., Sture, S. 2003. Strain localization in sand: plane strain versus triaxial compression. Journal of Geotechnical and Geoenvorimental Engineering, ASCE 129(6), 483-494. DOI: 10.1061/(ASCE)1090-024

[2] Alsaleh, M.I., Alshibli, K.A., Voyiadjis, G.Z. 2006. Influence of micromaterial heterogeneity on strain localization in granular materials. International Journal of Geomechanics, ASCE 6, 4, 248-259.

DOI: 10.1061/(ASCE)1532-3641

[3] Alshibli, K.A., Sture, S. 1999. Sand shear band thickness measurements by digital imaging techniques. Journal of Computing in Civil Engineering 13, 2, 103-109. DOI: 10.1061/(ASCE)0887-3801

[4] Bhatia, S., Soliman, A. 1990. Frequency distribution of void ratio of granular materials determined by an image analyzer. Soils and Foundations 30, 1, 1-16. DOI:10.3208/sandf1972.30.1

[5] Kuo, C.Y., Frost, J.D. 1996. Uniformity evaluation of cohesionless specimens using digital image analysis. ASCE Journal of Geotechnical and Geoenvironmental Engineering 122, 5, 390–396. DOI: 10.1061/(ASCE)0733-9410

[6] Alshibli, K.A., Alsaleh, M.I. 2004. Characterizing surface roughness and shape of sands using digital microscopy. Journal of Computing in Civil Engineering 18, 1, 36-45. DOI: 10.1061/(ASCE)0887-3801

[7] Masad, E., Saadeh, S., Rousan, T.A., Garboczi, E., Little, D. 2005. Computations of particle surface characteristics using optical and X-ray CT images. Computational Materials Science 34, 406-424. DOI: 10.1016/j.commatsci.2005.01.010

[8] Al-Rousan, T., Masad, E., Tutumluer, E., Pan, T. 2007. Evaluation of image analysis techniques for quantifying aggregate shape characteristics. Construction and Building Materials 21, 978–990. DOI: 10.1016/j.conbuildmat.2006.03.005

[9] Ohm, H., Hryciw, R. 2014. Size Distribution of Coarse-Grained Soil by Sedimaging. J. Geotech. Geoenviron. Eng. 140, 4, 04013053. DOI: 10.1061/(ASCE)GT.1943-5606.0001075

[10] Araujo, G.S., Bicalho, K.V., Tristao, F.A. 2015. Use of image analysis to determine the shape and texture of sands. Revista Brasileira De Ciencia Do Solo 39, 1, 94-99. DOI: 10.1590/01000683rbcs20150274

[11] Aydilek A.H., Kutay, M.E., Sparacino, R., Dafla, H. 2007. Image Analysis for QC/QA of Geosynthetic Deformation during Wide Width Tensile Testing. Proceedings of Geosynthetics 2007, Washington, D.C., 6 p.

[12] Rasband, W.S. 2005. ImageJ, U. S. National Institutes of Health, Bethesda, Maryland, USA.

[13] Szramek, L., Gardner, J.E., Larsen, J. 2006. Degassing and microlite crystallization of basaltic andesite magma erupting at Arenal Volcano, Costa Rica. Journal of Volcanology and Geothermal Research 157, 182–201. DOI: 10.1016/j.jvolgeores.2006.03.039

[14] Polacci, M., Baker, D.R., Mancini, L., Tromba, G., Zanini, F. 2006. Three-dimensional investigation of volcanic textures by X-ray microtomography and implications for conduit processes. Geophysical Research Letters 33, L13312, 1-5. DOI: 10.1029/2006GL026241

[15] Raschke, S. A., Hryciw, R. D. 1997. Grain-size distribution of granular soils by computer vision. ASTM Geotech. Testing Journal 20, 4, 433–442. DOI: 10.1520/GTJ10410J

[16] Mora, C.F., Kwan, A.K.H., Chan, H.C. 1998. Particle Size Distribution Analysis Of Coarse Aggregate Using Digital Image Processing. Cement and Concrete Research 28, 6, 921–932. DOI: 10.1016/S0008-8846(98)00043-X

[17] Ghalib, A.M., Hryciw, R.D. 1999. Soil particle size distribution by mosaic imaging and watershed analysis. Journal of Computing in Civil Engineering 13, 2, 80-87. DOI: 10.1061/(ASCE)0887-3801

[18] Mora, C.F., Kwan, A.K.H. 2000. Sphericity, Shape Factor, and Convexity Measurement of Coarse Aggregate for Concrete Using Digital Image Processing. Cement and Concrete Research 30, 3, 351-358. DOI: 10.1016/S0008-8846(99)00259-8

[19] Mertens, G., Elsen, J. 2006. Use of computer assisted image analysis for the determination of the grain-size distribution of sands used in mortars. Cement and Concrete Research 36, 1453-1459. DOI: 10.1016/j.cemconres.2006.03.004

[20] Kuo, C.Y., Frost, J.D., Lai, J.S., Wang, L.B. 1996. Three-Dimensional Image Analysis of Aggregate Particles from Orthogonal Projections. Transportation Research Record 1526, 98-103. DOI: 10.3141/1526-12

[21] Fernlund, J.M.R., Zimmerman, R.W., Kragic, D. 2007. Influence of volume/mass on grain-size curves and conversion of image-analysis size to sieve size. Engineering Geology 90, 124–137. DOI: 10.1016/j.enggeo.2006.12.007

[22] Allen,T. 1968. Particle size measurement, Chapman and Hall, London.

[23] Pettijohn F.J. 1984. Sedimentary Rocks. S.K. Jain, India.

[24] Fernlund, J.M.R. 1998. The effect of particle form on sieve analysis: a test by image analysis. Engineering Geology 50, 111-124. DOI: 10.1016/S0013-7952(98)00004-0

[25] Vincent, L. 1991. Morphological transformations of binary images with arbitrary structuring elements. Signal Processing 22, 1, 3–23. DOI: 10.1016/0165-1684(91)90025-E

[26] Vincent, L., Soille, P. 1993. Watersheds in digital spaces, an efficient algorithm based on immersion simulations. IEEE Trans. Pattern Anal. and Machine Intelligence 13, 6, 583–598. DOI: 10.1109/34.87344

[27] Dunkelberger, K. A., Mitchell, 0. R. 1985. Contour tracing for precision measurement. Proc. IEEE Inter Conf. Robotics and Automation, St. Louis, 22-27.

[28] ASTM, 1998 Standard test method for particle-size analysis of soils ASTM D422-63, ASTM Standards, Philadelphia, Pennsylvania.

3D ODZIV IZKOPA VAROVANEGA Z NAGNJENIMI OPORNIKI V BLIŽINI ZGRADB

Zahra Sabzi *(vodilni avtor)*
Karaj branch, Islamic Azad University,
Department of Engineering
Karaj, Iran
E-pošta: zahra.sabzi@kiau.ac.ir

Ali Fakher
University of Tehran,
Faculty of Engineering
Teheran, Iran
E-pošta: afakher@ut.ac.ir

Ključne besede

izkop, nagnjen opornik, sosednja zgradba, terenska meritev, 3D analiza s končnimi elementi, projektiranje na osnovi pomikov

Izvleček

Predstavljena študija se osredotoča na terenska opazovanja in 3D numerične analize izkopa, varovanega z nagnjenimi razporami v bližini zgradb. Raziskan je učinek opornikov na prenašanje obtežb in zmanjšanje upogibov. Oporniki zmanjšujejo vrednosti deformacij in ustvarijo tudi kotni učinek podoben kot v vogalu diafragm. Raziskovan je vpliv razdalje med oporniki in predlagan optimalni razmik med oporniki. Predlagana je najbolj učinkovita konfiguracija vgradnje opornikov za zmanjševanje deformacij in poškodb zgradbe. Na podlagi rezultatov numeričnih študij so predstavljene smernice za projektiranje na osnovi pomikov.

3D RESPONSE OF AN EXCAVATION ADJACENT TO BUILDINGS SUPPORTED BY INCLINED STRUTS

Zahra Sabzi *(corresponding author)*
Karaj branch, Islamic Azad University,
Department of Civil Engineering
Karaj, Iran
E-mail: zahra.sabzi@kiau.ac.ir

Ali Fakher
University of Tehran,
Faculty of Engineering
Teheran, Iran
E-mail: afakher@ut.ac.ir

Keywords

excavation, inclined strut, adjacent building, field measurement, 3D finite-element analysis, displacement-based design

Abstract

The presented study focuses on field observations and a 3D numerical analysis of open-cut excavations adjacent to a building supported by inclined struts. The performance of the struts in carrying the building loads and decreasing the deflections is investigated. Struts reduce the amount of deformations and also create a corner effect similar to the diaphragm walls corner. The influence of the distance between the struts is studied and the optimum struts interval is proposed. The most effective configuration of struts installation in reducing the deflections and building damage is proposed. A displacement-based design guideline is also presented based on the results of numerical studies.

1 INTRODUCTION

A simple method for protecting the buildings adjacent to open-cut excavations is the use of inclined struts connected to the buildings. This method is considered as a traditional support method in Iran and is the most common method in small-sized excavations [1]. Fig.1 schematically illustrates the use of struts and the current state-of-the-practice for this method. In the presented method, which is appropriate for a small to medium depth of excavations, the struts are directly connected to the buildings and control the movements of the buildings and consequently reduce the soil movements. The method is the subject of this paper and should not be mistaken for the use of struts that are connected to the retaining walls. Some studies were conducted and the primary understanding of the performance of inclined struts was presented [2], [3]. The performance mechanisms of such a strut were proposed as follows: (i) the load of the adjacent building is partially passed to the bottom of the excavation through the strut and consequently less pressure is exerted on the soil beneath the foundation; therefore, the settlement of the foundation decreases. (ii) The strut reduces the horizontal displacements of the buildings due to the lateral constraints it creates. Consequently, it can reduce the horizontal deflections of the excavation unsupported face. The deformation pattern of the excavation face and the ground surface settlement were strongly affected by the use of inclined struts that are connected to the building. Previous studies on this method showed that the use of inclined struts that are connected to the adjacent buildings influences the deformation patterns; the shape of the horizontal deflection at the excavation face is changed from cantilever type to lateral-bulging type; the ground surface settlement profile is changed from spandrel-type to concave-type [3].

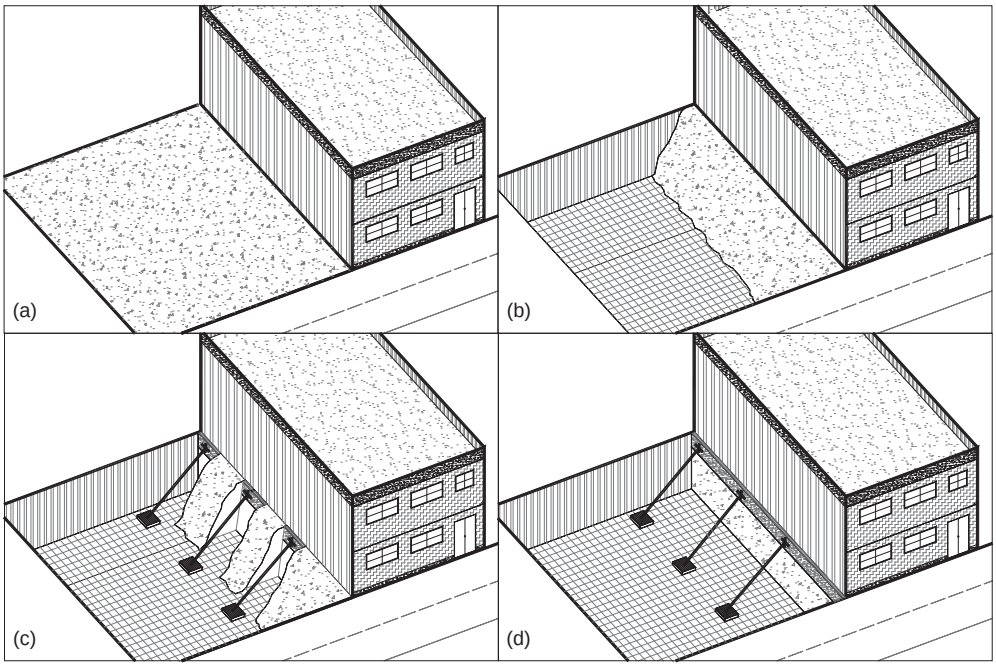

Figure 1. Schematic of the current state-of-the-practice of excavation using inclined struts connected to an adjacent building (a) before excavation; (b) excavation stage 1; (c) installation of struts, stage 2; (d) excavation stage 3.

One of the objectives of this paper is to verify the proposed mechanisms of struts through 3D numerical analyses and a comparison of field measurements and numerical studies.

Fig. 2 shows the most conventional configurations for excavation. Sadeghian and Fakher presented the most effective configuration for strut installation that produces the least ground surface settlement and horizontal deflection [2].

In this pattern the struts install after the first stage of excavation by sloping the sides of the excavation and then excavating the marginal soil behind the struts (Fig.2 (e)). This configuration minimizes the damage to the buildings, according to the criteria proposed by [4].

Sadeghian and Fakher obtained optimum results for inclined strut installation by connecting the struts to the

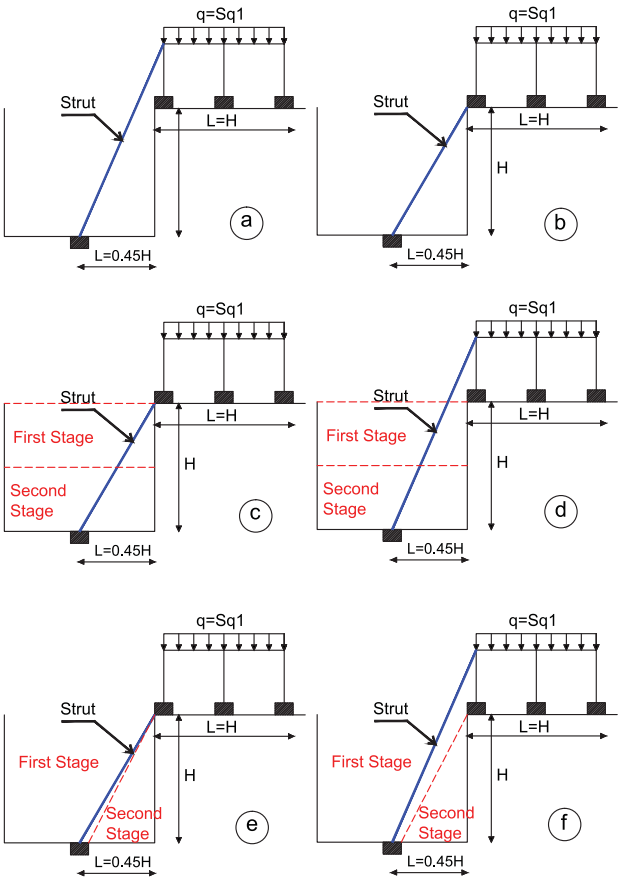

Figure 2. Most common configurations of the excavation procedure using inclined struts. (a) Struts connected to the first floor after full excavation. (b) Struts connected to the foundation after full excavation. (c) Struts connected to the foundation after full excavation made in two stages. (d) Struts connected to the first floor after full excavation, made in two stages. (e) Struts connected to the foundation after the first stage of excavation. (f) Struts connected to the first floor after the first stage of excavation [2].

foundation of the adjacent building [2]. Fig. 2 illustrates the most effective inclination angle for the struts at L/H = 0.45, where L is the distance of the struts from the excavation face at the bottom and H is the excavation depth. This value corresponds to an inclination angle of 65° above the horizontal.

Failure to control the deformations can cause significant damage to adjacent structures. Consequences such as the loss of bearing capacity of the foundations of adjacent building and the loss of a factor of safety for basal heave, global instability or bearing capacity can become very hazardous. In the presented paper, it is assumed that the safety factor of excavation is in an acceptable range that is derived from an appropriate limit equilibrium analyses or design codes (e.g., The National Building Regulations of Iran suggest safety factors for basal heave, global instability or bearing capacity for different conditions and depths of excavations). Thus, the presented analyses are focused on the displacements induced by the excavation and on the assessment of the admissibility of these displacements with respect to the maximum acceptable values.

Although the mentioned method has many practical applications, the inclined struts' behavior is not fully understood and determinations of the design parameters like loads and the distance between the struts are uncertain. Most designs are based on past experiences and no definitive conclusions exist regarding the effect of the struts on the deformations.

Two-dimensional plane-strain finite-element analyses of the strutted excavation have been performed by many researchers [5], [6], [7], [8],[9], [10]. But excavations behave as a three- dimensional problem [11]. Many studies have been performed to investigate the three-dimensional performance of excavations [12], [13], [14], [11], [15], [16], [17]. The mentioned method of excavation using inclined struts has been previously analyzed using 2D finite-element modeling [1], [2], [3], [18], but some important aspects can be simulated only when a 3D model is employed. Among them: (i) the behavior of the excavation corners, (ii) the sequence of struts installation and (iii) the struts interval can be mentioned. In this study, a series of parametric studies using a 3D numerical model were performed to examine the struts' performance.

2 NUMERICAL ANALYSIS

In the presented research, three-dimensional analyses were performed to account for the complex 3D nature of the excavation and to examine the inclined struts in the excavation. Numerical simulations were carried out using the FEM program ABAQUS [19]. Fig. 3 shows the finite-element mesh. The soil was modeled using three-dimensional brick elements with eight nodes. A large zone was selected to avoid any measurable effects from the boundaries. It was assumed that the vertical boundary is free in the vertical direction and restricted in the horizontal direction; and the bottom horizontal boundary was restricted in both the horizontal and vertical directions. To minimize the boundary effects, the vertical boundary and the bottom horizontal boundary at the far ends were set to almost 5 times the excavation's width and depth, from the center of the excavation.

The element size is chosen based on the desire to increase the accuracy of the results and reducing the computational effort. A large number of iterations were carried out to achieve the convergence criteria and the accuracy of the deflections. In a finite-element simulation of excavations it has been demonstrated that the refinement of the mesh had no significant effect on the final displacements [20]

In this study the horizontal dimensions were set to be of the same order as the vertical dimension and to be compatible with the dimensions of the excavated area. In order to reduce the required computational effort, the element dimensions could increase as the distance from the excavated area increases.

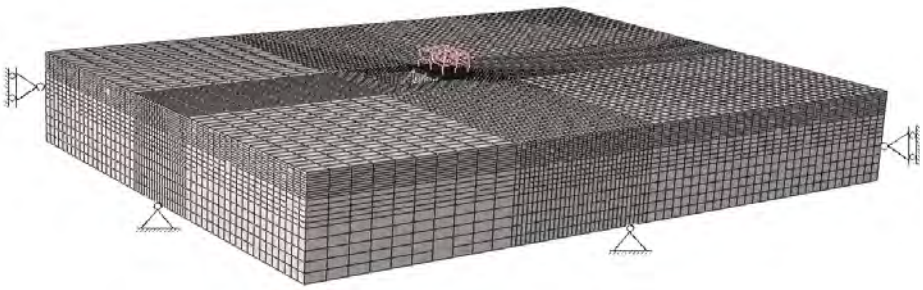

Figure 3. Finite-element mesh used in the analysis.

Many soil models in the literature can represent the excavation, but as the objective of the presented paper is to study the effect of struts, a simple model may be more illustrative than a complex one. In this study, the nonlinear elasto-plastic behavior of soils is simulated using the hyperbolic model [21]. The hyperbolic model is implemented with a user-defined model within the subroutine UMAT in the ABAQUS program and then used in the analyses. Although the hyperbolic model is not formulated based on the theory of plasticity, it considers the deformation characteristics of soils such as the nonlinear, inelastic, and strain-dependent ones. The hyperbolic model has been used in analyzing excavation problems [12], [14], [22], [23], [24], [25] possibly due to the fact that this type of soil model is relatively simple, conceptually understood, and easy for determining the soil parameters [12].

For the hyperbolic model, seven parameters are required to fully describe the stress–strain behavior of the soil. These are cohesion (c), friction angle (ϕ), stiffness modulus number for primary loading (E), stiffness modulus exponent (m), stiffness modulus number for unloading–reloading (E_{ur}), failure ratio (R_f), and Poisson's ratio (v).

3 VALIDATION OF THE NUMERICAL MODEL

The built numerical model in the current study was validated using data obtained from a field measurement undertaken by the authors. Then extensive parametric studies were performed to evaluate the trend of excavation behavior with respect to the variation of parameters.

3.1 Project description

Three boreholes were drilled in order to investigate the soil properties required for modeling the excavation. The soil at the excavation site typically consisted of marl that contains variable amounts of clays and silts and was plastic and sticky. Fig. 4 shows the stratigraphy of the site's soil. As shown in Fig.4 the subsurface conditions at the site consisted of two layers. The first layer was about 8m-thick stiff clayey silt; and this layer mainly affected the excavation behavior. The second layer was about 10m-thick stiff silty clay. No groundwater table was detected in the excavation zone; this means that pore water pressure had no effect on the behavior of the excavation. Fig.4 also shows variations of standard penetration test number (N_{SPT}) and the strength parameters of the soil. The shear-strength parameters were obtained from triaxial tests. The unit weight of the soil layers are also given in Fig.4.

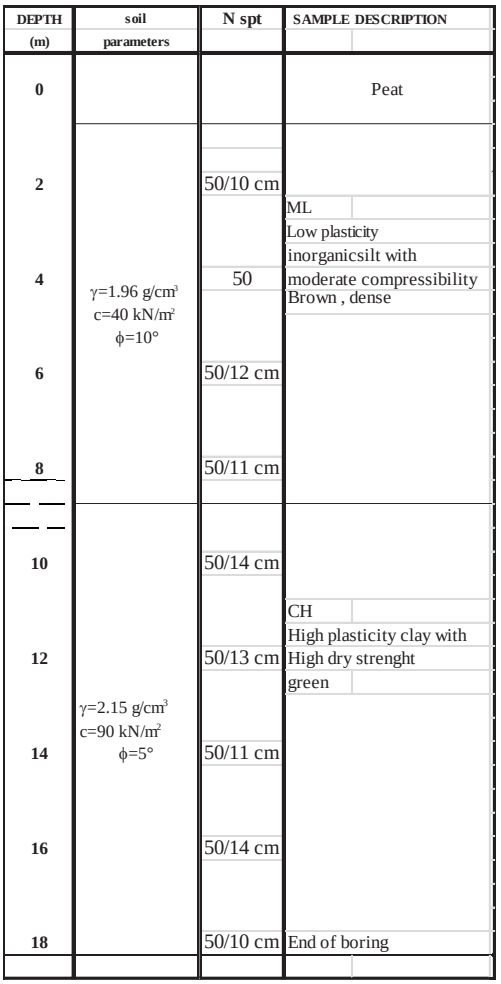

Figure 4. Stratigraphy of the excavation case.

A plan view of the dimensions of the excavation, support system geometry, neighboring structures and the instrumentations are shown in Fig. 5. As shown in this figure, the shape of the excavation site was 10×16 m^2. The final excavation depth was 4.5m, and this was completed using the described method, which is illustrated in Fig.1. The inclination of the struts was about 45° due to the site condition and the working space. The foundation of the neighboring building was mat footing. To monitor the displacements, optical survey points on the excavation face and buildings were used. Electrical strain gauges and a mechanical load cell, which was designed and fabricated by the authors, were used to measure the strut loads. The excavation procedure and strut-installation sequences are given in Table 1.

The dimensions of the structural elements in a building and the struts in numerical model were the same as for the excavation case. The neighboring building on the north side of the excavation was a three-story

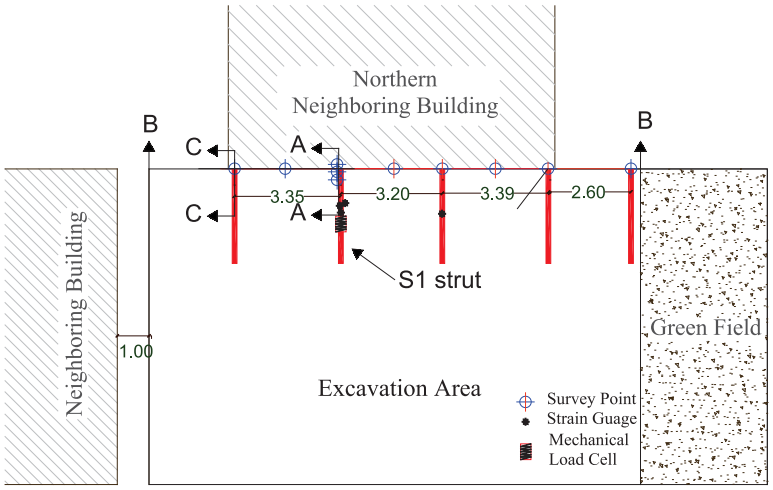

Figure 5. Plan view of excavation and instrumentation scheme.

Table 1. Excavation phases of the project.

Excavation stages	Description
1	Excavate down to 4.5 m below the ground surface by sloping the sides of excavation as shown in Fig.1 (b).
2	Construction of the foundation of the struts and installation of the struts, Fig.1 (c).
3	Excavation of marginal soil behind the struts, Fig.1 (d).

structure and was modeled as a steel frame by using beam elements as linear elastic materials with no failure criterion and the Young's modulus of steel was set $E_{steel} = 2.0\times10^5$ MPa. The inclined struts, that were connected to the adjacent building foundation, were steel box 140×140×7mm^3 and were modeled using three-dimensional beam elements and were simulated as linear elastic materials with no failure criterion and the Young's modulus is set to $E_{steel} = 2.0\times10^5$ MPa. The concrete foundations of the struts were 500 ×500 mm^2 bearing pads with a 400 mm thickness, which were placed below the ground level of excavation, but were modeled as a single mat foundation due to the negligible effect on results. The foundation of the building and the foundation of the struts were modeled as concrete foundations using solid elements as linear elastic material with no failure criterion and the Young's modulus of concrete was set $E_{concrete} = 2.0\times10^4$ MPa. The interface between the structure and the soil elements was modeled using contact elements.

The geotechnical characteristics of soil are presented in Table 2. The strength parameters c and ϕ were obtained directly from Drained and Consolidated (CD) triaxial laboratory tests. The value of the Young's modulus of first layer at a depth of 2 m of soil was directly obtained from the plate load-test results and provides a primary understanding of the soil stiffness. Table 3 lists the parameters of the geometry of the excavation used in the numerical analyses. The struts spacing are as shown in Fig.5.

In this study the soil stiffness modulus parameters (K, K_{ur}) are estimated from the plate load-test results and verified by the stiffness of soil of a nearby similar excavation project. The failure ratio, R_f, is normally in the range 0.5 and 1.0 [26]. In this study, R_f is assumed to be 0.9 for cohesive soil, accounting for the flexible behavior of clay [26]. The stiffness modulus exponent, m, can reasonably be assumed to be 0.5 for the cohesionless soil [27] and m should be equal to 0.0 for cohesive soil due to the concept of effective stress [27]. Poisson's ratio is assumed to be 0.3 at the pre-failure condition and 0.49 at or near the failure condition. The lateral earth pressure at rest, K_0, is obtained from Jaky's equation.

Table 2. Parameters of the soil used in numerical modeling.

Parameter	K	K_{ur}	m	c (kPa)	$\phi°$	γ(kN/m^3)	R_f	$v_{prefailure}$	$v_{failure}$	K_0
Layer 1	1900	4300	0.3	40	10	19.6	0.9	0.3	0.49	0.82
Layer 2	2550	5500	0.1	90	5	21.5	0.9	0.3	0.49	0.91

Note:K, K_{ur}, c, ϕ, m, R_f, v : the hyperbolic model parameters; K_0= "at-rest" coefficient of lateral earth pressure.

Table 3. Parameters of the excavation project used in the numerical modeling.

Parameter	H (m)	B (m)	L (m)
Amount	4.5	10	16

Note: H= excavation depth, B= excavation width and L= excavation length.

3.2 Excavation-induced displacements and loads

Figs. 6, 7 and 8 show the observed deflections at excavation stages and show the comparison of the deflections between the field observations along the north side of the excavation and the FE model predictions.

By comparing the results for excavation with and without struts, the effectiveness of the struts can be evaluated. Fig.6 shows that the computed horizontal deflections of the excavation face at section A-A (Fig.5), for three stages are much smaller than those without struts. It can be seen that the maximum horizontal deflection at the analysis is reduced by 50%, by the installation of strut. Also, it can be seen from Fig.6 that the use of struts connected to the adjacent building

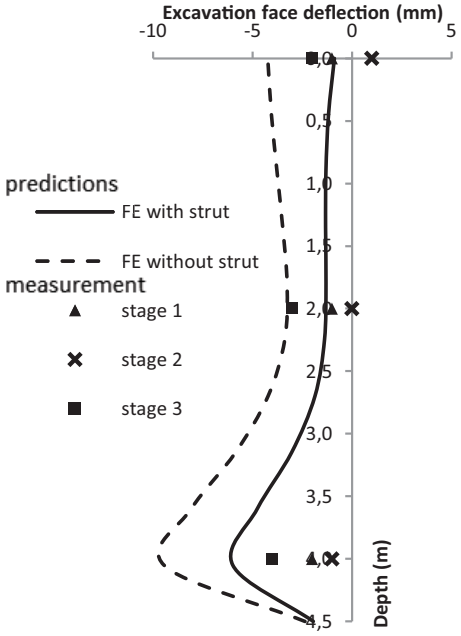

Figure 6. Comparison of the measured horizontal deflections and finite-element (FE) analyzed values for the excavation face at section A-A, shown in Fig.5.

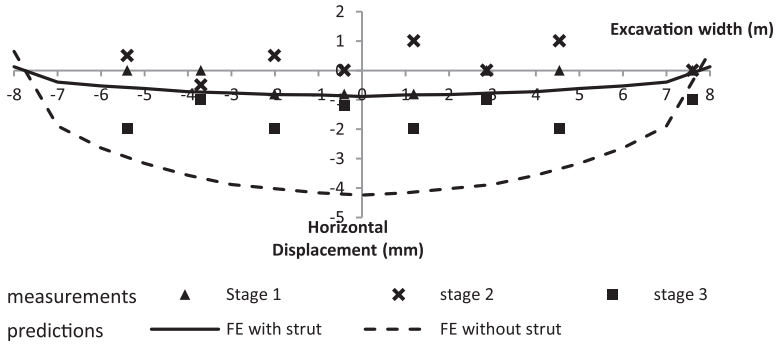

Figure 7. Comparison of the measured horizontal deflections and finite-element (FE) analyzed values along the north side of the excavation; section B-B shown in Fig.5.

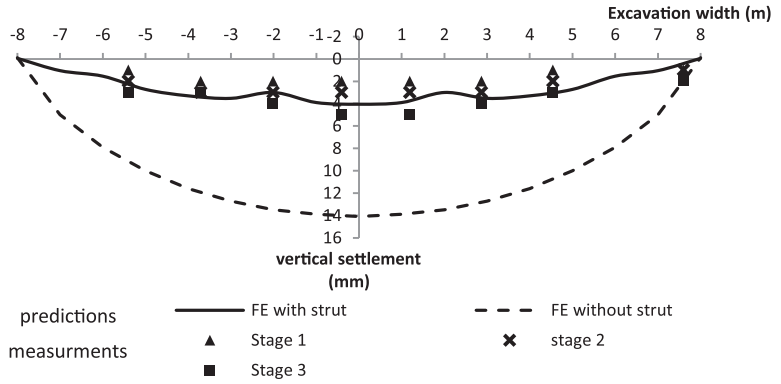

Figure 8. Comparison of the observed vertical settlements and finite-element (FE) analyzed values along the north side of the excavation; section B-B shown in Fig.5.

decreased the horizontal deformation to a slight value near the excavation surface around the contact point of the strut and lowered the location of the maximum horizontal deformation near the excavation bottom, whereas without using the struts, a large horizontal deformation will occur near the excavation surface.

Similarly, Figs.7 and 8 show that the computed horizontal deflections and surface settlements of the foundations along the north side (i.e., section B-B in Fig.5) for three stages are much smaller than those without struts. The maximum horizontal deflection and the vertical settlement beneath the foundation along the north side are reduced by about 80% and 70% respectively due to the installation of struts. Therefore, the installation of struts can substantially reduce the lateral deflections and vertical settlements.

Moreover in Figs.7 and 8, it is clear that there is a larger zone of relatively constant horizontal deflection and vertical settlements at the end of stage 1 than at the end of stage 3. This means that before the installation of strut, the plane strain condition exists over a larger portion of the excavation length than after the installation of a strut, where a shallower section has relatively constant values; and the 3D effects of the excavation become more apparent as the struts are installed.

Figures show that the computed deflections for the excavation with the strut are reasonably consistent with those observed in field measurements. Therefore, it is found that the above-mentioned numerical model is able to predict the deflections of the excavations.

As stated in the introduction of the presented paper, the performance mechanism of the struts derived from the field measurements and the 2D numerical analysis. It is needed to quantify in detail the 3D performance of the struts in excavations to provide a reasonable method to design the struts.

The ground surface settlement profile and the horizontal deflection of the excavation face illustrate the restraining effect of the struts on soil movement. The results of the numerical analysis make it clear that the struts decrease the horizontal displacements of the excavation face. The vertical settlement is also reduced by the installation of struts. These results confirm the mechanisms (i) and (ii). Moreover, it can be seen from Figs. 7, 8 that the maximum horizontal deflection and vertical settlement occur at the approximate middle position of the excavation length. Also, as shown from field observations in Figs.7 and 8, the horizontal deflection and vertical settlement are smaller at the section where struts are installed than those sections at a distance from the struts.

Fig. 9 illustrates the lateral deflection of the excavation face derived from numerical analyses at different positions of the excavation length (Fig.5.) The maximum horizontal movements occur near the bottom of the excavation at the center of the excavation length and much smaller lateral movements occur at the corners. It can be seen that the 3D effects become more apparent as the excavation depth increases, confirming that the effects of the corners of the excavation become more apparent as the horizontal deflection increases.

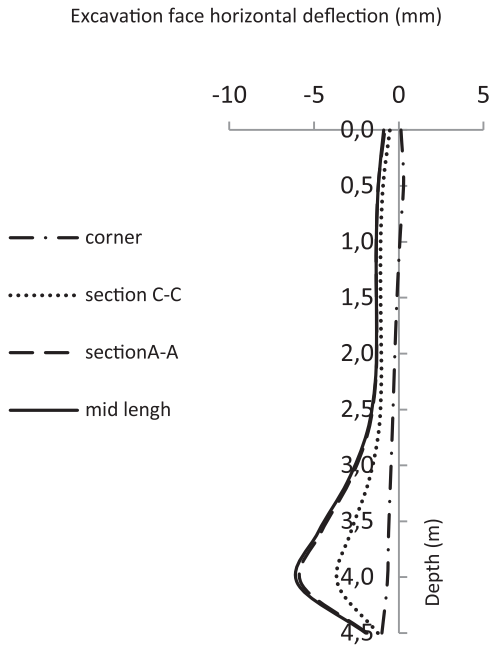

Figure 9. Comparison of the lateral movements of different positions of the excavation length (as shown in Fig.5).

4 INVESTIGATION OF THE 3D BEHAVIOR OF EXCAVATION

In this section the effects of important parameters are studied using the above-mentioned 3D finite-element model. A large number of finite-element analyses are made to evaluate the influence of the geometry of excavation and the parameters of the struts on the deformations. The results of the parametric studies are summarized herein.

4.1 3D effect of struts

In this section the values for H, B, L and the strut spacing were changed, as shown in Table 4, to investigate the effects of the various parameters in the parametric studies. Fig. 10 shows a cut of the 3D model in detail, to obtain a better understanding of the results.

Table 4. Parameters used in the parametric studies.

Parameter	H (m)	B (m)	L (m)	d (m)
Amount	4.5	32	32	8

Note: H= excavation depth, B= excavation width and L= excavation length and d=Struts spacing.

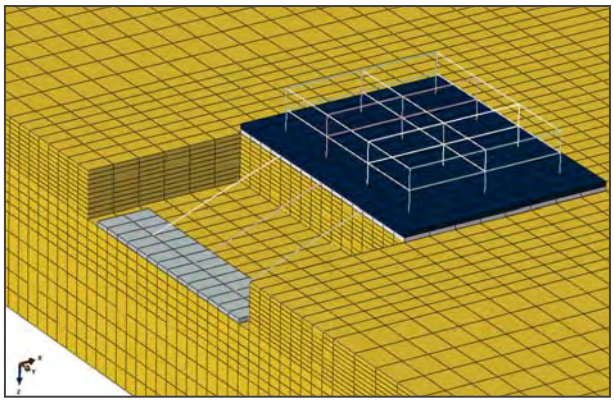

Figure 10. The cut of the 3D model with details.

Fig.11 compares the distribution of the lateral stresses in the soil in the analyses with and without the installation of struts. The direction of the lateral stress is shown in Figs. 11. The positive values represent the tensile stresses. The results show that the distribution of lateral stresses is considerably changed in the ground surface adjacent to the excavation and in the excavation face by the installation of struts. Also, it can be seen that the lateral stress generally decreases near the struts. This is probably due to the arching effect of the struts. It is clear that the arch formation is noticeable in the vicinity of the corner struts. According to many studies [5], [11], [13], [14], [15], [16] due to the arching effect, the horizontal deflection and the vertical settlement near the corners are very small. The parametric analyses and the field-observation results imply that the installation of struts has a similar effect as the diaphragm wall corners.

The contour of plastic strains is depicted in Fig. 12. The evolution of the plastic strains in all of parametric studies shows that the plastic zone begins to form near the bottom of excavation face at the middle of the excavation length.

(a)

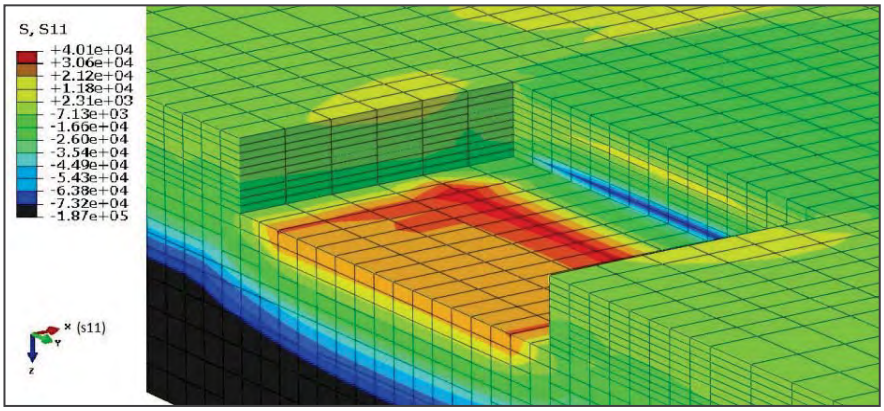

(b)

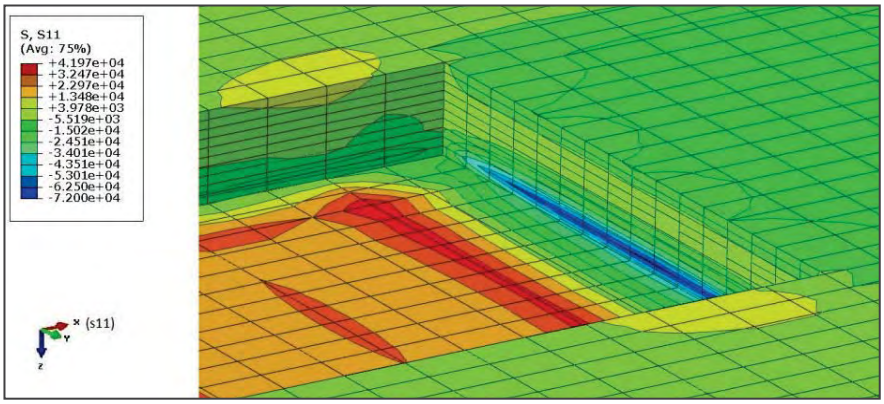

Figure 11. Contours of the soil lateral stresses (a) without struts, (b) with installation of struts.

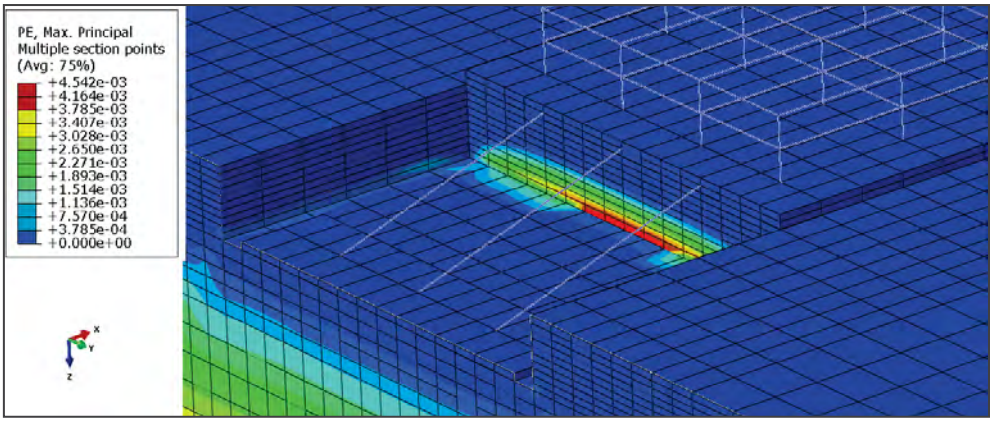

Figure 12. Contours of the soil plastic strains at the final stage of excavation.

4.2 Strut intervals

In order to investigate the effect of the strut intervals at different depths of the excavations and to obtain comparable results in the parametric studies, as mentioned previously, the lengths of the excavations are increased to 32 m in the analyses. The influence of the distance between the struts on the maximum lateral deflections is shown in Fig. 13, where the maximum lateral deformations (δ_{hmax}) are normalized with respect to the depth of the excavation (H). It should be noted that the values at d=0 m are obtained from a two-dimensional analysis. Fig. 13 shows how δ_{hmax}/H increases as the distance between the struts (d) increases, with the influence of the support spacing being more pronounced in the deeper excavation than in the shallower excavation. Fig.13 also shows that when the distance between the struts exceeds the excavation depth, e.g., d/H > 1.0, the δ_{hmax}/H remained approximately constant for a specific excavation depth. These results imply that if the distance between the struts exceeds the excavation depth, the inclined struts would have a minor restraining effect on the horizontal deflections. Consequently, it can be concluded that the maximum distance between the struts should be limited to the excavation depth.

Fig.14 shows the influence of the distance between the struts on δ_{htop}/H and δ_{vtop}/H, of which δ_{htop} and δ_{vtop} are the horizontal and vertical deflections at the top of the ,excavation respectively, and they are obtained from the values of horizontal and vertical deflections near the connection point of the struts to the building. The results show that δ_{htop}/H and δ_{vtop}/H increase with the increasing distance between the struts and the values of δ_{htop}/H and δ_{vtop}/H are seriously affected by the distance between the struts. The above observations can be explained by the fact that the top of the excavation near the connection point of the struts to the building is directly restrained from movement by the struts, and the inclined struts have a serious restraining effect near the excavation surface and also on the adjacent building.

The spacing of the struts can affect their bearing load. To investigate the effect of the interval of the struts on the strut loads, variations of the maximum computed strut load for four excavation depths are shown in Fig.15. The figure shows that the strut load values increase approximately linearly with an increasing distance between the struts for a specific depth. Also, it can be seen from Fig.15 with increasing excavation depth, the strut load increases dramatically.

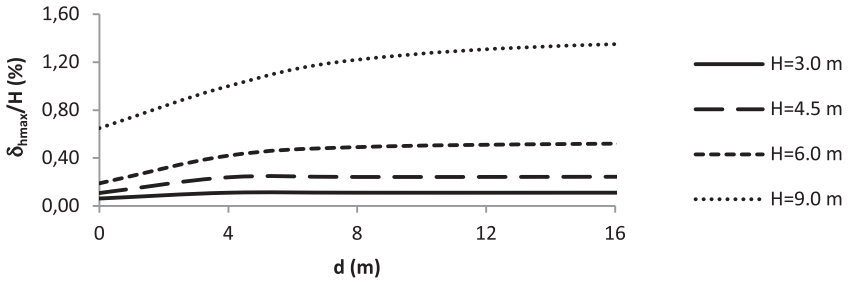

Figure 13. Relationship between the maximum horizontal deflection and the strut intervals for different excavation depths.

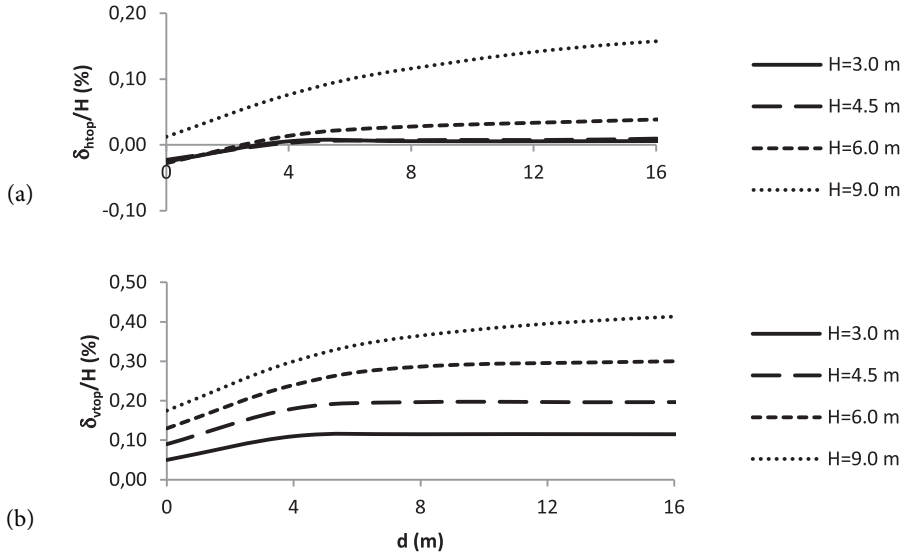

Figure 14. Relationship between the deflections at the point of connection of struts to the building and the strut intervals for different excavation depths, (a) horizontal deflection, (b) vertical deflection.

For an assessment of the effect of the strut intervals on the performance of the struts, the parameter load bearing ratio (LBR) is defined in this study. This parameter is obtained by dividing the unit load of the strut on the unit load of adjacent structures, as shown in Eq.1:

$$LBR = \frac{q_{strut}}{q_{build}} \quad ; \quad q_{strut} = \frac{F_{strut}}{H \cdot d} \qquad (1)$$

where F_{strut} is the strut load, d is the distance between the struts, H is the excavation depth and q_{build} is the unit

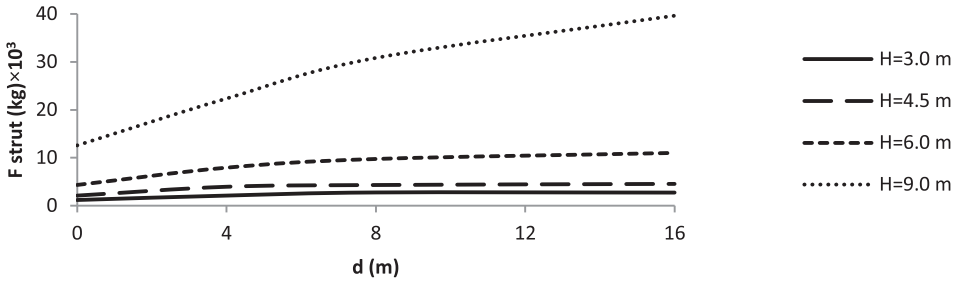

Figure 15. Relationship between the maximum struts load and the strut intervals for different excavation depths.

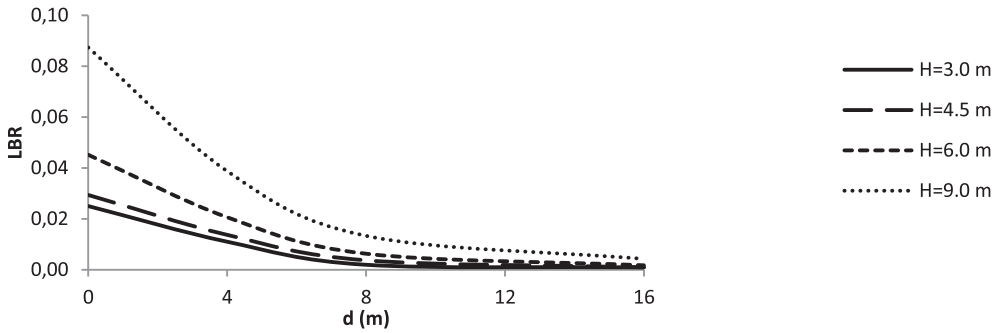

Figure 16. Relationship between the load bearing ratio (LBR) and the strut intervals for different excavation depths.

load of the adjacent building. It assumes that a surcharge of 1 ton/m^2 for each floor of the neighboring buildings act on the ground surface. A greater LBR value implies that the struts have more effect in the bearing building load and vice versa. To consider the effect of the interval of the struts on the LBR, variations of the LBR computed with the maximum strut load for four excavation depths are shown in Fig.16. The results show that LBR decreases rapidly with an increasing distance between the struts for a specific depth. The decrease in LBR is approximately proportional to the square of the struts' interval.

These results indicate that with an increasing distance between the struts, although the struts' loads increase while the load bearing ratio of strut decreases, the performance of the struts in carrying the buildings' loads reduces.

4.3 Strut-installation pattern

As mentioned in the introduction, Sadeghian and Fakher [2] used a numerical analysis to investigate the effect of the strut-installation pattern in two-dimensional excavations. In this paper the efficient sequences of strut installation in 3D excavations are studied. The most effective method in the installation pattern of struts, Fig.2 (e), is selected based on the Sadeghian and Fakher studies [2] and extended in 3D analyses with four different patterns. In all of these patterns, the first stage is the same and is consistent with the method that is illustrated in Fig.1.

(i) Configuration 1: The excavation is executed in one stage, as shown in Fig.1(b); afterwards all of the struts are installed simultaneously, as shown in Fig.1(c) and finally the marginal soil is excavated, as illustrated in Fig.1(d).
(ii) Configuration 2: First the site's excavation zone is fully excavated (Fig.1(b) and Fig.1(d)) and all of the struts are then installed.
(iii) Configuration 3: First corner struts are installed and the marginal soil behind the struts is excavated and then the middle struts are installed and the remaining soil is excavated.
(iv) Configuration 4: Middle struts are installed and the marginal soil in the struts back is excavated. Then the corner struts are installed and the remaining soil is excavated.

To find the most effective configuration, horizontal deflections are considered. Fig.17 compares the excavation-induced maximum horizontal deflection along the excavation length for the four mentioned excavation procedures. It should be noted that the results in Fig.17 are obtained from the numerical model with the parameters as given in Table.4. According to Fig.17 the maximum horizontal displacement in the center of the excavation length induced by configuration 2 is larger than the other configuration and the most effective configuration is configuration 1. In configuration 4, since the middle struts are installed earlier than the corner struts, the horizontal deflection at the middle of the excavation length is restrained rather than the other configurations. Obviously, the most efficient method of installation for the strut is the installation of all the struts simultaneously. But if it is not possible to execute all of struts installation in one step, the installation of the middle struts at first and then the installation of the corner struts produces fewer horizontal deflections at the middle of the excavation length.

5 DISPLACEMENT-BASED DESIGN

Limiting the movements of adjacent buildings is becoming a significant design issue because deformations can cause significant damage to the structures. Increasingly, designs are controlled by the need to limit movements,

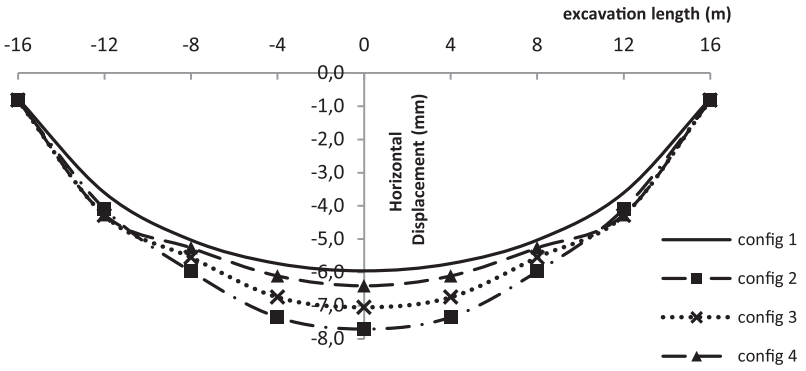

Figure 17. Comparison of the maximum horizontal deflection along the excavation length for four strut installation configurations.

which goes beyond the traditional design approach of focusing on the required support loads and avoiding collapse. These conditions require a new approach to designing support systems to focus on controlling displacements [28]. In the displacement-based design, a comprehensive understanding of the characteristics of deformations is very important. Using a displacement-based design approach requires a way to predict displacements. The proposed approach determines the displacement based on numerical studies and compares the results with the allowable displacement.

5.1 Allowable deflections

There are several publications on the allowable deflections for different types of structures and some criteria have been proposed for estimating the potential of damage to adjacent buildings. Boscardin and Cording [4] developed a plot relating the angular distortion and horizontal strain to building damage. The establishing permissible deflections range depends on the project conditions. The maximum allowable angular distortion and the horizontal strain should be determined according to the level of damage and the type and condition of the building. The values for the maximum allowable horizontal (δ_h) and vertical (δ_v) deflections can then be obtained.

5.2 Simple estimation of deflections

The deformations are the result of many complex factors such as ground condition, type of retaining structure, stiffness of supports and adjacent building conditions. The deflections determination can be obtained from a dimensional analysis of the parameters that appeared to contribute to the deflections in an excavation. The parameters that have the most effect on the deflections are as follows:

$$\delta_h = f(E_s, E_b, H, \gamma_s, c, n, K_{st}) \qquad (2)$$

$$\delta_v = f(E_s, E_b, H, \gamma_s, c, n, K_{st}) \qquad (3)$$

where δ_h and δ_v are the horizontal and vertical deflections, respectively, and E_s = Young's modulus of the soil; E_b = Young's modulus of the structure; H = excavation depth; γ_s = unit weight of the soil; c = cohesion of the soil; n is the number of the story of building; and K_{st} is the stiffness of the strut and is obtained by:

$$K_{st} = \frac{A_{st} E_{st}}{ld} \qquad (4)$$

where A_{st} = cross-sectional area of strut; E_{st} = modulus of elasticity of strut; l = length of strut; and d = distance between struts.

A dimensional analysis suggests that a dimensionally homogeneous equation can be reduced to a relationship among a complete set of dimensionless products. The correct use of the dimensionless products makes the parametric studies more efficient by revealing which variables are truly independent [29]. From an inspection of the variables contributing to deflections, it can be seen that three dimensionless groupings emerge. One grouping is the relative stiffness resistance, $E_b \cdot E_{st} / E_s \cdot K_{st}$, which captures the soil-structure-strut interaction [30]. Another grouping is the excavation stability number, $H\gamma_s / c$, which characterizes the effects of the soil conditions. The third dimensionless parameter is the number of the story of the building (n). The two first-mentioned dimensionless groupings are combined and produce the dimensionless parameter R as:

$$R = \left(\frac{E_b}{E_s} \cdot \frac{E_{st}}{K_{st}}\right) \times \frac{H\gamma_s}{c} \quad \text{or} \quad R = \left(\frac{E_b}{E_s} \cdot \frac{ld}{A_{st}}\right) \times \frac{H\gamma_s}{c} \qquad (5)$$

Thus Equations 2 and 3 can be rewritten as:

$$\delta_h = f(R,n) \qquad (6)$$

$$\delta_v = f(R,n) \qquad (7)$$

It should be noted that all the variables included in the dimensionless parameters are from basic soil, geometry parameters of excavation and adjacent building that the designer can easily determine from standard soil tests and excavation and building specifications; and also the struts' cross-sectional area and materials as design parameters can be estimated primarily based on similar excavation projects.

Fig.18 shows the dimensionless parameter (R,n) values and the maximum deflections obtained from the parametric finite-element studies and the fitted curves.

The trend curves fitted through the parametric data have the form:

$$\frac{\delta_{htop}}{H}(\%) = 0.42e^{0.5n} \times \left[\left(1.54\times10^{-20} \times R^2\right) + \left(1.7\times10^{-11} \times R\right) + \left(5.1\times10^{-3}\right)\right] \qquad (8)$$

$$\frac{\delta_{vtop}}{H}(\%) = 1.01e^{0.5n} \times \left[\left(2.9\times10^{-20} \times R^2\right) + \left(1.65\times10^{-10} \times R\right) + \left(0.13\right)\right] \qquad (9)$$

$$\frac{\delta_{h\max}}{H}(\%) = 0.93e^{0.1n} \times \left[\left(1.51\times10^{-19} \times R^2\right) + \left(1.68\times10^{-10} \times R\right) + \left(0.19\right)\right] \qquad (10)$$

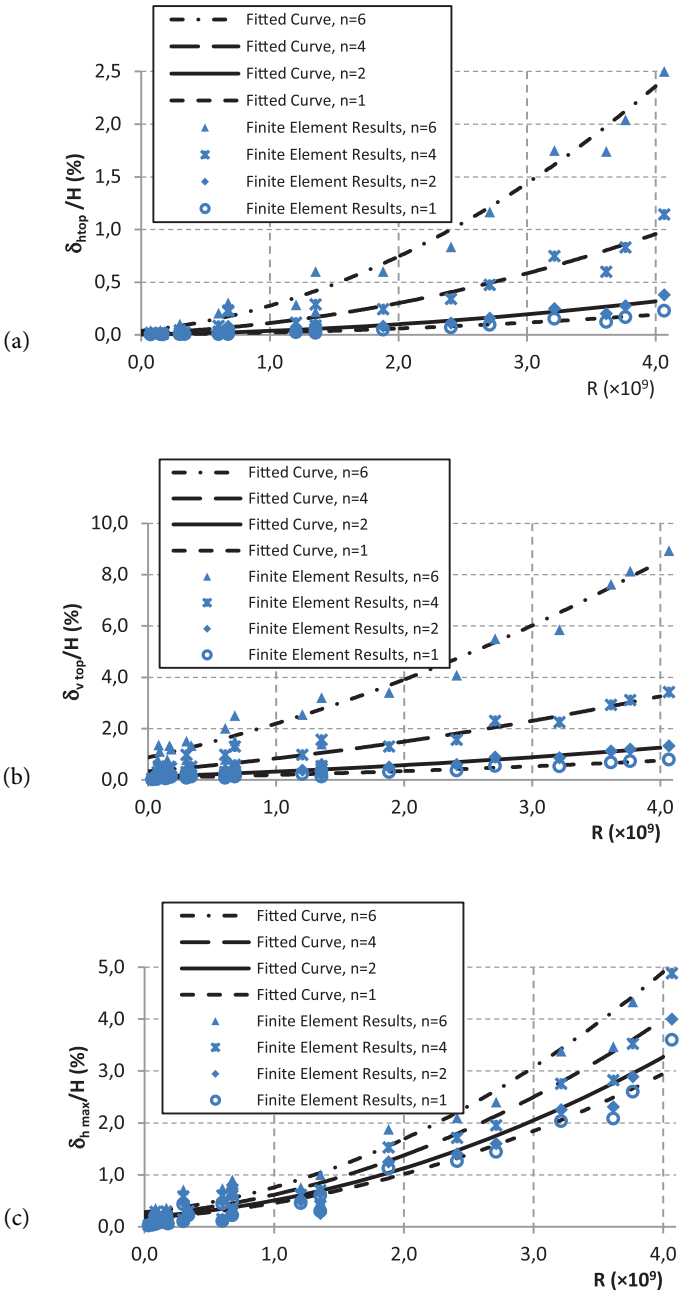

Figure 18. Comparison of the finite-element parametric studies with the proposed relations; (a) horizontal deflection at the top of the excavation, (b) vertical settlement at the top of the excavation, (c) maximum lateral deflection of the excavation face.

Eq.8 to 10 develop a design chart that allows the designer to choose the appropriate struts' cross-sectional area (A_{st}) and the distance between the struts (d) based on the design criteria of limiting the deformations. Conversely, for a given struts cross-sectional area and the distance between the struts, Eq.8 to 10 allow the designer to predict the horizontal and vertical deflections for excavations supported by inclined struts based on simple soil data and excavation geometry.

5.3 Proposed design guidelines

Based on the results of the current study, the following design guidelines are offered for estimating the design parameters.

1. Determine the soil and structure condition, including material properties (E_s, E_b, γ_s, c) and excavation and structure geometry (H, n).

2. Choose the cross-sectional area and the inclination angle of struts, based on the recommendations which are proposed in the introduction of paper; choose the distance between the struts based on the recommendations that are proposed in Section 4.2; calculate the struts stiffness (K_{st}).
3. Determine the values of allowable deflections as described in Section 5.1.
4. The maximum deflections can be obtained using all the input parameters from Eq. 8 to 10. The value of the deflections should then be compared with the allowable deflection to ensure that they are within acceptable limits. If the values of the deformations are not within permissible limits, the strut stiffness parameter should be adjusted to ensure that the deflections are within reasonable limits.

6 CONCLUSIONS

This study investigated the effect of struts on the deflections in excavations using a series of 3D finite-element parametric studies using strut spacing and the configuration of the strut installation as variables. The influence of the strut installation on the excavation was also studied. The results can be used to approximate the design of reasonable strut intervals and their cross-sectional areas. This study confirmed the proposed performance mechanism for inclined struts using field observations and 3D numerical analysis results. Finally a performance design approach was presented that can be used to effectively design inclined struts for an excavation based on the deformation limits. The following were observed:

1. The use of inclined struts connected to adjacent buildings decreased the amount of deformation and created a corner effect similar to that for diaphragm wall corners; the deflections at the corners were much smaller in response to the arching effect. The deflections were also smaller in the section where the struts were installed than in the sections that were some distance from the struts.
2. The use of inclined struts strongly decreased the horizontal deformation near the ground surface around the contact point of the strut and lowered the location of the maximum wall deformation to a point near the bottom of the excavation. Whereas, large horizontal deformations occurred near the surface of the excavation without the use of struts.
3. The stress distribution pattern outside the excavation zone at the ground surface revealed that the lateral stresses decreased near the struts in response to the arching effect of the struts; an arch formation was noticeable in the vicinity of the corner struts. The evolution of plastic strains in the excavations showed that a plastic zone began to form near the bottom of the excavation face in the middle of the excavation length.
4. Horizontal deflections increased as the strut intervals increased. It was found that the maximum spacing between the struts should not exceed the excavation depth.
5. The load bearing ratio (LBR) was defined and used to assess the effect of strut intervals on the performance of the struts. This parameter was obtained by dividing the unit load of a strut by the unit load of the adjacent structures. A larger LBR indicates that the struts play a major role in bearing the load from a building. The load on the struts increases as the distance between the struts increases, but the load bearing ratio (LBR) decreases and the role of the struts in carrying the building loads decreases. The decrease in LBR is approximately proportional to the square of the interval between the struts.
6. The most efficient strut-installation sequence in the length of the excavation that produces the greatest decrease in the horizontal deflection is the simultaneous installation of struts. If it is not possible to execute the installation of all the supports at the same time, the middle struts should be installed first and then the corner struts.

REFERENCES

[1] Fakher, A., Sadeghian, S, 2011. An investigation into Inclined Struts method as a type of shoring. Geotechnical Aspects of Underground Construction in Soft Ground, Rome, Italy, 369–375. DOI: 10.1201/b12748-48

[2] Sadeghian, S., Fakher, A. 2010. An investigation into a shoring method to support buildings adja¬cent to excavations. The 17th Southeast Asian Geotechnical Conference Proceeding, Taipei, Taiwan, May 10-13, pp. 207-210.

[3] Sabzi, Z., Fakher, A. 2015. The performance of buildings adjacent to excavation supported by inclined struts. International Journal of Civil Engineering 13, 1, 1-15.

[4] Boscardin, M.D., Cording, E.G. 1989. Building response to excavation-induced settlement. Journal of Geotechnical Engineering 115, 1, 1-21. DOI: 10.1061/(ASCE)0733-9410(1989)115:1(1)

[5] Lee, F.H., Yong, K.Y., Quan, K.C.N., Chee, K.T. 1998a. Effect of corners in strutted excavations: Field monitoring and case histories. J. Geotech. Geoenviron. Eng. 124, 4, 339–349. DOI: 10.1061/(ASCE)1090-0241(1998)124:4(339)

[6] Lee, F.H., Yong, K.Y., Lee, S.L., Toh, C.T. 1989b. Finite element modelling of strutted excavation.

Numerical models in geomechanics, Elsevier Applied Science, London, U.K., 577-584.
[7] Yong, K.Y., Lee, F.H., Parnploy, U., Lee, S.L. 1989. Elasto-plastic consolidation analysis for strutted excavation in clay. Computer and Geotechnics 8. 311-328. DOI: 10.1016/0266-352X(89)90038-4
[8] Finno, R.J., Harahap, I.S. 1991. Finite element analysis of HDR-4 excavation. Journal of Geotechnical and Geoenvironmental Engineering 117, 10, 1590–1609. DOI: 10.1061/(ASCE)GT.1943-5606.0001533
[9] Smith, I.M., Ho, D.K.H. 1992. Influence of construction technique on the performance of a braced excavation in marine clay. Int.J. Numer. and Analytical Methods in Geomech. 16, 845-867. DOI: 10.1002/nag.1610161202
[10] Coutts D.R, Wang J., Cai, J.G. 2001. Monitoring and analysis of results for two strutted deep excavations using vibrating wire strain gauges. Tunneling and Underground Space Technology 16, 2, 87-92. DOI: 10.1016/S0886-7798(01)00032-3
[11] Finno, R.J., Roboski, J.F. 2005. Three-dimensional responses of a tied-back excavation through clay. J. Geotech. Geoenviron. Eng. 131, 3, 273–282. DOI: 10.1061/(ASCE)1090-0241(2005)131:3(273)
[12] Ou, C.Y, Shiau, B.Y. 1998. Analysis of the corner effect on excavation behaviors. Can. Geotech. J. 35, 532-540.
[13] Ou, C.Y., Chiou, D.C., Wu, T.S. 1996. Three-dimensional finite element analysis of deep excavations. J. Geotech. Eng. 12, 5, 337–345.
[14] Ou, C.Y., Hsieh, P. G., Lin, Y.L. 2011. Performance of Excavations with Cross Walls. J. Geotech. Geoenviron. Eng. 137, 1, 94-104. DOI: 10.1061/(ASCE)GT.1943-5606.0000402
[15] Wu, C.H., Ou, C.Y., Tung, N. 2010. Corner effects in deep excavations establishment of a forecast model for taipei basin T2 zone. Journal of Marine Science and Technology 18, 1, 1-11.
[16] Blackburn, J.T., Finno, R.J. 2007. Three-dimensional responses observed in an internally braced excavation in soft clay. J. Geotech. Geoenviron. Eng. 133, 11, 1364–1373. DOI: 10.1061/(ASCE)1090-0241(2007)133:11(1364)
[17] Finno, R.J., Blackburn, J.T., Roboski, J.F. 2007. Three-dimensional effects for supported excavations in clay. J. Geotech. Geoenviron. Eng. 133, 1, 30–36. DOI: 10.1061/(ASCE)1090-0241(2007)133:1(30)
[18] Sabzi, Z., Fakher, A. 2012. The effect of confining stress on the analysis of excavations adjacent to existing buildings. International Conference on Geotechnique, Construction Materials and Environment, Kuala Lumpur, Malaysia, Nov 14-16, pp. 162-166.
[19] Hibbit, Karlsson, Sorensen, Inc., 2010. ABAQUS/Standard User's Manual, Version 6.10. Pawtucket, RI, USA.
[20] Brown, P.T., Booker, J.R. 1985. Finite element analysis of excavation .Computers and Geotechnics 1: 207.220.
[21] Duncan, J.M., Chang, C.Y. 1970. Nonlinear analysis of stress and strain in soils. Journal of the Soil Mechanics and Foundations Division, ASCE, 96, 5, 637-659.
[22] Khoiri, M., Ou, C.Y. 2013. Evaluation of deformation parameter for deep excavation in sand through case histories. Computers and Geotechnics 47, 57–67. DOI: 10.1016/j.compgeo.2012.06.009
[23] Dang, H., Lin, H., Juang, C. 2014. Analyses of braced excavation considering parameter uncertainties using a finite element code. Journal of the Chinese Institute of Engineers 37, 2, 141-151. DOI: 10.1080/02533839.2013.781790
[24] Dang, H., Lin, H., Juang, C. 2012. Evaluation of soil variability influence on deep excavation analysis–simplified approach. GeoCongress, pp. 2895-2903. DOI: 10.1061/9780784412121.296
[25] Verghese, S.J., Nguyen, C.T., Bui, H.H. 2013. Evaluation of plasticity-based soil constitutive models in simulation of braced excavation. Int. J. of GEOMATE. 5, 2, 672-677.
[26] Wong, K.S., Broms, B.B. 1989. Lateral deflection of braced excavation in clays. Journal of Geotechnical Engineering, ASCE, 115, 6, 853-870. DOI: 10.1061/(ASCE)0733-9410(1989)115:6(853)
[27] Duncan, J.M., Byrne, P., Wong, K.S, Mabry, P. 1980. Strength, stress-strain and bulk modulus parameters for finite element analysis of stresses and movements in soil masses. Report No. UCB/GT/80-01, College of Engineering, Office of Research Services, University of California, Berkley, Calif.
[28] Marr, W.A., Hawkes, M. 2010. Displacement-based design for deep excavations. ASCE, Earth Retention Conference 3: pp. 82-100. DOI: 10.1061/41128(384)6.
[29] Wood, M.D. 2004. Geotechnical Modelling. Spon, London.
[30] Sebastian B.L., Zapata-Medina, D.G. 2012. Method for estimating system stiffness for excavation support walls. J. Geotech. Geoenviron. Eng.138, 1104-1115. DOI: 10.1061/(ASCE)GT.1943-5606.0000683

NAPETOSTNO ODVISNO RAZMIKANJE PESKA UPOŠTEVAJOČ DROBLJENJE ZRN

Fangwei Yu
Chinese Academy of Sciences,
Institute of Mountain Hazards and Environment
Chengdu 610041, Kitajska

The University of Tokyo,
Department of Civil Engineering
Tokio 113-8656, Japonska

E-pošta: fwyuui@gmail.com

Ključne besede

kot razmikanja; strižni kot; drobljenje delcev; pesek; triosni preizkus

Izvleček

V članku je predstavljeno napetostno odvisno razmikanje peska z upoštevanjem drobljenja zrn. Za ta namen je bil izveden niz dreniranih triosnih preizkusov na kremenovem pesku številka 5 in predhodno zdrobljenih peskih, ki so bili pridobljeni z več dreniranimi triosnimi preizkusi na kremenovem pesku številka 5 pri 3 MPa bočnega tlaka, s čimer je ponazorjeno striženje peska pri visokih tlakih, to pa ima za posledico drobljenje delcev. Za podani začetni količnik por je bilo ugotovljeno, da ima drobljenje delcev za posledico zmanjšanje napetostno odvisnega razmikanja peska, kar se kaže bodisi kot kontrakcijsko obnašanje ali kot zmanjšanje maksimalne vrednosti kota razmikanja in s tem zmanjšanje dodatnega strižnega kota (razlika med vrhunsko vrednostjo strižnega kota ter strižnim kotom pri kritičnem stanju). Z uvedbo koncepta količnika por skeleta pri obravnavanju drobljenja zrn je predlagan linearen odnos za napetostno odvisno razmikanje v obliki zveze med maksimalnim kotom razmikanja, dodatnim strižnim kotom in vrhnjo vrednostjo količnika por skeleta v pol-logarimični ravnini. Ta zveza je nato razširjena na mobilizirano napetostno-deformacijsko stanje. Dobljena enačba napetostno odvisnega razmikanja, ki vključuje drobljenje zrn, je uporabna za oceno vpliva drobljenja zrn na napetostno odvisno razmikanje peska.

STRESS-DILATANCY BEHAVIOR OF SAND INCORPORATING PARTICLE BREAKAGE

Fangwei Yu
Chinese Academy of Sciences,
Institute of Mountain Hazards and Environment
Chengdu 610041, China

The University of Tokyo,
Department of Civil Engineering
Tokyo 113-8656, Japan

E-mail: fwyuui@gmail.com

Keywords

dilatancy angle; friction angle; particle breakage; sand; triaxial tests

Abstract

This paper presents the stress-dilatancy behavior of sand incorporating particle breakage. A series of the drained triaxial tests were conducted on the Silica sand No.5 and the pre-crushed sands that were produced by several drained triaxial tests on Silica sand No.5 under 3MPa confining pressure in simulating the high-pressure shear process to result in particle breakage, to investigate the stress-dilatancy behavior of sand incorporating particle breakage. For a given initial void ratio, particle breakage was found to result in deterioration of the stress-dilatancy behavior in the impairment of the dilatancy of sand to become more contractive with a reduction in the maximum dilatancy angle and the excess friction angle (the difference between the peak-state friction angle and the critical-state friction angle). By introducing the concept of the skeleton void ratio in considering particle breakage, a linear stress-dilatancy relationship between the maximum dilatancy angle-over-the excess friction angle and peak-state skeleton void ratio was proposed in semi-logarithmic plane and popularized to the mobilized stress-stain state as a stress-dilatancy equation pertaining to particle breakage, which would be useful in assessing the evolution of the stress-dilatancy behavior of sand during particle breakage.

1 INTRODUCTION

Since the dilatacny phenomenon of granular materials was firstly mentioned by Reynolds (1885) [17], the dilatancy behavior of soil plays a very significant role in soil behavior, e.g., stress-dilatancy behavior of soil (e.g., [4], [5], [18], [27]), and stress-dilatancy behavior of soil in relation to particle breakage or fine content (e.g., [6], [7], [19], [22], [25], [28], [29], [30]). For a given initial void ratio, the increase of the particle breakage or the non-plastic fines was found to lead to a decrease of the dilatancy behavior of soil in a great deal of previous studies (e.g., [2], [3], [14], [16], [20], [21], [28], [29], [30]). Also, particle breakage or non-plastic fines revealed a great influence on the critical state behavior of the soil: critical state line, critical-state stress and critical-state friction angle (e.g., [2], [16], [21], [26], [28], [29], [30]). In addition, the intergranular void ratio has been used to represent the behavior of the mixed soils (e.g., [13], [15], [19], [21]). The excess friction angle (the difference between peak-state friction angle and critical-state friction angle) was widely employed in relation to the peak-state dilatancy rate for representing the stress-dilatancy behavior of soils (e.g., [3], [4], [23], [27], [29]). However, a question arises as to what role particle breakage plays in the stress-dilatancy behavior of soil, especially for the stress-dilatancy equation of soil, which has not been fully studied yet.

In this paper, with the main attempt being to establish a stress-dilatancy equation incoporating particle breakage, a series of the drained triaxial test were conducted to investigate the influence of particle breakage on the stress-dilatancy behavior of the pre-crushed sands that were produced by several triaxial tests on Silica sand No.5 under 3MPa confining pressure in simulating the high-pressure shear process to result in particle breakage. The excess friction angle, dilatancy angle and the relation of the maximum dilatancy angle over the excess friction angle of the pre-crushed sands were discussed in detail in view of particle breakage. By introducing the skeleton void ratio in considering the influence of particle breakage, a linear relation between the maximum dilatancy angle-over-the excess friction angle and the peak-state skeleton void ratio was proposed in semi-logarithmic plane and extended to the mobilized stress-stain state as a stress-dilatancy equation for particle breakage.

2 LABORATARY EXPERIMENTS

2.1 Materials and methods

As a kind of natural silica sand, Silica sand No.5 from the Seto area of Aichi prefecture, Japan-which has some of the purest sands in Japan-was tested by triaxial tests in this paper with its physical properties in Table 1 and its original grain size distribution curve in Figure 1 (JGS 0131-2009, 2009 [9]; JGS 0161-2009, 2009 [10]). Silica sand No.5 is classified as a poorly graded sand (SP) according to the Unified Soil Classification System (ASTM D2487-11, 2011 [1]).

For consistency with the previous studies [28, 29, 30], a series of Consolidated-Drained (CD) triaxial tests were conducted on Silica sand No.5 and its pre-crushed sands using a strain-controlled high-pressure triaxial apparatus with maximum 3MPa confining pressure (JGS 0524-2009, 2009 [12]). All the specimens in diameter 75mm and height 160mm were prepared by air pluviation into a mound with a 1-mm-thick membrane in eight layers with the necessary tamping to reach the designated void ratio (JGS 0520-2009, 2009 [11]). To prevent the membrane from being pierced by sharp edges of soil particles and minimizing the membrane penetration under high effective stress, a 1-mm-thick membrane was employed for all the tests. All the triaxial tests were conducted on saturated specimens with Skempton's B value over 0.98 using the de-aired water to flush the specimens under around -100kPa vacuum.

After the shearing of each test, the whole material of the specimen was dried in an oven and later mixed uniformly, and then laid open uniformly as a thin cylinderical shape on a large tray, which was divided into four sectors uniformly. The diagonal two of them were removed until around 200g left by repeating this method, with the aim to have around 200g uniform material of specimen to sieve. Hereafter, the around 200g of specimen was employed for sieve analysis to obtain the grain size distribution curve (JGS 0131-2009, 2009 [9]).

Table 1. Physical properties of Silica sand No.5.

Property	Silica sand No.5
Specific gravity, G_s	2.761
Minimum void ratio, e_{min}	0.766
Maximum void ratio, e_{max}	1.215
Fine content, F_c	0.02%
Coefficient of uniformity, C_u	1.647
Coefficient of curvature, C_c	0.378

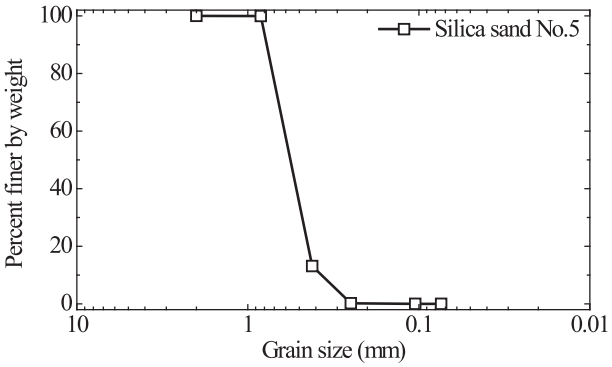

Figure 1. Original grain size distribution curve of silica sand No.5.

2.2 Quantification of particle breakage

In this paper, the Relative Breakage (B_r) [8] was introduced to assess the extent of particle breakage, where the area between initial grain size distribution curve and the grain size distribution curve after loading can be regarded as the total breakage B_t, and the area between initial grain size distribution curve and the vertical line of 0.075mm sieve size can be regarded as the breakage potential B_p. The relative breakage B_r is defined as a ratio of the total breakage B_t over the breakage potential B_p as illustrated in Figure 2.

2.3 Test results

As shown in Figure 3, several drained triaxial tests were sheared under 3MPa to the designated axial strain levels from 0% to 50% using a 10% increment for producing the crushed sands with progressively increased extent of particle breakage, which can be called the pre-crushed sands shown in Figure 4. Note that the original sand

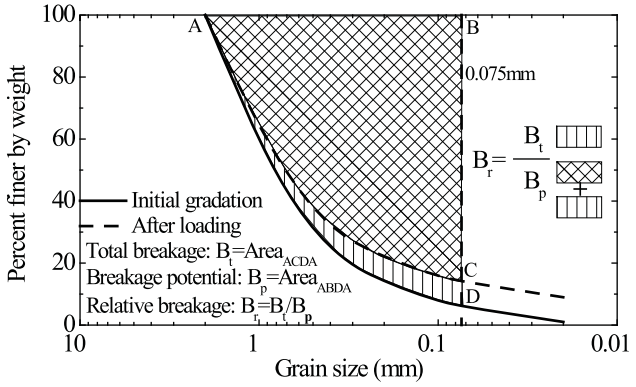

Figure 2. Definition of relative breakage (Hardin, 1985).

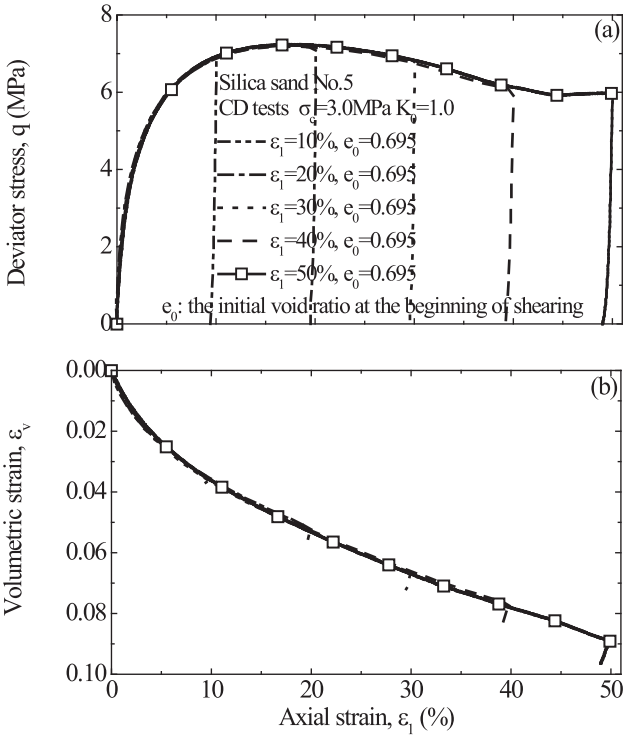

Figure 3. Drained shear tests for producing the pre-crushed sands.

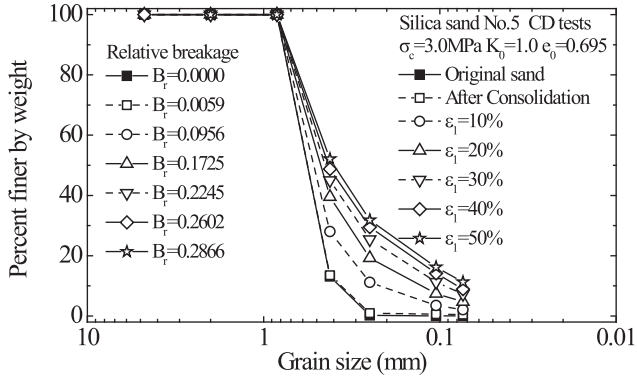

Figure 4. Grain size distribution curves of the pre-crushed sands.

can be regarded as a kind of pre-crushed sand with B_r=0.0000, and the original sand and pre-crushed sands are hereafter called the pre-crushed sands by a general designation. For investigating the influence of particle breakage on the stress-dilatancy behavior of sand, the

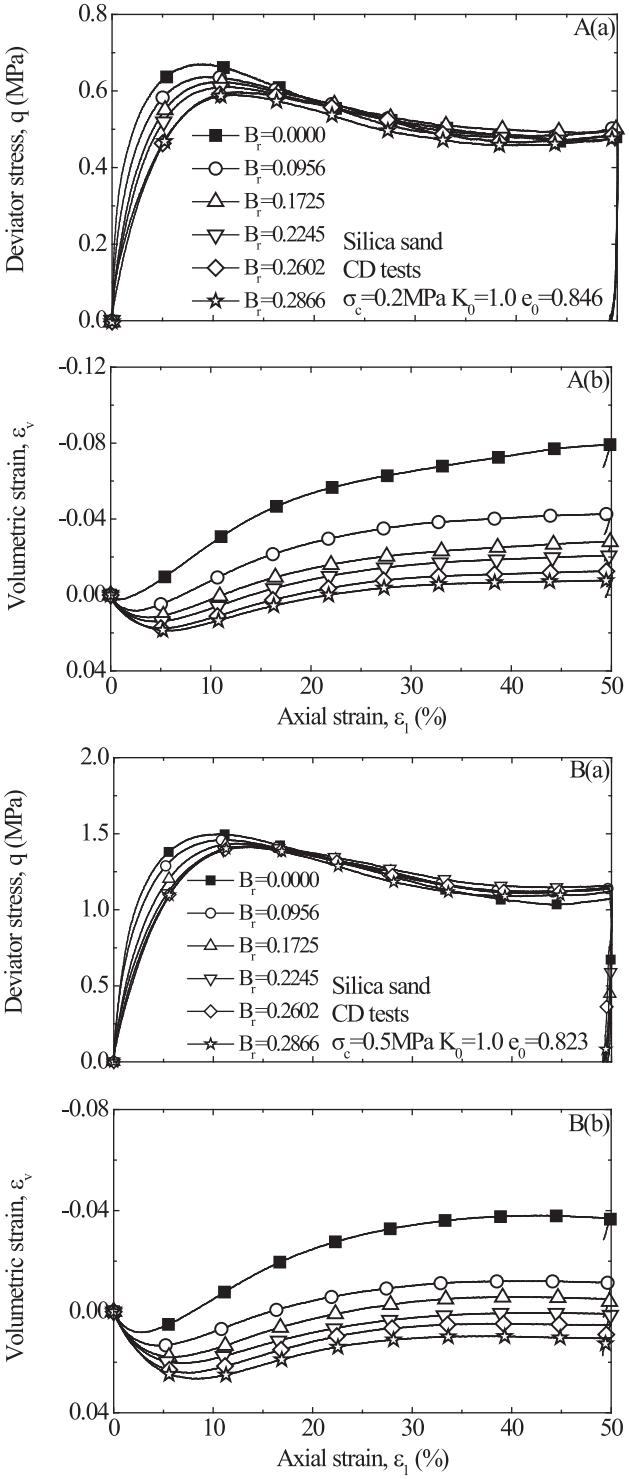

Figure 5. Drained shear results on the pre-crushed sands: (A) under 0.2MPa; (B) under 0.5MPa.

pre-crushed sands were re-employed to constitute the new specimens, which would reach the same initial void ratio after the isotropically drained consolidation and then would be re-sheared to reach the critical states under 0.2MPa and 0.5MPa confining pressures, respectively, as shown in Figure 5. Herein, the 0.2MPa and 0.5MPa, as the relatively low confining pressures were employed in the drained triaxial shear for trying not to crush the pre-crushed sands any more in clearly detecting the influence of particle breakage on the shear behavior of the pre-crushed sands. Note that the particle breakage has a significant influence on the soil behavior, e.g., for a given initial void ratio, particle breakage results in a deterioration of stress-strain behavior in the impairment of dilatancy of sand to become more contractive.

3 DISCUSSION

3.1 Angles of shearing and dilatancy

The shear strength and dilatancy of soil has a significant influence on soil behavior. The mobilized angles of shearing and dilatancy of soil are defined and given respectively by

$$\sin\varphi_m = \left[\frac{\sigma_1'/\sigma_3' - 1}{\sigma_1'/\sigma_3' + 1}\right]_m \qquad (1)$$

$$\sin\psi_m = \left[-\frac{d\varepsilon_v}{d\gamma_{13}}\right]_m \qquad (2)$$

where φ_m is the mobilized angle of shearing, ψ_m is the mobilized angle of dilatancy, σ_1'/σ_3' is the mobilized effective principal stress ratio, $d\varepsilon_v$ is the volumetric strain increment and $d\gamma_{13}$ is the maximum shear strain increment that can be calculated by $d\gamma_{13}=2d\varepsilon_1-d\varepsilon_v$ ($d\varepsilon_1$ is the axial strain increment) for the plain strain shear and traditional triaxial shear (e.g., [4], [19]).

By introducing the peak-state and critical-state stresses and strains to equations (1) and (2), the angles of shearing and dilatancy in peak state and critical state would be obtained, as represented by φ_{ps} and ψ_{ps} for peak-state friction angle and peak-state dilatancy angle, respectively, and by φ_{cs} and ψ_{cs} for critical-state friction angle and critical-state dilatancy angle, respectively.

The excess friction angle ([23], [27], [29]) is defined as

$$\varphi_{excess} = \varphi_{ps} - \varphi_{cs} \qquad (3)$$

And, corresponding to the concept of the excess friction angle, the excess dilatancy angle ψ_{excess} can be also be defined by

$$\psi_{excess} = \psi_{ps} - \psi_{cs} \qquad (4)$$

In addition, the maximum dilatancy rate of soil is widely accepted to be associated with the peak state of shear (e.g., [4]), which means that the peak-state dilatancy angle ψ_{ps} could be treated as being equal to the maximum dilatancy angle $\psi_{\max}$, i.e. $\psi_{ps}=\psi_{\max}$. And the critical-state dilatancy angle would be equal to zero, i.e. $\psi_{cs}=0$, according to the concept of critical state.

Therefore, the equation (4) gives

$$\psi_{excess} = \psi_{ps} = \psi_{\max} \qquad (5)$$

Figure 6 shows that the excess friction angles decrease approximately in up concavity to converge with increasing particle breakage. As shown in Figure 7, the maximum dilatancy angles are found to decrease gradually in slightly up concavity with increasing particle breakage. It is evident to image that the excess friction angle and maximum dilatancy angle should finally converge to a constant with increasing particle breakage to the limit particle breakage, i.e., the ratio of maximum dilatancy

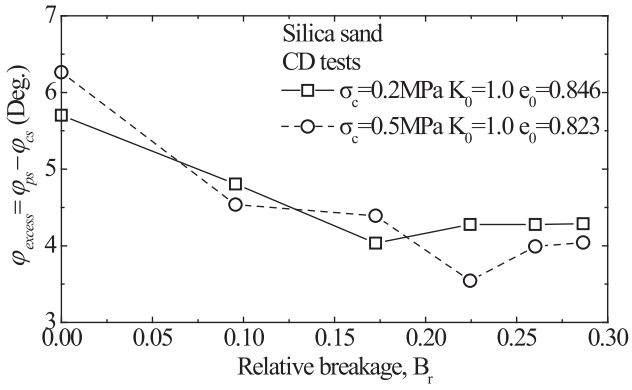

Figure 6. Evolution of the excess friction angle against relative breakage.

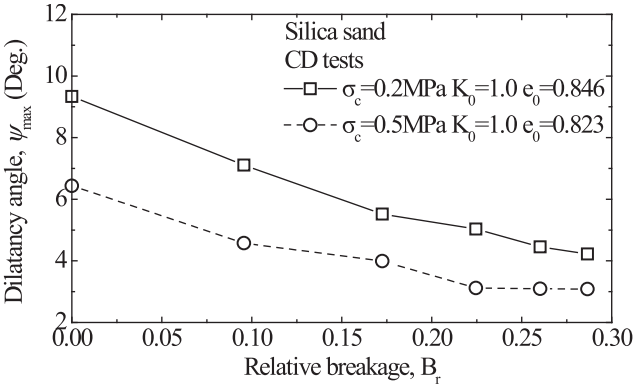

Figure 7. Evolution of the maximum dilatancy angle against relative breakage.

angle over the excess friction angle should finally converge gradually to a constant with increasing particle breakage to the limit particle breakage. Figure 8 shows the evolution of the maximum dilatancy angle-over-the excess friction angle (or the excess dilatancy angle-over-the excess friction angle) against the relative breakage, i.e., in detail, the ratio of the maximum dilatancy angle-over-the excess friction angle decreases gradually in down concavity.

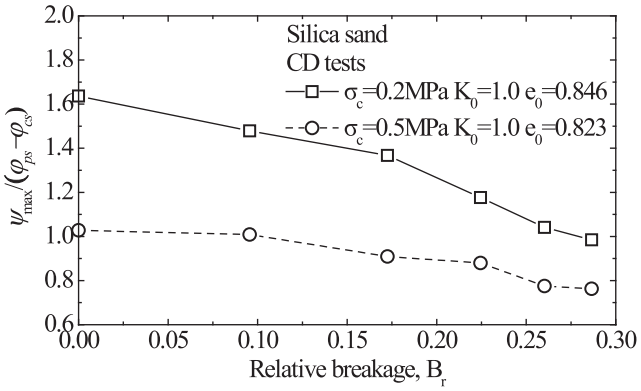

Figure 8. Evolution of the maximum dilatancy angle-over-the excess friction angle against relative breakage.

3.2 Microstructure framework for the pre-crushed sands

The increased fine content that squeezed into voids among the sand particles would result in the reduction of the maximum void ratio and minimum void ratio, which represents a reduction in the void ratios (e.g., [14], [19], [21]). For a given overall void ratio of soil with almost all the fines in voids, in the microstructure framework of granular mix, the skeleton void ratio e_{skfc} (e.g., [13], [19], [21]) can be approximately in consideration of the composite mix of coarse and fine grain skeletons as if the fines were voids, as defined by

$$e_{skfc} = \frac{1+e}{1-f_c} - 1 \qquad (6)$$

where e is the void ratio and f_c is the fine content.

As shown in Figure 3, the pre-crushed sands were produced by the progressive triaxial shear on poorly graded silica sand No.5 with very few initial fine content and lots of voids among the soil particles. With the progressive triaxial shear, the particle breakage in pre-crushed sands were regarded as being progressive, and the fine content in the pre-crushed sands can be assumed to be squeezed into the voids in the sand skeleton as if the fines were voids in being same as the concept of the skeleton void ratio. Consequently, for the pre-crushed sands with progressive particle breakage, the skeleton void ratio was introduced and redefined as the relative breakage skeleton void ratio in replacing the fine content f_c by the relative breakage B_r for considering particle breakage, as represented by

$$e_{sk} = \frac{1+e}{1-B_r} - 1 \qquad (7)$$

where e is the void ratio of original sand and B_r is the relative breakage ($0 \le B_r < 1$ corresponding to $e \le e_{sk}$). The e_{sk} with (B_r=0) is equal to the void ratio of original sand (B_r=0), and the e_{sk} is to increase monotonically with increasing particle breakage (B_r) which reveals that e_{sk} can interpret the influence of particle breakage produced by the original sand on the void ratio.

3.3 Stress-dilatancy behavior incorporating particle breakage

As illustrated in Figure 9 and Figure 10, both the excess friction angle and the maximum dilatancy angle decrease in up concavity when increasing the peak-state skeleton void ratio, which are consistent with the findings found in Figure 6 and Figure 7. As mentioned above, the ratio of maximum dilatancy angle over the

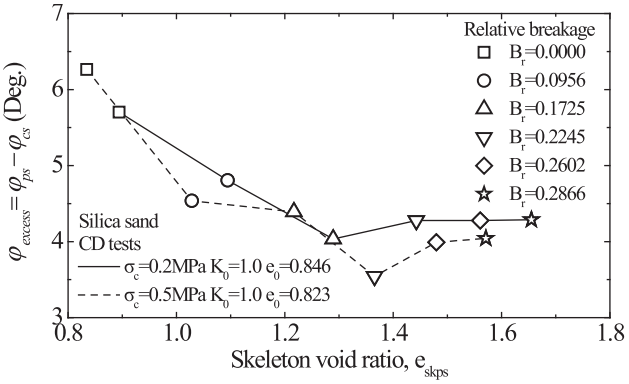

Figure 9. Evolution of the excess friction angle against peak-state skeleton void ratio.

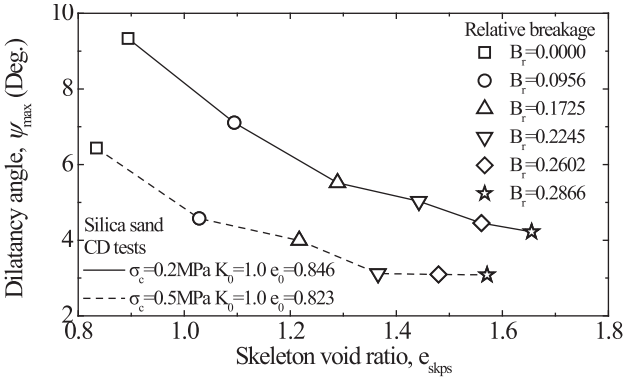

Figure 10. Evolution of the maximum dilatancy angle against peak-state skeleton void ratio.

excess friction angle should finally converge gradually to a constant with increasing particle breakage to the limit particle breakage. Meanwhile, in view of the mapping from B_r in domain [0,1) to e_{sk} in domain [e,∞), a linear relation of the maximum dilatancy angle-over-the excess friction angle and the peak-state skeleton void ratio can be drawn in semi-logarithmic plane, as displayed in Figure 11. It is also shown in Figure 11 that the different confining pressures have a significant influence on this stress-dilatancy relation, i.e., lower stress (0.2MPa) results in a much sharper decrease than the relative higher stress (0.5MPa).

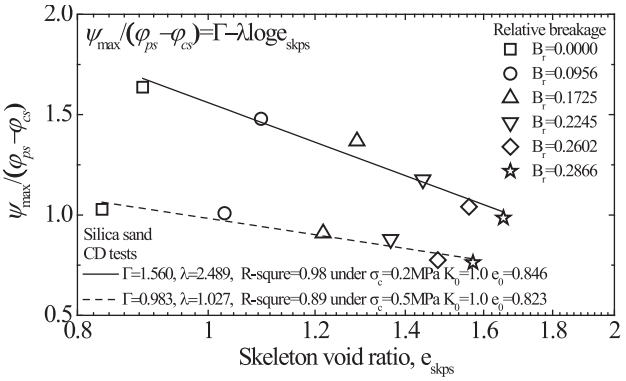

Figure 11. Evolution of the maximum dilatancy angle-over-the excess friction angle against peak-state skeleton void ratio.

As shown in Figure 11, the linear correlation between $\psi_{max}/\varphi_{excess}$ and e_{sk} can be represented by

$$\psi_{max}/\varphi_{excess}=\Gamma-\lambda\log e_{skps} \qquad (8)$$

where Γ and λ are the model parameters. By substituting equations (2), (3) and (7) into equation (8), equation (8) can be rearranged by

$$\left[-\frac{d\varepsilon_v}{d\gamma_{13}}\right]_{max}=\sin\left\{\left[\Gamma-\lambda\left(\log\frac{1+e_{ps}}{1-B_r}-1\right)\right]\left(\varphi_{ps}-\varphi_{cs}\right)\right\} \qquad (9)$$

The relation, i.e., equation (9), can be extended into the whole shear stage in replacing the peak-state variables: maximum dilatancy angle, peak-state friction angle and peak-state void ratio by the mobilized variables during shear [24], as rewritten by

$$\left[-\frac{d\varepsilon_v}{d\gamma_{13}}\right]_{m}=\sin\left\{\left[\Gamma-\lambda\left(\log\frac{1+e}{1-B_r}-1\right)\right]\left(\varphi_m-\varphi_{cs}\right)\right\} \qquad (10)$$

where e is the void ratio of the original sand, φ_m=arcsin[(σ_1'/σ_3' -1)/(σ_1'/σ_3'+1)]$_m$ is the mobilized friction angle. Equation (10) as a stress-dilatancy relation in relation to particle breakage (B_r) can be employed for application in assessing the evolution of the stress-dilatancy behavior of sand in considering the particle breakage.

4 CONCLUSIONS

A series of the drained triaxial tests were conducted on the Silica sand No.5 and the pre-crushed sands that were produced by several drained triaxial tests on Silica sand No.5 under 3MPa confining pressure in simulating the high-pressure shear process to result in particle breakage, to investigate the stress-dilatancy behavior of sand incorporating particle breakage. The major findings can be summarized as what follows:

a) For a given initial void ratio, particle breakage had a significant influence on the stress-dilatancy behavior, in impairment of dilatancy of sand to become more contractive. The skeleton void ratio was introduced in replacing the fine content by relative breakage to consider the influence of the particle breakage.
b) A linear relation between $\psi_{max}/(\varphi_{ps}-\varphi_{cs})$ and e_{skps} was proposed in $\psi_{max}/(\varphi_{ps}-\varphi_{cs})$ - log e_{skps} plane and popularized to the mobilized stress-strain state for establishing a new stress-dilatancy equation pertaining to particle breakage in assessing the stress-dilatancy behavior subjected to particle breakage.

Acknowledgements

This work was supported by the Chinese Academy of Sciences (CAS) "Light of West China" Program (Grant No.Y6R2250250), the Key Research Program of Frontier Sciences, CAS (Grant No.QYZDB-SSW-DQC010), the National Basic Research Program of China (973 Program) (Grant No.2013CB733201), the One-Hundred Talents Program of Chinese Academy of Sciences (Lijun Su) and the China Scholarship Council (Grant No.2011671035). A special acknowledgement should be expressed to Professor Ikuo Towhata for his invaluable assistance in the performance of the tests in this paper in the Geotechnical Engineering Laboratory of The University of Tokyo, Japan.

REFERENCES

[1] ASTM D2487-11, 2011. Standard Practice for Classification of Soils for Engineering Purposes (Unified Soil Classification System). ASTM International, West Conshohocken, PA. DOI:10.1520/D2487-11.
[2] Bandini, V., Coop, M.R. 2011. The influence of particle breakage on the location of the critical state line of sands. Soils and Foundations 51, 4, 591-600. DOI:10.3208/sandf.51.591.
[3] Been, K., Jefferies, M.G. 1985. A state parameter for sands. Geotechnique 35, 2, 99-112. DOI:10.1680/geot.1985.35.2.99.

[4] Bolton, M.D. 1986. The strength and dilatancy of sands. Geotechnique 36, 1, 65-78. DOI:10.1680/geot.1986.36.1.65.
[5] De Silva, L.I.N., Koseki, J., Wahyudi, S., Sato, T. 2014. Stress–dilatancy relationships of sand in the simulation of volumetric behavior during cyclic torsional shear loadings. Soils and Foundations 54, 4, 845-858. DOI:10.1016/j.sandf.2014.06.015.
[6] Hamidi, A., Alizadeh, S.M., Soleimani, M. 2009. Effect of particle crushing on shear strength and dilation characteristics of sand-gravel mixtures. International Journal of Civil Engineering 7, 61-72. DOI:10.3328/IJGE.2009.03.01.29-38.
[7] Hamidi, A., Soleimani, M. 2012. Shear strength-dilation relation in cemented gravely sands. International Journal of Geotechnical Engineering 6, 415-425. DOI:10.1179/1939787913Y.0000000026.
[8] Hardin, B.O. 1985. Crushing of soil particles. Journal of Geotechnical Engineering 111, 10, 1177-1192. DOI:10.1061/(ASCE)0733-9410(1985)111:10(1177).
[9] JGS 0131-2009. 2009. Laboratory Testing Standards of Geomaterials: Tests for physical properties-Test Method for Particle Size Distribution of Soils of Soils. The Japanese Geotechnical Society, Tokyo, Japan.
[10] JGS 0161-2009. 2009. Laboratory Testing Standards of Geomaterials: Tests for physical properties-Test Method for Minimum and Maximum Densities of Sands. The Japanese Geotechnical Society, Tokyo, Japan.
[11] JGS 0520-2009. 2009. Laboratory Testing Standards of Geomaterials:Tests for Mechanical Properties-Preparation of Soil Specimens for Triaxial Tests. The Japanese Geotechnical Society, Tokyo, Japan.
[12] JGS 0524-2009. 2009. Laboratory Testing Standards of Geomaterials: Tests for Mechanical Properties- Method for Consolidated Drained Triaxial Compression Test on Soils. The Japanese Geotechnical Society, Tokyo, Japan.
[13] Kuerbis, R.H. 1989. Effect of gradation and fines content on the undrained response of sand. Master thesis, The University of British Columbia. DOI:10.14288/1.0062832.
[14] Lade, P.V., Yamamuro, J.A. 1997. Effects of nonplastic fines on static liquefaction of sands. Canadian Geotechnical Journal 34, 6, 918-928. DOI:10.1139/t97-052.
[15] Murthy, T.G., Loukidis, D., Carraro, J.A.H., Prezzi, M., Salgado, R. 2007. Undrained monotonic response of clean and silty sands. Geotechnique 57, 3, 273-288. DOI:10.1680/geot.2007.57.3.273.
[16] Ni, Q., Tan, T.S., Desari, G.R., Hight, D.W. 2004. Contribution of fines to the compressive strength of mixed soils. Geotechnique 54, 9, 561-569. DOI:10.1680/geot.2004.54.9.561.
[17] Reynolds, O. 1885. On the dilatancy of media composed of rigid particles in contact with experimental illustrations. Philosophical Magazine 5, 20, 469-481. DOI:10.1080/14786448508627791.
[18] Rowe, P.W. 1962. The stress-dilatancy relation for static equilibrium of an assembly of particles in contact. Proceedings of the Royal Society, London, A269:500-527. DOI:10.1098/rspa.1962.0193.
[19] Salgado, R., Bandini, P., Karim, A. 2000. Shear strength and stiffness of silty sand. Journal of Geotechnical and Geoenvironmental Engineering 126, 5, 451-462. DOI:10.1061/(ASCE)1090-0241(2000)126:5(451).
[20] Thevanayagam, S. 1998. Effect of fines and confining stress on undrained shear strength of silty sands. Journal of Geotechnical and Geoenvironmental Engineering 124, 6, 479-491. DOI:10.1061/(ASCE)1090-0241(1998)124:6(479).
[21] Thevanayagam, S., Shenthan, T., Mohan, S., Liang, J. 2002. Undrained Fragility of clean sands, silty sands and sandy silts. Journal of Geotechnical and Geoenvironmental Engineering 128, 10, 849-859. DOI:10.1061/(ASCE)1090-0241(2002)128:10(849).
[22] Ueng, Tzou-shin, Chen, Tse-jen. 2000. Energy aspects of particle breakage in drained shear of sands. Geotechnique 50, 1, 65-72. DOI:10.1680/geot.2000.50.1.65.
[23] Vaid, Y.P., Sasitharan, S. 1992. The strength and dilatancy of sand. Canadian Geotechnical Journal 29, 3, 522-526. DOI:10.1139/t92-058.
[24] Wang, R.G., Guo, P.J. 1998. A simple constitutive model for granular soils: modified stress-dilatancy approach. Computers and Geotechnics 22, 2, 109-133. DOI:10.1016/S0266-352X(98)00004-4.
[25] Xiao, Y., Liu, H., Chen, Y., Chu, J. 2014. Strength and dilatancy of silty sand. Journal of Geotechnical and Geoenvironmental Engineering 140, 7, 06014007. DOI:10.1061/(ASCE)GT.1943-5606.0001136.
[26] Xiao, Y., Liu, H.L., Ding, X.M., Chen, Y.M., Jiang, J.S., Zhang, W.G. 2016. Influence of particle breakage on critical state line of rockfill material. International Journal of Geomechanics 16, 1, 04015031. DOI: 10.1061/(ASCE)GM.1943-5622.0000538.
[27] Xiao, Y., Liu, H.L., Sun, Y.F., Liu, H., Chen, Y.M. 2015. Stress-dilatancy behaviors of coarse granular soils in three-dimensional stress space. Engineering Geology 195, 104-110. DOI:10.1016/j.enggeo.2015.05.029.
[28] Yu, F.W. 2017a. Particle breakage and the critical state of sands. Geotechnique DOI:10.1680/jgeot.15.P.250. (Published online).
[29] Yu, F.W. 2017b. Particle breakage and the drained shear behavior of sands. International Journal of Geomechanics 17, 8, 04017041. DOI:10.1061/(ASCE)GM.1943-5622.0000919. (In press).
[30] Yu, F.W., Su, L.J. 2016. Particle breakage and the mobilized drained shear strengths of sand. Journal of Mountain Science 13, 8, 1481-1488. DOI:10.1007/s11629-016-3870-1.

NAPOVED KALIFORNIJSKEGA INDEKSA NOSILNOSTI (CBR) IN LASTNOSTI ZGOSTITVE ZRNATIH ZEMLJIN

Attique ul Rehman *(vodilni avtor)*
University of Lahore,
Department of Civil Engineering
Lahore, Pakistan
E-pošta: attiq.engr@gmail.com

Khalid Farooq
University of Engineering and Technology,
Department of Civil Engineering
Lahore, Pakistan

Hassan Mujtaba
University of Engineering and Technology,
Department of Civil Engineering
Lahore, Pakistan

Ključne besede

CBR, regresija, model, napoved, karakteristike zgostitve

Izvleček

V pričujoči študiji je podan poskus korelacije indeksnih lastnosti zrnatih zemljin s kalifornijskim indeksom nosilnosti (CBR) in lastnosti zgostitve. Na naravnih in kompozitnih vzorcih peskov so bile skladno z ASTM metodami izvedene klasifikacija zemljin, modificirani Proctorjev preizkus in CBR preizkus. Rezultati laboratorijskih preiskav so pokazali, da vzorci v študiji spadajo med kategorije SW, SP in SP-SM, skladno s sistemom enotne klasifikacije zemljin in v skupini A-1-b in A-3, skladno z AASHTO klasifikacijskim sistemom. Na podatkih eksperimentov je bila izvedena multipla linearna regresijska analiza in razvite korelacije za napoved CBR, maksimalne suhe gostote in optimalne vlažnosti glede na indeksne lastnosti vzorcev. Med različnimi parametri so se za napovedovanje izkazali za najboljše koeficient enakomernosti (C_u), velikost zrn pri 30 % presejku (D_{30}) in pri 50 % presejku (D_{50}). Predlagani modeli za napoved zgornjih lastnosti so bili potrjeni na bazi neodvisnih podatkov CBR preizkusov peščenih zemljin. Primerjalni rezultati kažejo, da je variacija med eksperimentalnimi in napovedanimi rezultati za CBR znotraj ±4 % intervala zaupanja, in za maksimalno suho gostoto ter optimalno vlažnost znotraj ±2 %. Na osnovi korelacij, razvitih za CBR, maksimalno suho gostoto in optimalno vlažnost, so predlagane napovedovalne krivulje za hitro oceno teh lastnosti na osnovi C_u, D_{30} in D_{50}. Predlagani modeli in napovedovalne krivulje za oceno CBR vrednosti in lastnosti zgostitve so lahko zelo uporabni v geotehničnem inženirstvu in dimenzioniranju voziščnih konstrukcij, ne da bi izvedli laboratorijske preiskave zgostitve in CBR preizkuse.

PREDICTION OF CALIFORNIA BEARING RATIO (CBR) AND COMPACTION CHARACTERISTICS OF GRANULAR SOILS

Attique ul Rehman *(corresponding author)*
University of Lahore,
Department of Civil Engineering
Lahore, Pakistan
E-mail: attiq.engr@gmail.com

Khalid Farooq
University of Engineering and Technology,
Department of Civil Engineering
Lahore, Pakistan

Hassan Mujtaba
University of Engineering and Technology,
Department of Civil Engineering
Lahore, Pakistan

Keywords

CBR, regression, model, prediction, compaction characteristics

Abstract

This research is an effort to correlate the index properties of granular soils with the California Bearing Ratio (CBR) and the compaction characteristics. Soil classification, modified proctor and CBR tests conforming to the relevant ASTM methods were performed on natural as well as composite sand samples. The laboratory test results indicated that samples used in this research lie in SW, SP and SP-SM categories based on Unified Soil Classification System and in groups A-1-b and A-3 based on the AASHTO classification system. Multiple linear regression analysis was performed on experimental data and correlations were developed to predict the CBR, maximum dry density (MDD) and optimum moisture content (OMC) in terms of the index properties of the samples. Among the various parameters, the coefficient of uniformity (C_u), the grain size corresponding to 30% passing (D_{30}) and the mean grain size (D_{50}) were found to be the most effective predictors. The proposed prediction models were duly validated using an independent dataset of CBR tests on sandy soils. The comparative results showed that the variation between the experimental and predicted results for CBR falls within ±4% confidence interval and that of the maximum dry density and the optimum moisture content are within ±2%. Based on the correlations developed for CBR, MDD and OMC, predictive curves are proposed for a quick estimation based on C_u, D_{30} and D_{50}. The proposed models and the predictive curves for the estimation of the CBR value and the compaction characteristics would be very useful in geotechnical & pavement engineering without performing the laboratory compaction and CBR tests.

1 INTRODUCTION

An appropriate and sound foundation is always required for the construction of all kinds of engineering projects, especially those involving large quantities of earth works, like pavements, runways, railway formations and pavement embankments, etc. Bearing capacity, swell potential and the settlement of different layers of pavements should be within tolerable limits. Therefore, it is necessary to have reliable methods to access the engineering properties of such projects. The California Bearing Ratio (*CBR*) is one of the most common methods to design and assess the strength of different pavement layers by comparing them with the strength of standard California crushed rock. The *CBR* value is used to determine the thickness of pavement layers and also to evaluate the shear strength and stiffness modulus of sub-grade material. Similarly, an evaluation of the compaction characteristics (*OMC* and *MDD*) for

projects involving large quantities of earthworks is also an essential requirement, and these parameters are also used in the evaluation of the *CBR* value. Both the *CBR* value and the compaction characteristics are very much dependent on soil gradation and other index properties in the case of granular soils.

Engineers encounter many difficulties in obtaining a reliable *CBR* value because of insufficient soil investigation data and limited time during the pre-feasibility stages of the project. At least 4 days are required to generate a soaked *CBR* value for a single soil specimen and multiple *CBR* tests are required on subgrade samples along the length of the pavement to obtain a representative design *CBR* value. In order to save time during the pre-feasibility stages, researchers have therefore developed prediction models to correlate the *CBR* value with various index properties of the soils.

As mentioned earlier, the *CBR* value is mainly dependent on various index properties of the soil; therefore, many researchers have conducted research studies to understand the effect of soil type and soil characteristics on the *CBR* value of both coarse-grained and fine-grained soils. Based on their research, various researchers including Agarwal and Ghanekar [1], National Cooperative Highway Research Program(NCHRP)[2], Breytenbach [3], Roy et al. [4], Ferede [5], Patel and Desai [6], Saklecha et al. [7], Yildirim and Gunaydin [8], Singh et al. [9], Taha et al. [10] and Talukdar [11] have proposed correlations to predict the *CBR* value for various types of soils based on their index properties. These correlations are summarized in Table 1, followed by their relevant discussion.

Agarwal and Ghanekar [1] used forty-eightfine-grained soil samples to correlate the *CBR* value with the liquid limit (*LL*) and optimum moisture content (*OMC*). The National Cooperative Highway Research Program (NCHRP) [2] presented a correlation between the grain size corresponding to 60% passing (D_{60}) and the *CBR* value. The applicability of the proposed correlation is limited for D_{60} varying between 0.01 mm to 30 mm. The recommended value of *CBR* is 5 when D_{60} is less than 0.01 mm and the *CBR* value is 95 when D_{60} is greater than 30 mm. Breytenbach [3] correlated the *CBR* value with the plasticity index (*PI*) and grading modulus (GM) based on the research work conducted on a variety of soils present in various parts of South Africa. Roy et al. [4] proposed an equation to estimate the *CBR* value on the basis of the maximum dry unit weight, the unit weight of water and the optimum moisture content for fine-grained soils. Ferede [5] developed correlations to predict the *CBR* value using D_{60} , the optimum moisture content (*OMC*) and the maximum dry density (*MDD*) for granular soils and liquid limit (*LL*), plastic limit (PL), plasticity index (*PI*) and percentage of fines (F_{200}) for fine-grained soils. Pateland Desai[6] proposed correlations to estimate the soaked and unsoaked *CBR* values based on compaction parameters (*MDD* and *OMC*) and the plasticity index of fine-grained soil. Saklecha et al. [7] performed multiple

Table 1. Correlations for predicting *CBR* proposed by various researchers.

Correlations	Reference
$CBR = 2 - \log(OMC) + 0.07\ LL$	Agarwal and Ghanekar (1970)
$CBR = 28.09\ (D_{60})^{0.358}$	NCHRP (2001)
$CBR = 26.382 \times (0.458\ PI) + 5.278\ GM$	Breytenbach (2009)
$\log CBR = \log(\gamma_{dmax} / \gamma_w) - \log OMC$	Roy et al. (2009)
$CBR = 68.789 - 11.925\ D_{60} + 0.897\ D_{60}^2 - 0.025\ D_{60}^3$	Ferede (2010)
$CBR = -27.998 + 0.029\ OMC^2 + 4.796\ MDD^4$	
$CBR = 4.175 - 0.029\ LL - 0.009\ F_{200}$	
$CBR(\text{Soaked}) = 43.907 - 0.093\ I_p - 18.78\ MDD - 0.3081\ OMC$	Patel and Desai (2010)
$CBR(\text{Unsoaked}) = 17.009 - 0.0696\ I_p - 0.296\ MDD + 0.0648\ OMC$	
$CBR = 0.26O\ MC + 42.55\ MDD - 73.62$	Saklecha et al. (2011)
$CBR = 0.22\ G + 0.045\ S + 4.739\ MDD + 0.122\ OMC$	Yildirim and Gunaydin (2011)
$CBR(\text{Soaked}) = -2.213 - 0.055[(MC/OMC)\times 100] + 0.328[(\text{Density}/MDD)\times 100] - 1.147\ PL$	Singh et al. (2011)
$CBR = 0.025\ F_{200}^4 + 30.130(MDD) - 25.813$	Taha et al. (2013)
$CBR(\text{Soaked}) = 0.127\ LL - 0.16\ PI + 1.405\ MDD - 0.259\ OMC + 4.62$	Talukdar (2014)

CBR = California Bearing Ratio, *LL* = Liquid limit, *PL* = Plastic limit, $PI = I_p$ = Plasticity index. *OMC* = Optimum moisture content, *MDD* = Maximum dry density, γ_{dmax} = Maximum dry unit weight, γ_w = Unit weight of water, D_{60} = grain size corresponding to 60% passing, *G* = Percentage of gravels, *S* = Percentage of sand, F_{200} = Percentage of fines, *GM* = Grading modulus

regression analyses to correlate the *CBR* with the compaction parameters (*MDD* and *OMC*) of sub-grade soil. Yildirim and Gunaydin [8] utilized fine-grained as well as coarse-grained soils comprising a wide range of grain sizes to develop prediction models for the estimation of *CBR* values based on the compaction parameters (*MDD* and *OMC*), the percentage of gravel (G) and the sand content (S). Singh et al. [9] collected five different soils from West Bengal and tested them in the laboratory at four different compaction energy levels and five different moisture contents. A prediction model for soaked *CBR* was proposed by considering the effect of the degree of compaction and moisture content. Taha et al. [10] correlated the *CBR* value with the index properties of Egyptian soil. They found after their study that the percentage of fines (F_{200}) and *MDD* are the most effective parameters to predict the *CBR* value. Talukdar [11] used multiple linear regression analysis (MLRA) to correlate the soaked *CBR* value with the index properties of fine-grained soil from the Assam state of India.

Also, various researchers proposed correlations to predict the compaction characteristics based on soil index properties. Sivrikaya et al. [12] focused on the prediction of compaction parameters for granular soils and used two approaches, named multiple linear regression (MLR) and Genetic Expression Programming (GEP), to develop correlations. Mujtaba et al. [13] used granular soil samples to propose predictive models using gradation parameters and compaction energy (CE) for predicting the maximum dry unit weight (γ_{dmax}) and the optimum moisture content (*OMC*). The prediction models presented by [13] are given in Eq.(1)and Eq. (2), respectively.

Omar et al.[14] developed prediction models to estimate the compaction characteristics of granular soil present in the United Arab Emirates.The prediction models developed in their research are presented in Eqs. (3) and (4). Noor et al. [15] collected 106 samples of fine-grained soils from various Indian Hydropower projects to develop prediction models for the estimation of compaction parameters given in Eq. (5) and Eq. (6). Boltz et al. [16] proposed correlations for fine-grained soil based on the liquid limit (*LL*) and the compaction energy (*E*), as presented in Eqs.(7) and (8). Sridharan and Nagaraj [17] found that only the plastic limit (ω_p) can give good estimates of compaction parameters. Their proposed correlations are presented in Eqs. (9) and (10).

$$\gamma_{dmax} = 4.49 \log(C_u) + 1.51 \log(CE) + 10.2 \quad (1)$$

$$\log OMC\ (\%) = 1.67 - 0.193 \log(C_u) - 0.153 \log(CE) \quad (2)$$

$$\rho_{dmax}(\mathrm{kg/m^3}) = [4804574\ G_s - 195.55(LL^2) + 156971(\mathrm{R\#4})^{0.5} - 9527830]^{0.5} \quad (3)$$

$$\ln(\omega_0) = 1.195\times10^{-4}\ (LL^2) - 1.964\ G_s - 6.617\times10^{-3}\ (\mathrm{R\#4}) + 7.651 \quad (4)$$

$$MDD = \sqrt{\mathrm{PL}} - 0.089\ LL + 33.97/(PL+1.37) + 19.05 \quad (5)$$

$$OMC = PI/\mathrm{G} + 3.424 + 0.462\ PL - G \quad (6)$$

$$MDD = (2.27 \log LL - 0.94) \log E - 0.16\ LL + 17.02 \quad (7)$$

$$OMC = (12.39 - 12.21 \log LL)\log E + 0.67\ LL + 9.21 \quad (8)$$

$$\gamma_{dmax} = 0.23(93.3 - \omega_P) \quad (9)$$

$$OMC = 0.92\ \omega_P \quad (10)$$

The present research is mainly focused on proposing prediction models to estimate the *CBR*, the *MDD* and the *OMC* in the case of granular soils present in various areas of the Punjab province of Pakistan, based on their index properties. The index parameters including D_{50}, D_{30} and C_u obtained from the results of grain size analysis were used for the estimation of the *CBR*, *MDD* and *OMC* of the coarse-grained soils.

2 MATERIALS AND METHODS

The major sources of soil samples were local deposits of granular soils commercially known as Ravi, Chenab and Lawrencepur sands, which have been used in this study. A total of seventy soil samples were tested, including natural sand samples and composite sand samples prepared by mixing the above-mentioned sands in different proportions. The soil samples were classified as poorly graded sand (SP), well-graded sand (SW) and poorly graded sand with silt (SP-SM),as per the Unified Soil Classification System (USCS) [18]. Similarly, according to the AASHTO classification system, soil samples lie in A-1-b and A-3 groups [19]. All the tests were conducted on every sample according to the standard test procedures described in the relevant ASTM standards. The grain size analysis test was performed in accordance with ASTM-D422 [20], where a modified Proctor compaction test was carried out in the laboratory following the test procedure of ASTM-D1557 [21]. For the determination of the California Bearing Ratio (*CBR*), soil samples were compacted at optimum moisture content, corresponding to the maximum dry density, which was obtained by performing a modified Proctor test on every sample.

Compacted soil samples were then soaked in water for 96 hours under excess weight as specified in a standard test procedure. Afterwards, the samples were tested in a *CBR* machine by penetrating a plunger in soil samples

at the specified rate stipulated in ASTM-D1883 [22]. All the experimentation was performed in the Geotechnical Engineering Laboratory of Civil Engineering Department, University of Engineering and Technology, Lahore, Pakistan.

A summary of the results based on the above-mentioned tests is shown in Table 2. The outcomes of the laboratory tests were analyzed using multiple linear regression analysis to develop prediction models for the estimation of the California Bearing Ratio (*CBR*) and the compaction characteristics. A statistical package for the social sciences (SPSS) software was utilized to perform multiple linear regression analysis. Before starting the analysis process, data was divided into two categories, i.e., the input and the output parameters. For predicting the *CBR* value, the *CBR* value was considered as an output parameter and parameters like D_{30}, D_{50}, D_{60}, C_u, *MDD* and *OMC* were considered as probable input parameters. For predicting the compaction characteristics, *OMC* and *MDD* were the output parameters, whereas D_{30}, D_{50}, D_{60} and C_u were possible input parameters. The potential input parameters for the prediction of the *CBR* value and the compaction characteristics were identified as D_{30}, D_{50} and C_u, on the basis of passing t-test, while the rest of the parameters were neglected. The formulated correlations were calibrated using simple linear regression analysis by having a plot between the experimental and the predicted results.

The developed prediction models are validated using an independent database, which was not used in the development of the models. A correlation coefficient, a standard error of estimates and a relative error of estimates for every prediction model were examined to check the reliability of the developed models.

3 RESULTS AND DISCUSSIONS

The laboratory test results and the classification group based on the USCS and AASHTO classification system of the tested soil samples are summarized in Table 2.

Table 2. Test data used for the development of the predictive models.

Sr. No.	D_{10} mm	D_{30} mm	D_{50} mm	D_{60} mm	C_u	C_c	G_s	*OMC* %	*MDD* kN/m^3	*CBR* %	USCS Classification	AASHTO Classification
S1	0.10	0.18	0.25	0.36	3.79	0.95	2.67	15.4	18.4	13	SP	A-3
S2	0.13	0.18	0.25	0.30	2.31	0.83	2.70	13.1	17.6	10	SP	A-3
S3	0.11	0.19	0.24	0.32	2.91	1.03	2.66	12.2	18.6	13	SP-SM	A-3
S4	0.30	1.00	2.20	2.40	8.00	1.39	2.72	8.2	21.9	24	SW	A-1-b
S5	0.28	0.90	2.30	2.40	8.57	1.21	2.65	8.2	21.9	34	SW	A-1-b
S6	0.21	0.48	0.74	0.90	6.00	1.22	2.60	12.0	20.0	21	SW	A-1-b
S7	0.19	0.28	0.50	0.58	3.05	0.71	2.63	11.6	20.0	16	SP	A-1-b
S8	0.17	0.27	0.45	0.60	3.53	0.71	2.71	12.4	20.1	14	SP	A-1-b
S9	0.12	0.22	0.36	0.47	3.92	0.86	2.69	11.1	18.1	8	SP	A-3
S10	0.17	0.30	0.73	1.30	7.65	0.41	2.72	11.2	20.3	20	SP	A-1-b
S11	0.16	0.21	0.28	0.33	2.06	0.84	2.64	13.4	19.4	7	SP	A-3
S12	0.15	0.20	0.27	0.45	3.00	0.59	2.70	14.8	19.2	13	SP	A-3
S13	0.15	0.21	0.25	0.32	2.13	0.88	2.65	14.0	19.3	11	SP	A-3
S14	0.16	0.21	0.28	0.32	1.97	0.88	2.60	13.5	19.2	12	SP	A-3
S15	0.16	0.20	0.27	0.31	4.50	0.82	2.63	12.3	19.3	12	SP	A-3
S16	0.14	0.19	0.26	0.29	2.07	0.89	2.71	13.1	19.5	7	SP	A-3
S17	0.12	0.19	0.22	0.27	4.20	1.06	2.72	12.0	19.0	14	SP-SM	A-3
S18	0.19	0.19	0.25	0.56	4.50	0.35	2.64	14.5	19.2	16	SP	A-3
S19	0.13	0.20	0.26	0.48	3.69	0.61	2.70	13.8	19.4	6	SP	A-3
S20	0.13	0.19	0.25	0.51	3.92	0.54	2.67	14.8	19.0	10	SP	A-3
S21	0.10	0.17	0.21	0.25	2.60	1.20	2.65	11.9	18.5	12	SP-SM	A-3
S22	0.12	0.18	0.23	0.27	2.35	1.04	2.60	13.7	18.6	12	SP-SM	A-3
S23	0.12	0.19	0.24	0.28	2.33	1.07	2.63	14.0	18.7	12	SP-SM	A-3
S24	0.13	0.20	0.25	0.30	2.27	0.99	2.71	13.8	18.8	12	SP	A-3
S25	0.13	0.19	0.25	0.30	2.31	0.93	2.65	12.9	18.9	14	SP	A-3
S26	0.16	0.22	0.33	0.43	2.74	0.73	2.61	11.6	19.4	12	SP	A-3
S27	0.16	0.25	0.30	0.52	3.25	0.75	2.68	12.4	18.7	6	SP	A-3

Sr. No.	D_{10} mm	D_{30} mm	D_{50} mm	D_{60} mm	C_u	C_c	G_s	*OMC* %	*MDD* kN/m^3	*CBR* %	USCS Classification	AASHTO Classification
S28	0.16	0.23	0.40	0.45	2.90	0.76	2.72	12.5	19.0	10	SP	A-3
S29	0.17	0.19	0.88	1.00	5.88	0.20	2.65	12.8	19.8	18	SP	A-3
S30	0.17	0.18	0.20	0.53	3.12	0.36	2.60	13.2	19.7	9	SP	A-3
S31	0.13	0.17	0.22	0.25	1.92	0.89	2.63	13.7	17.8	11	SP	A-3
S32	0.17	0.19	0.92	1.20	7.06	0.18	2.70	11.7	20.5	20	SP	A-3
S33	0.14	0.19	0.22	0.27	7.96	1.01	2.63	13.5	18.4	12	SW	A-3
S34	0.23	0.41	0.53	0.73	3.17	1.00	2.71	11.3	20.2	8	SP-SM	A-1-b
S35	0.18	0.44	1.50	1.70	9.71	0.65	2.69	9.7	21.2	24	SP	A-1-b
S36	0.16	0.20	0.75	0.80	5.00	0.30	2.72	13.0	18.9	9	SP	A-3
S37	0.15	0.20	0.26	0.30	2.07	0.92	2.64	11.8	19.1	8	SP	A-3
S38	0.16	0.21	0.90	1.20	7.50	0.22	2.65	11.6	19.4	14	SP	A-3
S39	0.17	0.22	1.20	1.40	8.48	0.21	2.60	11.2	19.6	17	SP	A-3
S40	0.15	0.22	0.70	1.00	6.67	0.32	2.63	11.6	18.9	9	SP	A-3
S41	0.17	0.25	1.00	1.30	7.65	0.28	2.71	10.0	21.2	19	SP	A-3
S42	0.18	0.27	1.40	1.70	9.71	0.25	2.63	10.1	20.4	21	SP	A-3
S43	0.17	0.26	1.00	1.55	9.39	0.26	2.71	11.8	20.1	19	SP	A-3
S44	0.23	0.30	0.56	0.76	3.30	0.51	2.69	10.3	20.8	10	SP	A-1-b
S45	0.16	0.20	0.24	0.27	1.69	0.88	2.70	13.6	18.3	9	SP	A-3
S46	0.17	0.20	0.80	1.10	6.47	0.20	2.63	14.6	18.5	13	SP	A-3
S47	0.18	0.21	0.60	0.67	6.50	0.38	2.71	11.2	20.5	20	SP	A-3
S48	0.16	0.22	0.30	0.37	2.31	0.82	2.69	11.2	19.0	13	SP	A-3
S49	0.18	0.26	1.30	1.50	8.33	0.25	2.72	11.4	20.2	18	SP	A-3
S50	0.18	0.30	0.54	0.71	3.94	0.70	2.64	11.2	20.4	12	SP	A-1-b
S51	0.19	0.47	1.10	1.20	6.32	0.97	2.68	12.0	20.5	21	SP	A-1-b
S52	0.20	0.50	0.90	1.30	6.50	0.96	2.63	11.0	20.8	20	SP	A-1-b
S53	0.22	0.55	1.00	1.50	6.82	0.92	2.71	11.0	21.4	21	SP	A-1-b
S54	0.21	0.57	1.30	1.70	8.10	0.91	2.69	9.2	21.0	29	SP	A-1-b
S55	0.22	0.60	1.30	1.85	8.41	0.88	2.72	9.0	21.2	28	SP	A-1-b
S56	0.28	0.88	1.40	1.80	6.43	1.54	2.64	9.3	21.6	24	SW	A-1-b
S57	0.27	0.83	1.90	2.10	9.00	1.21	2.60	8.9	21.7	29	SW	A-1-b
S58	0.33	1.10	2.20	2.60	7.88	1.41	2.63	8.2	21.0	34	SW	A-1-b
S59	0.32	0.90	2.10	2.70	8.44	0.94	2.71	8.3	21.5	33	SP	A-1-b
S60	0.30	1.00	2.20	2.80	9.33	1.19	2.68	8.1	21.9	35	SW	A-1-b
S61	0.10	0.14	1.10	1.50	5.00	0.13	2.63	11.5	19.0	20	SP	A-3
S62	0.17	0.12	1.60	2.40	4.12	0.04	2.70	11.0	18.5	27	SP	A-1-b
S63	0.90	1.20	1.70	1.90	2.11	0.84	2.63	11.0	19.2	32	SP	A-3
S64	0.07	0.11	1.50	1.80	5.71	0.10	2.71	11.0	19.6	33	SP	A-3
S65	0.60	0.90	1.20	1.30	2.17	1.04	2.69	9.5	20.9	22	SP-SM	A-3
S66	0.60	0.90	1.20	1.50	2.50	0.90	2.72	7.5	21.4	23	SP	A-3
S67	0.40	0.60	2.20	2.50	6.25	0.36	2.64	6.5	21.6	32	SP	A-1-b
S68	0.90	1.60	2.00	2.40	2.67	1.19	2.65	9.5	19.5	26	SP-SM	A-1-b
S69	0.10	0.40	0.70	0.90	9.00	1.78	2.60	9.5	18.7	24	SW	A-3
S70	0.70	1.10	1.40	1.60	7.29	1.08	2.63	7.5	20.7	32	SW	A-1-b

Based on the grain size analysis, it can be inferred that the samples used in the study contain a sand content (percent passing 4.75 mm, and percent retained on 0.075 mm) varying between 80 and 100 %. The gravel content (percent retained on 4.75 mm) in the samples varies from 0 to 20% and the fines (percent finer than 0.075 mm) vary from 0 to 7%. The mean grain size (D_{50}) of all the samples is in the range 0.2 mm to 2.3 mm and the effective grain size (D_{10}) is in the range 0.45 mm to 0.07 mm. The particle sizes at 30% and 60% passing (D_{30} and D_{60}) were also determined from the grain size analysis curve. The coefficient of uniformity ($C_u = D_{60}/D_{30}$) of

the tested samples ranges from 1.7 to 9.7 and the coefficient of curvature (C_c=D_{30}^2/D_{60}×D_{10}) varies in between 0.04 and 1.78. The specific gravity of the samples is in the range 2.60–2.72. The results of the modified Proctor and *CBR* tests presented in Table 2 indicated that the maximum dry density (*MDD*) ranges from 17.64kN/m^3 to 21.92kN/m^3 and the optimum moisture content (*OMC*) ranges from 6.5% to 15.4% and the *CBR* values vary from 6 to 35.

More specifically, the *MDD* for the SP samples varies from 17.64kN/m^3 to 21.6kN/m^3, while for the SP-SM samples it fall between 18.45kN/m^3 and 20.89kN/m^3 and for the SW samples it varies from 18.37kN/m^3 to 21.92kN/m^3. The *OMC* for the SP samples varies from 6.5% to 15.4%, while for the SP-SM samples it falls between 9.50% and 14%,and for SW samples it varies from 7.5% to 13.5%. Similarly, the *CBR* for the SP samples varies from 6% to 33%, while for the SP-SM samples it falls between 8% and 26%, and for the SW samples it varies from 12% to 35%.

The laboratory test results mentioned in Table 2 were analyzed using multiple linear regression analysis to develop prediction models for the estimation of the California Bearing Ratio (*CBR*) and the compaction characteristics. A statistical package for the social sciences (SPSS) software was utilized to perform multiple linear regression analysis. The best-fit prediction models obtained as a result of the regression analysis carried out on the test data presented in Table 2 are as follows:

$$CBR = 6.508D_{50} + 1.48C_u + 3.970 \quad (R^2 = 0.85) \quad (11)$$

$$MDD = 0.171C_u + 2.408D_{30} + 18.168 \quad (R^2 = 0.81) \quad (12)$$

$$OMC = 0.026C_u - 2.53D_{50} + 13.456 \quad (R^2 = 0.74) \quad (13)$$

D_{50} and D_{30} are the grain sizes corresponding to 50% finer and 30% finer, respectively and D_{50} and D_{30} are in mm for the above-mentioned equations.

The coefficient of determination is a quantitative measure to represent how well the predicted results are replicated by the model. The standard error of estimate (SEE) is a quantitative measure to check the variance between the predicted and the experimental results. The relative standard error of the estimate is obtained by dividing SEE by the mean of the output values to provide a standard measure of fit. The formulated correlations in the present research have high values for the coefficient of determination (R^2) and relatively low values for the standard error of the estimate (SEE) and the relative standard error of the estimate. The SEE was computed mathematically;

$$SEE = \sqrt{\frac{\sum\left(y_{experimental} - y_{predicted}\right)^2}{v}} \quad (14)$$

where

v = Degree of freedom = number observations - number of variables
$y_{experimental}$ = Experimental results
$y_{predicted}$ = Predicted results

The SEEs for Eqs.(11), (12) and (13) are 3.13, 0.49 and 0.93, respectively. The SEE values indicate that the proposed models have a good prediction capability.

Analysis of variance (ANOVA) is carried out to determine the F- statistic for the output parameters and the t-statistics for input parameters for Eqs. (11), (12) and (13). The model F value for Eq.(11) is 147.7,for Eq.(12) is 105.63 and for Eq.(13) is 69.35. These values of the F- statistic are greater than the critical F, indicating that Eq.(11), (12) and (13) are significant. Similarly, absolute t- statistics for the input parameters for these equations are greater than the t- significance of the model.

Figures 1, 2 and 3 represent a comparison between the experimental and predicted results of *CBR*, *MDD* and *OMC* using equations (11), (12) and (13), respectively. These plots show that the variation between the experimental versus the predicted results for *CBR* are within ±4% confidence interval and within ±2% confidence interval for both the *MDD* and *OMC*.

The prediction models developed in this research were validated using an independent database. For this purpose, laboratory test results from 37 samples were utilized, which were not used in the development process of the models. The experimental results from the laboratory data were plotted against the predicted values using the proposed models, as represented in Figures1, 2 and 3, which show that the predicted results almost fall within the confidence interval of ±4% for *CBR* and±2% for both *MDD* and the *OMC*. The correlations proposed by NCHRP (National Co-operative Highway Research Program) [2], Ferede [5] and Saklecha et al. [7] were used for comparison purposes of the *CBR* value.

The predictions using the above-mentioned correlations are plotted in Figure 4. The predictions made by the NCHRP[2] correlation show that 7 out of 37 predictions fall outside ±4% confidence interval. The predictions made by Ferede's [5] correlation show that 10 out of 37 predictions fall outside ±4% confidence interval, and the predictions by Saklecha [7] correlation show that 11 out of 37 predictions fall outside ±4% confidence interval. The probable reason for this variation is the different

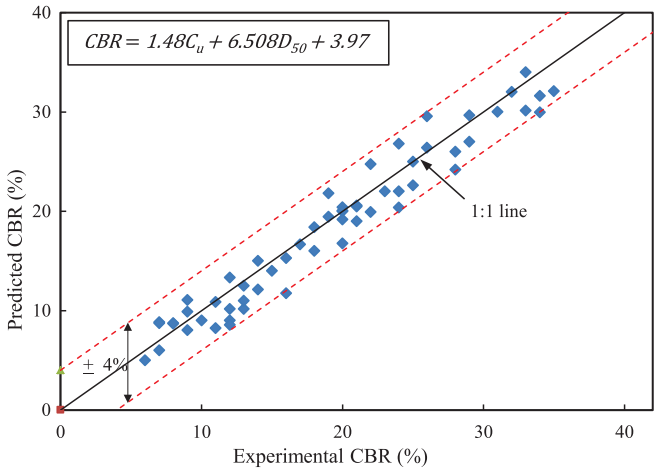

Figure 1. Experimental vs Predicted values of *CBR* by Eq. (11).

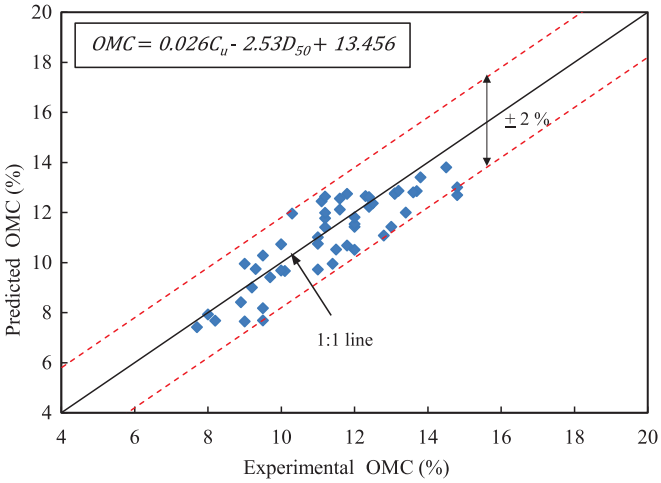

Figure 3. Experimental vs Predicted *OMC* by Eq. (13).

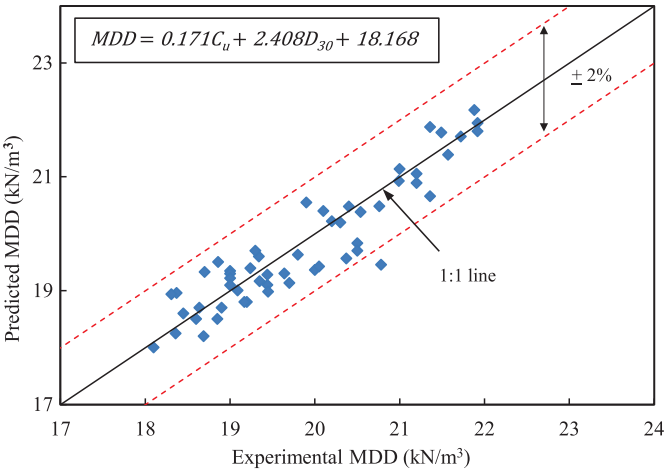

Figure 2. Experimental vs Predicted *MDD* by Eq. (12).

mineralogical composition, soil texture, fabric and deposition mode of the soils present in various regions of the world.

The correlations presented by Mujtaba et al. [13] and Omer et al.[14] were used for predicting the compaction characteristics using validation data. It can be observed from Figures 5 and 6 that the predicted results of the *MDD* and *OMC* fall almost within the ±2% envelopes, except for a few predicted results that exceed the prediction band of ±2%.

Figure 5 illustrates that the predictions by Eq. (3) show that 8 out of 37 predictions fall outside the ±2% confidence interval. Whereas the predictions by Eq. (1) show that 13 out of 37 predictions fall outside the ±2% confidence interval. The soil samples used in this

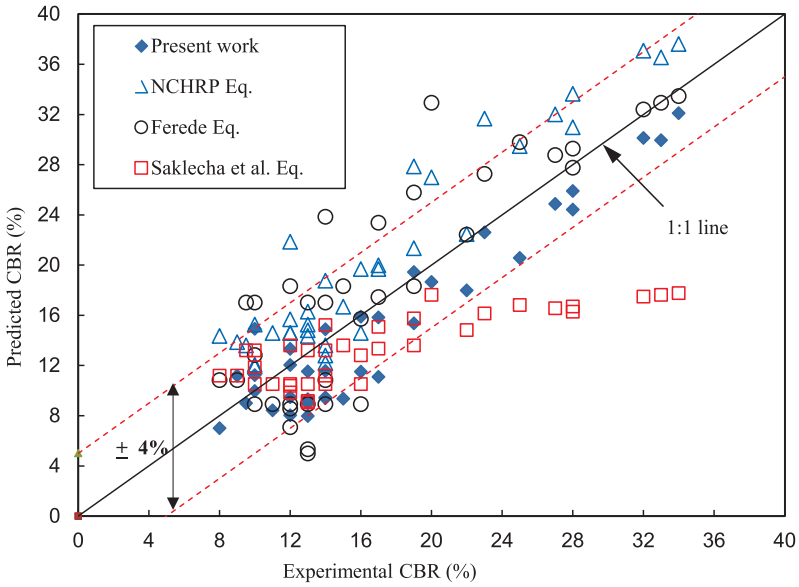

Figure 4. Experimental vs Predicted values of *CBR* by various models using the validation data.

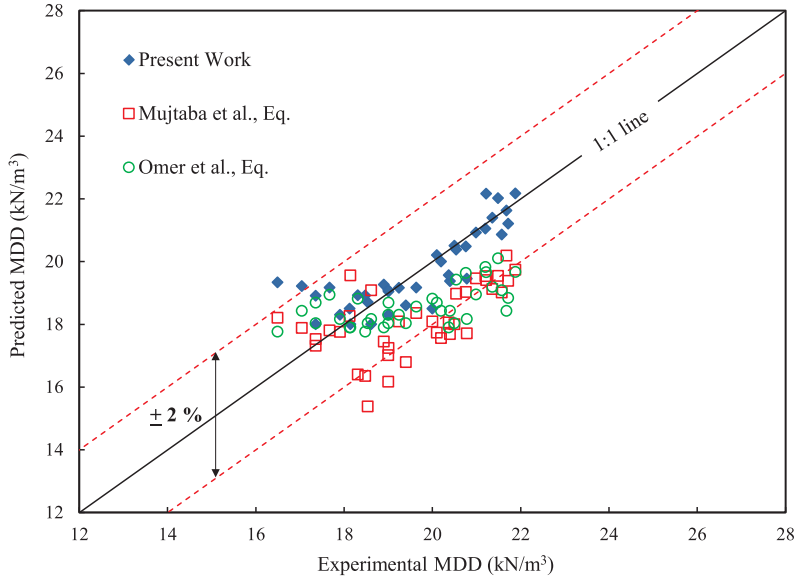

Figure 5. Experimental vs Predicted MDD by various predictive equations using validation data.

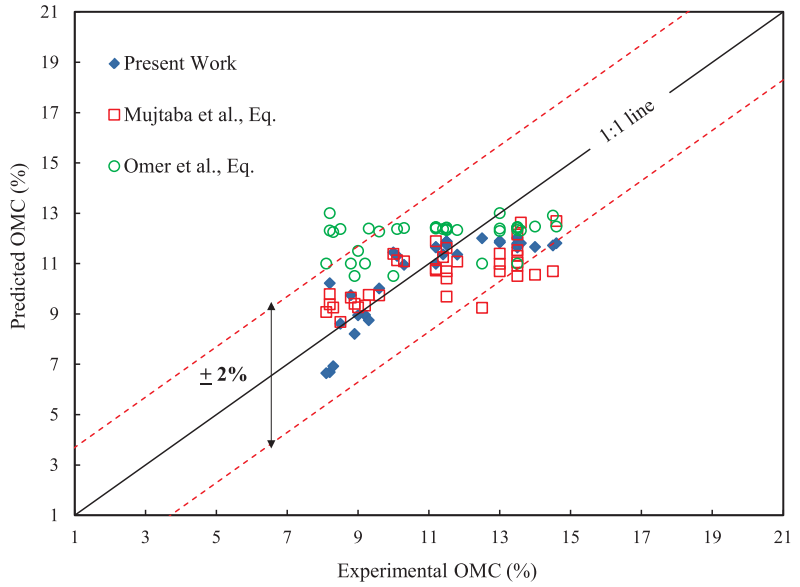

Figure 6. Experimental vs Predicted values of *OMC* by various models using the validation data.

research and those used by Mujtaba et al. [13] in his research were from same region, but the reason for this difference is the variation in the grain size distribution range of the soil samples used to develop these correlations. Mujtaba et al. [13] used 110 granular soil samples with a fine content varying from 0 to 47% and 70 samples of granular soil were used in this research with a fines content varying from 0 to 7%. So the difference in the fines content may be the cause of the variation in the predicted results, as illustrated in Figure 5.The predictions of the *OMC* by equations (2) and (4) show that only 4 and 6, respectively, out of 37 predictions fall outside the ±2% prediction band.

4 MODEL IMPLICATION

The *CBR* and the compaction parameters of granular soils depend on the number of physical soil parameters; however, based on extensive laboratory testing during this research, correlations have been proposed to predict

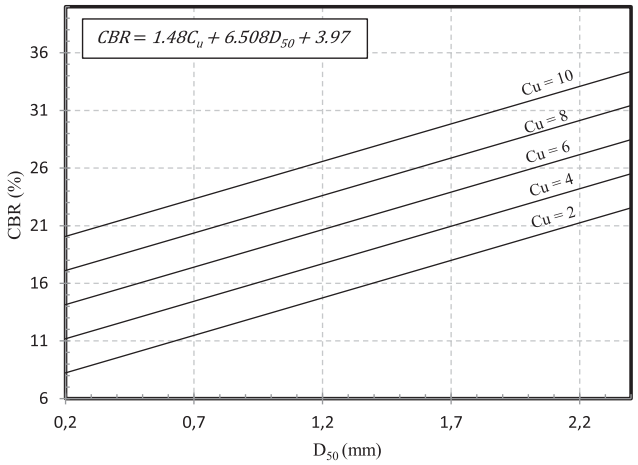

Figure 7. Nomograph for estimation of *CBR* value based on Eq. (11).

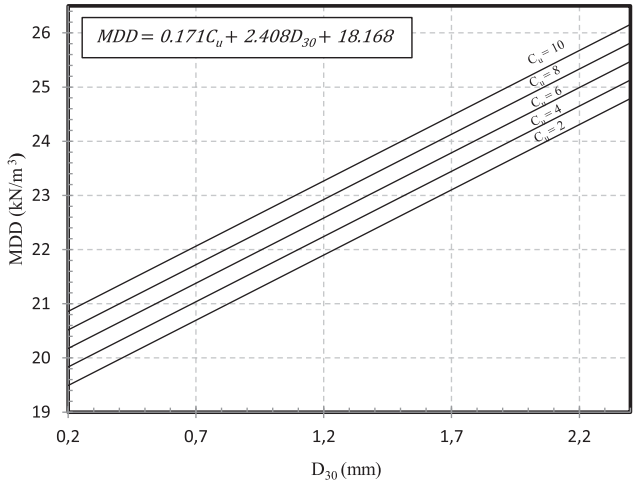

Figure 8. Nomograph for estimation of *MDD* value based on Eq. (12).

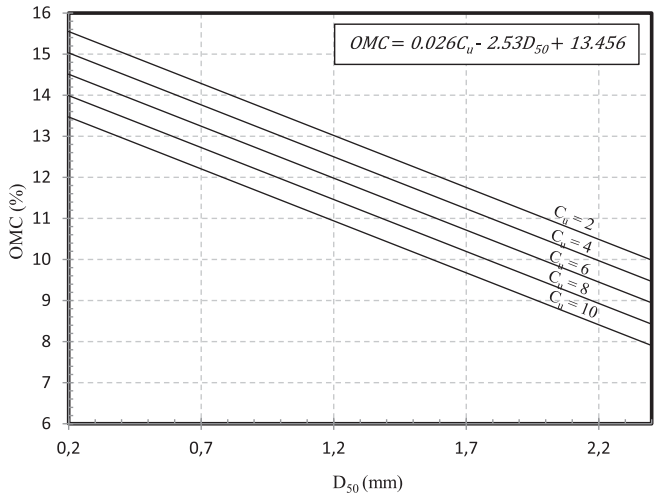

Figure 9. Nomograph for estimation of *OMC* value based on Eq. (13).

the *CBR* and the compaction characteristics of sandy soils with reasonable accuracy. These equations may be quite useful in estimating the engineering properties of granular soils used in the construction of earth structures. In addition, these models can be used during the planning and prefeasibility stages of the projects for a quick estimation of the *CBR* and the compaction parameters without performing any laboratory testing. In order to simplify the use of these correlations, nomographs or predictive curves have been developed based on the models presented in this research paper and the nomographs are presented in Figure 7 through Figure 9. By using these predictive curves, the *CBR*, *MDD* and *OMC* values of the granular soils can be readily estimated using the gradation data like D_{30} , D_{50} and C_u. Although the prediction models proposed in this article are quite valuable and user friendly, their use is applicable only for coarse-grained soils with a gravel content up to 20% and for non-plastic fines up to 10%.

5 CONCLUSIONS

On the basis of the above research study, the following conclusions can be drawn:

- The *CBR* value varies with the grain size parameters of coarse-grained soils; *CBR* varies from 6 to 35 when the mean grain size (D_{50}) varies from 0.2mm to 2.3mm and the coefficient of uniformity (C_u) varies from 1.7 to 9.7.
- Multiple linear regression analysis showed that the *CBR* values can be predicted based on mean grain size (D_{50}) and the coefficient of uniformity (C_u) using the correlation: CBR=6.508D_{50}+1.48C_u+3.970. The experimental versus predicted values fall within ±4%, indicating good prediction accuracy of the model.
- The *MDD* can also be predicted based on the coefficient of uniformity (C_u) and grain size corresponding to 30% passing (D_{30}) using the correlation: MDD=0.171C_u+2.408D_{30}+18.168.The prediction accuracy of this model is within ±2%.
- The optimum moisture content (*OMC*) is related to the coefficient of uniformity (C_u) and the mean grain size (D_{50}) as: OMC=0.026C_u-2.53D_{50}+13.456. The prediction accuracy of this correlation is also within ±2%.
- The predictive correlations and the curves presented in this research are valid for granular soils with a gravel content up to 20% and the fines up to 10% and above for non-plastic fines.

REFERENCES

[1] Agarwal, K.B., Ghanekar, K.D. 1970. Prediction of CBR values from plasticity characteristics of soil. In Processing of 2nd South East Asian Conference on Soil Engineering, Singapore, July 11-15.

[2] National Cooperative Highway Research Program (NCHRP). 2001. Correlation of *CBR* values with soil index properties. Guide For Mechanistic-Em*PI*rical Design of New and Rehabilitated Pavement Structures.

[3] Breytenbach, I.J., Green, P.P., Rooy, J.L.V. 2010. The relationship between index testing and California Bearing Ratio values for natural road construction materials in South Africa. Journal Of The South African Institution Of Civil Engineering 52, 2, 65–69.

[4] Roy, T.K., Chattopadhyay, B.C., Roy, S.K. 2009. Prediction of CBR from Compaction Characteristics of Cohesive Soil. Highway Research Journal, July-Dec, 77-88.

[5] Ferede, Z.W. 2012. Prediction of California Bearing Ratio (CBR) value from Index Properties of Soil., M.Sc. dissertation, Department Of Civil Engineering. Addis Ababa Institute of Technology (AAIT).

[6] Patel, R. S., Desai, M.D. 2010. CBR Predicted by Index Properties of Soil for Alluvial Soils of South Gujarat. Indian Geotechnical Conference, Proc. IGC 1, 79-82.

[7] Saklecha, P.P., Katpatal, Y.P., Rathore, S.S., Agarawal, D. K. 2011. Spatial Correlation of Mechanical Properties of Subgrade Soil for Foundation Characterization. International Journal of Computer Applications 36, 11. DOI: 10.5120/4544-6439

[8] Yıldırım, B., Gunaydın, O. 2011. Estimation of California bearing ratio by using soft computing systems. Expert Systems with Applications 38, 6381- 6391.

[9] Singh, D., Reddy, K.S., Yadu, L. 2011. Moisture and Compaction Based Statistical Model for Estimating *CBR* of Fine Grained Sub grade Soils. International Journal of Earth Sciences and Engineering 4, 6, 100-103.

[10] Taha, S.A., Ali, A. M. 2010. Determination of California Bearing Ratio Through Material Index Properties. Faculty of Engineering, Mansoura University, Mansoura, Egypt.

[11] Talukdar, D. K. 2014. A Study of Correlation between California Bearing Ratio (CBR) value with Other Properties of Soil. International Journal of Emerging Technology and Advanced Engineering 4, 1, 559-562.

[12] Sivrikaya, O., Kayadelen, C., Cecen, E. 2013. Prediction of the compaction parametersfor coarse-grained soils with finescontent by MLR and GEP. ACTA Geotechnica Slovenica 2, 29-41.

[13] Mujtaba, H., Farooq, K., Sivakugan, N., Das, B.M. 2013. Correlation between gradational parameters and compaction characteristics of sandy soils. International Journal of Geotechnical Engineering 7, 4, 395-401. DOI: 10.1179/1938636213Z.00000000045

[14] Omar, M., Shanableh, A., Basma, A., Barakat, S. 2003. Compaction characteristics of granular soils in United Arab Emirates. Geotechnical and Geological Engineering 21, 283-295. DOI: 10.1023/A:1024927719730

[15] Noor, S., Singh, A. 2012. Use of Genetic Programming to Evaluate Proctor Properties of Compacted Soils. International Journal of Latest Trends in Engineering and Technology 1, 4.

[16] Blotz, L., Bension, C., Boutwell, G. 1998. Estimating optimum water content and maximum dry unit weight for compacted soils. J. Geotech. Geoenvir. Eng. 124, 9, 907-912. DOI: http://dx.doi.org/10.1061/(ASCE)1090-0241(1998)124:9(907)

[17] Sridharan, A., Nagaraj, H. B. 2005. Plastic limit and compaction characteristics of fine grained soils. Ground Improvement 9, 1, 17-22. DOI: http://dx.doi.org/10.1680/grim.2005.9.1.17

[18] ASTM D-2487. 2007. Standard practice for classification of soils for engineering purposes (Unified Soil Classification System). ASTM International. DOI: 10.1520/D2487-11

[19] ASTM D-3282. 2007. Standard Practice for Classification of Soils and Soil-Aggregate Mixtures for Highway Construction Purposes. ASTM International. DOI: 10.1520/D3282-15

[20] ASTM D-422. 2007. Standard test method for particle-size analysis of soils. ASTM International. DOI: 10.1520/D0422-63R07E02

[21] ASTM D-1557. 2007. Standard test methods for laboratory compaction characteristics of soil using modified effort. ASTM International. DOI: 10.1520/D1557-07

[22] ASTM D-1883. 2007. Standard test methods for CBR (California bearing ratio) of laboratory compacted soils. ASTM International. DOI: 10.1520/D1883-16

NUMERIČNA ŠTUDIJA KOEFICIENTA DINAMIČNEGA AKTIVNEGA ZEMELJSKEGA TLAKA ZA KOHEZIVNE ZEMLJINE

Mehrab Jesmani
P.E., Koury Engineering & Testing Inc.
Chino, CA, ZDA
E-pošta: mehrabjesmani@gmail.com

Hossein Alirezanejad
Professional Geotechnical Engineer
Tehran, Iran
E-pošta: h.alirezanejad@gmail.com

Hamed Faghihi Kashani
HyGround Engineering LLC
Williamsburg, MA, ZDA
E-pošta: hamed@hyground.com

Mehrad Kamalzare *(vodilni avtor)*
California State Polytechnic University,
Department of Civil Engineering
3801 West Temple Ave. Pomona, CA 91768, ZDA
E-pošta: mkamalzare@cpp.edu

Ključne besede

koeficient dinamičnega aktivnega zemeljskega tlaka (K_{ae}), kohezivna zaledna zemljina, metoda končnih diferenc (FDM), natezne razpoke, podporni zid, seizmična obtežba

Izvleček

Podporni zidovi so predlagani v mnogih projektih, kot so mostovi, priobalne konstrukcije, cestne konstrukcije in v primerih, ko je potrebno bočno podpiranje izkopov vertikalnih površin. Koeficient aktivnega zemeljskega tlaka K_a, predstavlja pomemben parameter pri študiju statičnega in dinamičnega obnašanja podpornih zidov. Mnoge študije obravnavajo ta koeficient v statičnih pogojih, v mnogih predhodnih dinamičnih študijah so raziskovalci obravnavali obnašanje nekohezivne zaledne zemljine ali pa so naredili poenostavljene predpostavke za kohezivne zaledne zemljine (npr.: psevdo statični pogoji). V tej študiji je bila preučevana vrednost koeficienta aktivnega zemeljskega tlaka (K_a) v polni dinamični situaciji (K_{ae}). Podporni zid s kohezivno zaledno zemljino je preučevan z uporabo metode končnih diferenc (FDM), upoštevani so vplivi pomembnih lastnosti zemljine in obtežb. Model je zasnovan z Mohr-Coulomb modelom kriterija porušitve pri seizmični obtežbi. Rezultati kažejo, da je vrednost koeficienta K_{ae} na vrhu zidu, kjer je zelo občutljiv na kakršno koli spremembo lastnosti zemljine in obtežbe, večja od vrednosti koeficienta K_{ae} zaradi visoke vrednosti tlaka povzročenega s horizontalnim dinamičnim pospeškom in prisotnostjo nateznih razpok.

NUMERICAL STUDY OF THE DYNAMIC ACTIVE LATERAL EARTH PRESSURE COEFFICIENT OF COHESIVE SOILS

Mehrab Jesmani
P.E., Koury Engineering & Testing Inc.
Chino, CA, USA
E-mail: mehrabjesmani@gmail.com

Hossein Alirezanejad
Professional Geotechnical Engineer
Tehran, Iran
E-mail: h.alirezanejad@gmail.com

Hamed Faghihi Kashani
HyGround Engineering LLC
Williamsburg, MA, USA
E-mail: hamed@hyground.com

Mehrad Kamalzare *(corresponding author)*
California State Polytechnic University,
Department of Civil Engineering
3801 West Temple Ave. Pomona, CA 91768, USA
E-mail: mkamalzare@cpp.edu

Keywords

Dynamic active lateral earth pressure coefficient (K_{ae}), cohesive backfill soil, finite difference method (FDM), tension cracks, retaining wall, seismic loading

Abstract

Retaining walls are proposed in many projects, such as bridges, coastal structures, road constructions and wherever lateral support is required for the vertical surface of an excavation. The active lateral pressure coefficient of soil, K_a, is an important parameter for studying the static and dynamic behaviors of these retaining walls. Many studies have evaluated this coefficient in static situations, but in most previous dynamic studies, researchers have worked on the behavior of cohesionless backfill soil or made simplifying assumptions (e.g., pseudo-static status) for cohesive soils as backfill soil. In this study, the size of the active lateral earth pressure coefficient (K_a) was studied in a full dynamic situation (K_{ae}). A retaining wall with cohesive backfill soil is evaluated using the finite-difference method (FDM) and the effects of important soil and loading properties are assessed. The model is based on Mohr-Coulomb failure criteria under seismic loading. The results show that the value of K_{ae} at the top of the wall, where it is highly sensitive to any variation in the soil and loading properties, is greater than one due to the high pressure value induced by the horizontal dynamic acceleration and the presence of tension cracks.

List of Symbols

K_a	The active lateral earth pressure coefficient of soil
K_{ae}	Dynamic Active Lateral Earth Pressure Coefficient
K_h	Horizontal seismic pseudo-static coefficient
K_v	Vertical acceleration coefficients of the seismic loading
B	Width of the wall foot
H	Height of the wall
G	Shear Modulus
c	Cohesion
i	Backfill Soil Angle

1 INTRODUCTION

The active lateral earth pressure coefficient of soil (Ka) has been the subject of intense interest and study for the design of retaining walls. Coulomb [1], as the first scientist to study the backfill soil pressure, assumed that the effective pressure that builds up behind a retaining wall is the result of the weight of a soil section above a certain linear sliding plane and used the limit equilibrium theory of forces (Fig. 1) to assign the active and passive pressures. The general equations developed through this theory are based on a number of fundamental assumptions as follows: the retained soil is cohesionless (no clay component), homogeneous (not a varying mixture of materials), isotropic (similar stress-strain properties

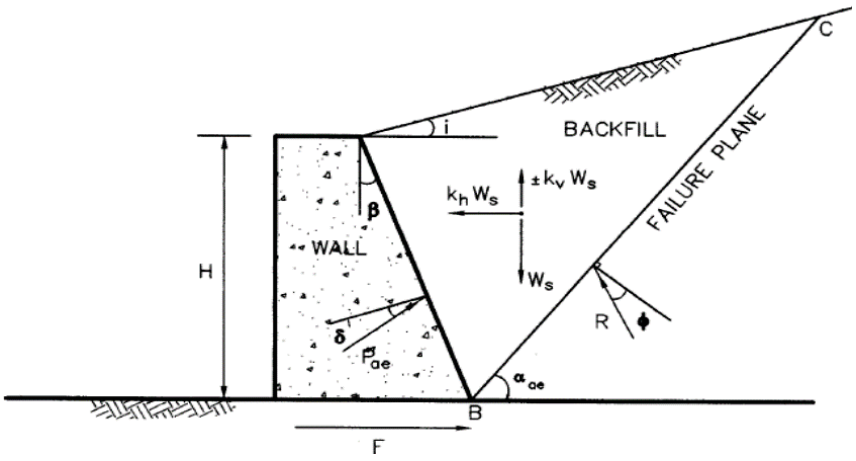

Figure 1. Limit equilibrium theory of retaining walls (Coulomb 1776, [1]).

in all directions or in practical terms, not reinforced), semi-infinite (the wall is very long and the soil moves back a long distance without bends or other boundary conditions), and well drained (to avoid a consideration of pore pressure). Accordingly, he suggested Eq. 1 for the static loading condition:

$$K_a = \frac{\cos^2(\varphi-\theta)}{\cos^2\theta\cos^2(\delta+\theta)\left[1+\sqrt{\frac{\sin(\delta+\varphi)\sin(\varphi-\beta)}{\cos(\delta+\theta)\cos(\theta-\beta)}}\right]^2} \quad (1)$$

where δ is the friction angle between the soil and the wall, φ is the internal friction angle and β and θ are as defined in Fig.1.

Rankine [2] suggested a stress-field solution to predict the active and passive earth pressures. His methodology relied on the assumptions that the soil is cohesionless, the wall is frictionless, the soil-wall interface is vertical, the failure surface on which the soil moves is planar and the resultant force is angled parallel to the backfill surface. He proposed Eq. 2 for determining K_a in the case when the backfill soil has a zero angle with respect to the horizon and Eq. 3 for the cases where the backfill soil has a non-zero angle to the horizon, both equations considering the static loading only:

$$K_a = \frac{1-\sin\varphi}{1+\sin\varphi} = \tan^2\left(\frac{\pi}{2}-\frac{\varphi}{2}\right) \quad (2)$$

$$K_a = \cos i\frac{\cos i-\sqrt{\cos^2 i-\cos^2\varphi}}{\cos i+\sqrt{\cos^2 i-\cos^2\varphi}} \quad (3)$$

where φ is the internal friction angle and i is the backfill soil angle with respect to the horizon.

Okabe [3] and Mononobe and Matuso [4] conducted pseudo-static analyses and suggested a relationship between K_a and some other parameters, as indicated in Eq. 4, known as the M-O equation. This equation, which can be considered as a development of Eq. 1 (Coulomb 1776), has been mainly used for the study of dry and non-cohesive soils under earthquake loading conditions.

$$K_{ae} = \frac{\cos^2(\varphi-\theta-\beta)}{\cos\theta\times\cos^2\beta\times\cos(\beta+\delta+\theta)\times D} \quad (4)$$

where φ is the internal friction angle, β is the internal steep of the wall, δ is the friction angle between the wall and the backfill soil and D and θ are as defined in Eq. 5 and Eq. 6 , respectively.

$$D = \left[1+\sqrt{\frac{\sin(\varphi+\delta)\sin(\varphi-\theta-i)}{\cos(\delta+\beta+\theta)\cos(i-\beta)}}\right]^2 \quad (5)$$

$$\theta = \tan^{-1}\left[\frac{k_h}{1-k_v}\right] \quad (6)$$

where i is the angle between the backfill soil and the horizontal (the slope of the soil face) and K_h and K_v are the horizontal and vertical acceleration coefficients of the seismic loading, respectively.

Saran and Prakash [5] developed the M-O equation (Eq. 4) for cohesive backfill soils, neglecting the earthquake vertical acceleration. Their model showed, however, the independence of the maximum pressure from the backfill soil weight over the failure plane, making the solution insecure from a practical viewpoint. Later, Zarrabi-Kashani [6] suggested an equation for assigning the angle of failure wedge in seismic loading conditions,

based on the M-O equation. Wood [7] examined the behavior of a solid retaining wall (without collapsing) under the active seismic pressure of the backfill soil using an elasto-plastic method. He stated that the resultant of the dynamic pressure is located at a point 0.6 times the wall height from the wall toe and the sliding plane has a curved shape. Steedman and Zeng [8] carried out a pseudo-static analysis to evaluate the behavior of retaining walls higher than 10 meters. In an attempt to address the deficiency of the pseudo-static analysis for evaluating the displacement of retaining walls under a seismic loading, Richards and Elms [9, 10] suggested a method to investigate the main ground motivating parameters caused by seismic loading (with maximum speed) to decrease the active seismic soil pressure based on the wall displacement.

Richards and Shi [11] presented an analytical solution for determining the lateral active pressure in cohesive soils, which was in fact a development of the elasto-plastic equation for cohesionless soils. They studied the effects of both horizontal and vertical accelerations. Velesos and Younan [12] reported that in solid walls that have elastic limitations in their foundation the magnitude and distribution of the backfill soil pressure are related to the limited flexibility of the foundation. Morisson and Ebeling [13] simulated the dynamic passive earth pressure by using a limited equilibrium computation with a logarithmic spiral failure surface. Soubra [14] assessed the passive earth pressure coefficients of rigid retaining structures in static and seismic loading conditions using an upper bound limit analysis. Chen [15] studied the problem of earthquake-induced lateral earth pressure using the LRFD method. Kumar [16] tried to determine the seismic passive earth pressure coefficient for sands. Kumar and Chitikela [17] employed the method of characteristics to evaluate the passive earth pressure coefficient in seismic loading conditions. Green and Ebeling [18] used the finite-difference method (FDM) (FLAC software) to evaluate the dynamic pressure on a retaining wall in dry consolidated sandy soils. They also drew an analogy between the lateral earth pressure coefficients (K_{ae}) obtained from FLAC software and the M-O equation, as shown in Fig. 2.

Saran and Gupta [19] continued the method of Saran and Prakash [5] in retaining walls having backfill soil with a slope in order to determine the lateral active pressure for cohesive soils. Cheng [20] studied the seismic lateral earth pressure coefficients for c-φ soils by employing the slip-line method. Yang and Yin [21] studied the seismic passive earth pressure by applying the limited analysis method with a non-linear failure criterion. Choudhury and Nimbalkar [22] investigated the temporal effects and shear phase changes of the primary waves behind the retaining walls by using a pseudo-dynamic method. Mylonakis et al. [23] proposed an alternative for the M-O equation for an evaluation of the seismic earth pressure on gravity walls with cohesionless backfill soil. Ghanbari and Ahmadabadi [24] brought forth two equations for perusing the inclined retaining walls backfilled by cohesionless and cohesive soils with a friction angle, via both static and pseudo-static methods. They declared that the active earth pressure in soils with friction and cohesion has a nonlinear distribution in the seismic loading condition.

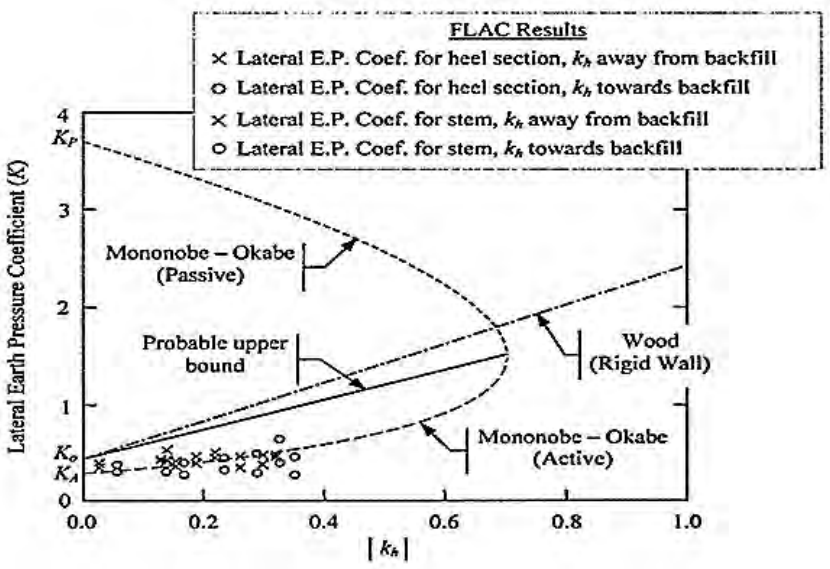

Figure 2. Comparison between lateral earth pressure coefficient (K_a) obtained from FLAC Software and M-O Equation [18].

Most of the above-mentioned works, with similarities in the standpoint through which the issue was looked at, namely, either assessing the cohesionless soils or using a pseudo-static method, shared basic assumptions on which ground their models were resting: a) negligible friction between the wall and the cohesive soil, b) single surface failure plane, c) adequate wall movement under the minimum active lateral pressure, d) using Mohr-Coulomb shear strength: $s = c + \sigma \tan\varphi$ (where s stands for the shear impedance, c for the cohesion, φ for the friction angle and σ for the effective stress of the backfill soil), e) backfill soil behaving like a solid material and f) the negligible effect of the tension cracks.

In this work, by considering the shortages felt in the context and with the aim of approaching a more realistic model, we studied the retaining walls with cohesive backfill soil under a full dynamic loading by means of a numerical model. What are the effects of the tension cracks, which in theory are supposed to increase the static active lateral pressure in the range 20 to 40% [25,26]. The results presented herein could be of great interest and avail in different sectors of geotechnical engineering, such as road construction, building construction and coastal structures in locations with cohesive soils.

2 DEFINITION OF NUMERICAL MODEL AND ASSUMPTIONS

The model retaining wall (B/H= 0.15, B: Width of the wall foot, H: Height of the wall) is made of concrete (Table 1) with the geometrical properties defined in Table 2. The wall is resting on a non-collapsing basic layer (elastic layer) and is facing a vertical surface of cohesive soil (Table 3) that is considered as a semi-infinite, homogenous and uniform environment. Since the length of the wall is a multiple of its height, the wall is modeled two dimensionally with the plane-strain condition and is subjected to a seismic loading on its unit length with constant acceleration and different ratios of k_v / k_h , i.e., 0, $1/3$ and $2/3$. To simulate the real condition that a wall would experience during an earthquake, the seismic load was applied as an acceleration, and at the same moment, to all of the nodes at the bottom of the model. Furthermore, for modeling the stress-strain behavior of the soil, the elasto-plastic model of the Mohr-Coulomb failure criteria was exploited.

Table 1. Concrete properties.

Bulk Modulus (K) $10^6 \times$ kPa	Poisson's Ratio (v)	Shear Modulus (G) $10^6 \times$ kPa	Unit weight (γ) kPa
13.9	0.2	10.4	25

Table 2. Geometrical properties of retaining walls and related parameters.

Height (H) m	Ratio of width to height (B/H)	Normalized depth by wall height (Z/H)	Backfill soil angle from horizontal (i°)
3,5,8	0.15	0–1	0,10,20,30,60

Table 3. Backfill soil properties of studied retaining walls (Poisson's ratios (v) for all soils are equal to 0.4).

Cohesion (c) kPa	Elasticity Modulus (E) kPa	Dry unit weight (γ_d) kN/m^3	Friction angle (φ°)
25	5000	16.5	5.15
45	12000	17.5	5.15
85	20000	18.5	5.15
100	27000	19.5	5.15

3 FINITE-DIFFERENCE MODEL STRATEGIES

A two-dimensional computational model is used under the plane-strain condition. Interface elements were used to model the shear stiffness, friction, cohesion, etc. for soil interfacing surfaces. Fig. 3 illustrates the interfacing elements for interfacing surfaces (soil to soil and soil to wall) of this study.

The interface elements are used to model the shear stiffness, friction, cohesion between two different surfaces. These elements are necessary to model and for simulating any probable separation, or the sliding of surfaces. However, the behavior of the soil-to-soil, or soil-to-concrete interfaces is a function of the internal friction angle, and therefore, the properties of the interface elements were defined in such a way as to account for this. The elements and their properties were applied to the model from the beginning and before analyzing the model.

Fig. 4 shows the interface element used in this research. In the figure, T is the tension strength, k_n is the vertical stiffness, k_s is the shear stiffness, and S is the shear strength.

In accordance with the node velocity, which is related to the amount of damping force, in order to avoid the problems of wrong element appropriation for damping (such as generated body forces in failure areas that could create some errors) and to avoid the allocation of a constant damping to every element, the nodal unbalanced force damping system was used in the model with a D (damping factor) value of 5%. Since dynamic analyses with unreal boundaries can cause a reflection of the waves in the computing area, individual dashpots have been used for the boundary nodes to absorb the body waves without any reflection.

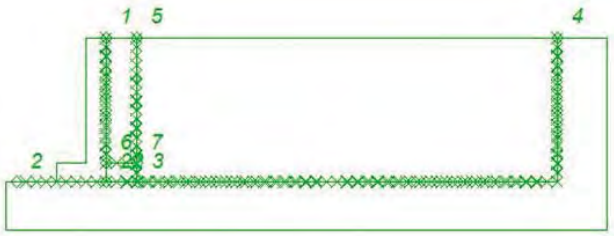

Figure 3. Interface elements of the wall-soil system in the model.

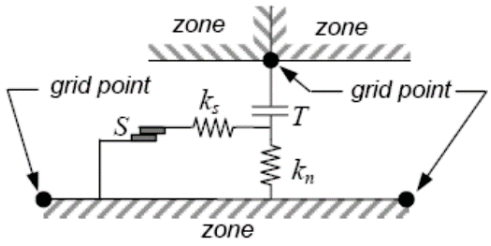

Figure 4. Interface element used in this study.

3.1 Meshing and loading condition

The meshes of the model for all the parts were squares with a dimension of 0.2 meter. In the static loading condition, the model was equilibrated with the materials weight. The lower nodes of the basic soil were restrained in the vertical and horizontal directions and it was assumed that the soil displacements do not affect the places beneath the defined nodes. Moreover, the nodes of the vertical boundaries were only restrained in the horizontal direction (Fig. 5).

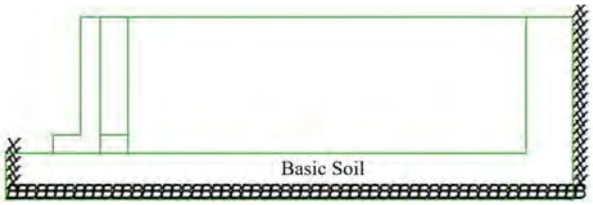

Figure 5. Model boundary condition in static loading.

In the dynamic loading condition, when the model is considered to be statically balanced, the dynamic load affects all the nodes of the base soil simultaneously (Fig. 6). In this situation, the displacement of the meshing nodes is taken to be equal to zero, in order to determine the net dynamic displacement after the loading. In addition, the wall was permitted to move, to develop an active condition and subsequently, the maximum value of K_{ae} experienced by the wall was recorded by the software as the dynamic active lateral pressure. The free

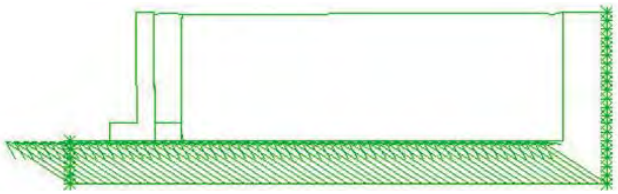

Figure 6. Load effect on all nodes of base soil layer with constant acceleration in dynamic loading.

Figure 7. Free field boundaries condition in dynamic loading.

fields of the model are taken as Fig. 7, which introduces the elements such that their masses are concentrated in nodes, and absorb the waves as free field boundaries.

4 MODEL VERIFICATION

In order to confirm the validity of the results achieved during the current study, a dry sandy soil with properties defined in Table 4 was modeled with the FDM (finite-difference method) analysis using FLAC. The results were compared with what the M-O equation predicts (as a proven equation confirmed and used by many experimental and numerical analyses). Interestingly, good agreement was found to exist between the two, from which results, a brief demonstration is presented in Fig. 8 (with K_h = 0.1~0.3, K_v = 0.1, c = 0 kPa and H = 3m). It is seen that with an increase in the internal friction angle, K_{ae} decreases. On the other hand, K_{ae} (dynamic active lateral earth pressure coefficient) increases when K_h increases (comparison of Fig. 8a, 8b and 8c). From the agreement found with the M-O equation and also from the logical trend of K_{ae} changes with the corresponding parameters, evaluated by this model, the validity of the FDM analysis can be ruled out.

Table 4. Granular soil properties used for the model verification.

ν	γ-- (kN/m^3)	c (kPa)	$\varphi°$	Tension resistance (T)	$\psi°$
0.3	15, 16.5, 18, 19.5, 20	0	25, 30, 35, 40, 45	0	0

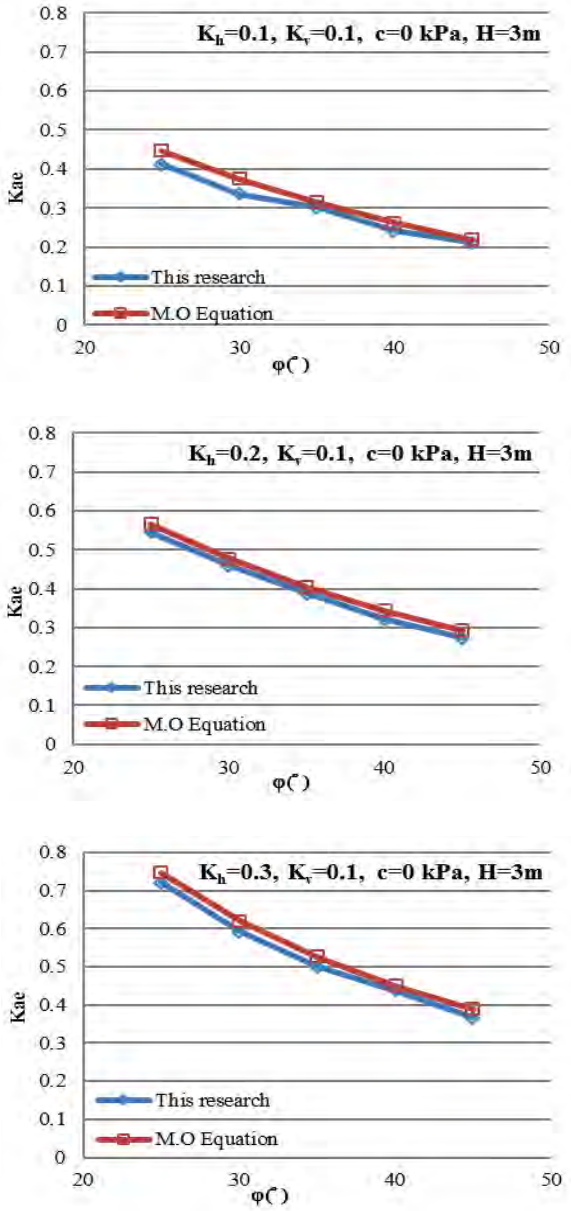

Figure 8. K_{ae} variation vs. φ for results obtained by numerical model of this research and M-O equation for constant K_v and different K_h coefficient.

5 RESULTS AND DISCUSSION

In this section, firstly, the effects of different parameters on K_{ae} are discussed in the two-dimensional condition and then, the parameters recognized as highly influential on K_{ae} are discussed in three-dimensional graphs with more details. Finally, some important "two-variable functions" will be proposed for the evaluation of the effective parameters.

5.1 Two-dimensional evaluation

5.1.1 Evaluation of dynamic active lateral earth pressure coefficient on the retaining wall

As seen in Fig. 9, in the dynamic loading condition the soil displacement at the top of the wall is more than that at the bottom and this difference is caused by the inconstant value of K_{ae} along the height. The lateral earth pressure at the top of the wall is affected by the backfill clayey soil tension cracks and at the bottom it is affected by the soil sliding caused by the upper soil layers' weight. At the top of the wall, K_{ae} is greater than 1 and it decreases gradually toward the depth.

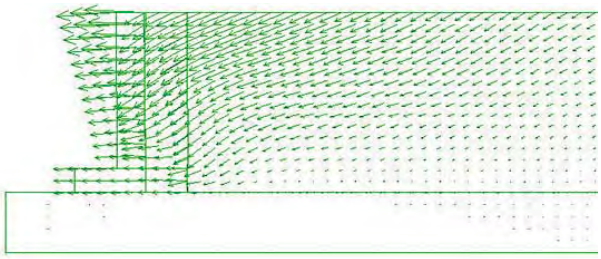

Figure 9. Displacement of the wall during seismic loading (φ = 15°, c = 45 kPa, K_v = 0.2 and, K_h = 0.3).

5.1.2 Effect of the soil depth on K_{ae}

The variation of K_{ae} with normalized depth by height (Z/H) for different cohesions and K_v/K_h ratios is shown in Fig. 10. It is apparent that K_{ae} decreases as the depth increases. This reduction appears sharply on the top of the wall and then slows down at the middle. At the bottom of the wall, K_{ae} starts increasing again; probably due to the soil sliding caused by the weight of the upper soil layers. Moreover, it is observed throughout Fig. 10 that for normalized depth (Z/H) values higher than approximately 0.16, Kae becomes less than 1 ($K_{ae} \leq 1$), for Z/H in the range of 0.25 to 0.75, K_{ae} remains almost constant and for Z/H larger than 0.75, K_{ae} starts increasing.

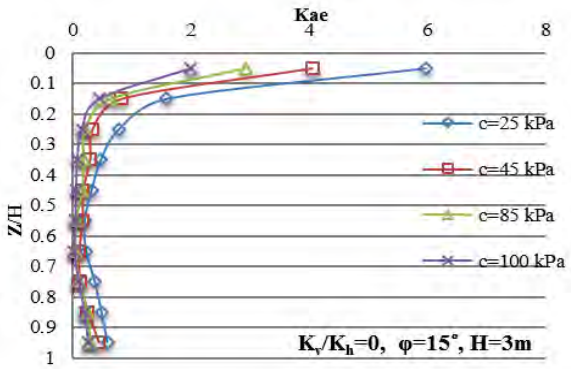

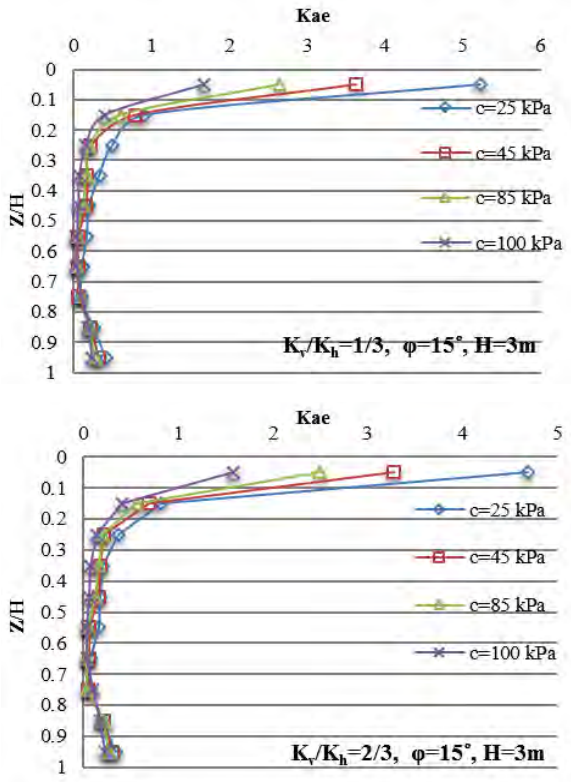

Figure 10. The variation of dynamic active lateral pressure coefficient (K_{ae}) vs. normalized depth Z/H for different cohesions and K_v/K_h ratios.

5.1.3 Effect of the soil cohesion on K_{ae}

As presented in Fig. 11, having a K_v/K_h ratio, a wall height (H), an internal friction angle ($\varphi°$) and a normalized depth (Z/H) constant, an increase in cohesion (c), will decrease K_{ae}. A reduction of the soil sliding and displacement as a result of the cohesion increase between the soil particles could be the reason for such behavior. In addition, it can be inferred from Figs. 10 and 11 that this effect decreases as the depth increases. Fig. 11 shows that at the top of the wall (Z/H = 0.05), increasing the soil cohesion (c) from 25 to 100 kPa, results in a decrease of about 45% in K_{ae}. Whereas, moving toward the middle of the wall (Z/H = 0.15, 0.35 & 0.65), the reduction rate decreases, indicating that the reduction of the cohesion is highly affected by the depth growth. Considering all the subsets of Figs. 10 and 11 demonstrates that for all cohesion values, Kae is larger than 1 in the first depth zone ($0 < Z/H < 0.1$) and that by increasing the cohesion, the dynamic active lateral pressure coefficient reaches 1 for lower Z/H ratios (lower depths). Therefore, it can be concluded that an increase in the soil cohesion decreases the depth of the tension cracks.

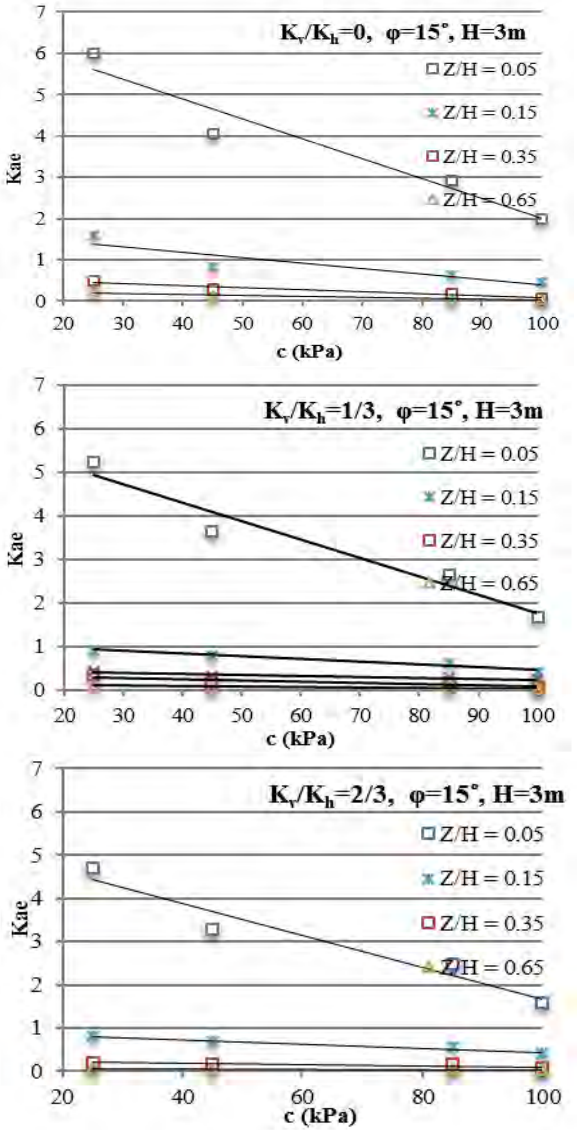

Figure 11. Variation of dynamic active lateral pressure coefficient (K_{ae}) vs. soil cohesion for different normalized depth Z/H and K_v/K_h ratios.

5.1.4 Effect of the K_v/K_h ratio on K_{ae}

As can be seen in Fig. 12, at constant cohesion (c), internal friction angle ($\varphi°$), height (H) and Z/H, a decrease in K_v/K_h ratio results in an increase of the dynamic active lateral pressure coefficient. Although this increase is not significant, it can be inferred that if the vertical acceleration of an earthquake decreases compared to its horizontal acceleration, the destructive effects of the seismic loading would increase. Besides, by increasing the soil cohesion or depth, the effect of the K_v/K_h ratio on K_{ae} becomes less significant (the slope decreases).

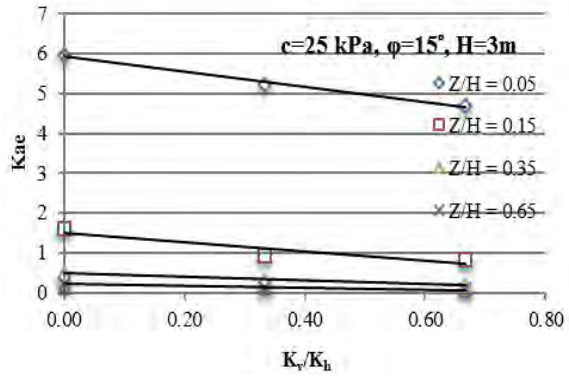

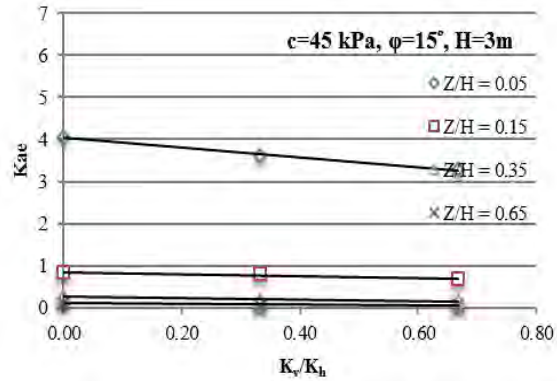

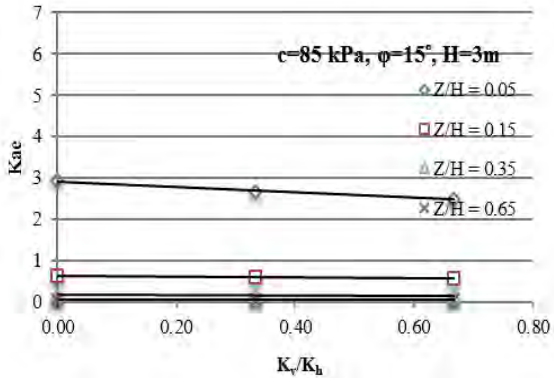

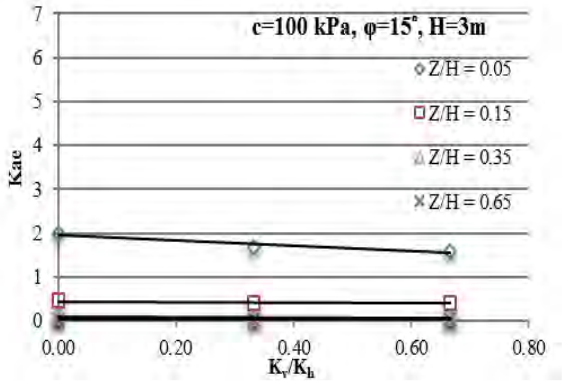

Figure 12. The variation of dynamic active lateral pressure coefficient (K_{ae}) vs. K_v/K_h ratios for different normalized depths Z/H and soil cohesions.

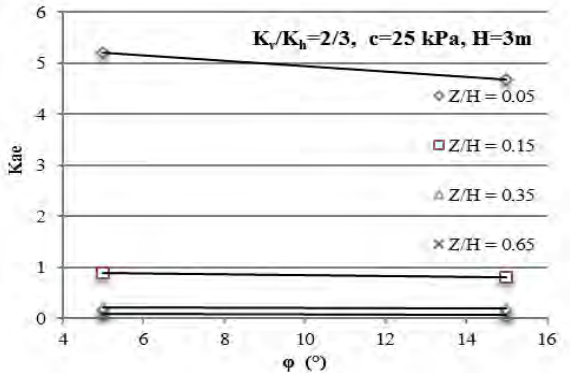

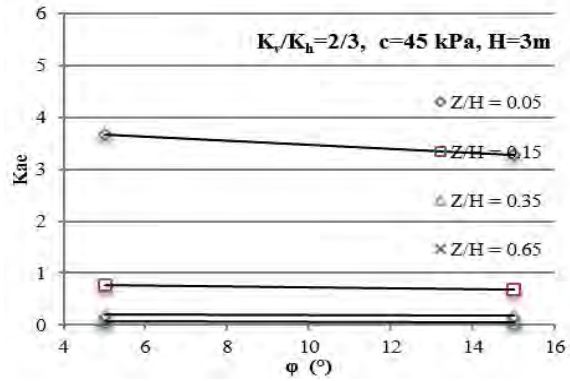

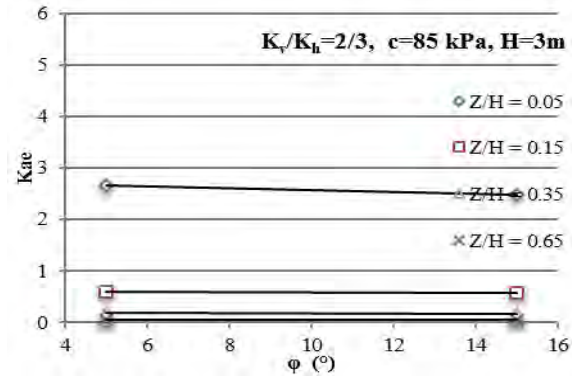

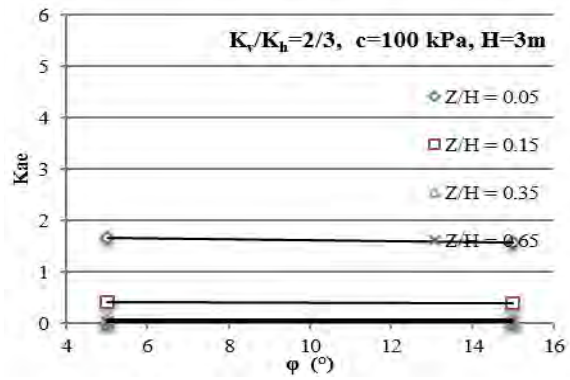

Figure 13. Variation of the dynamic active lateral pressure coefficient (K_{ae}) vs. soil friction angle $\phi°$ for different normalized depths Z/H and soil cohesions.

5.1.5 Effect of the internal friction angle (φ) on K_{ae}

Fig. 13 shows the variation of K_{ae} versus the friction angles (φ°) for different normalized depths (Z/H) and cohesions. It can be inferred that at a constant height (H), cohesion (c), K_v/K_h ratio and Z/H, a diminution in the value of the internal fiction angle from to results in an increases of about 10 to 15% in K_{ae} for lower cohesions (c = 25 and 45 kPa) and about 5 to 7% for higher cohesions (c = 85 and 100 kPa). Since the decreases of the φ can be simply translated to a looser and more collapsible nature of the soil, the likelihood of failing and sliding will obviously increase. Therefore, the dynamic active lateral pressure coefficient increases with a decrease of the friction angle and this effect becomes less significant with the soil cohesion growth and the depth increase.

5.1.6 Effect of the retaining wall height (H) on K_{ae}

Fig. 14 shows the effect of the wall height on K_{ae} in different normalized depths (Z/H) and soil cohesions. As can be seen, K_{ae} increases with the wall height, at constant internal friction angle (φ), cohesion (c), K_v/K_h and Z/H ratios. By increasing the wall height, the effect of the horizontal acceleration of the seismic loading increases at the top of the wall due to the longer moment arm. Moreover, increasing the wall height leads to an increased weight of the backfill soil. Therefore, the displacement at the bottom of the wall increases as a result of the higher elements weight of the backfill soil in comparison with a shorter wall. Fig. 14 also shows that increasing the wall height by 60–67% can induce an increase of about 10 to 38% for K_{ae} at the top of the wall (Z/H = 0.05). In addition, by moving toward the middle of the wall (Z/H = 0.15, 0.35 & 0.65) this incremental rate of K_{ae} decreases as a result of the wall's height increase. It is also obvious that by increasing the soil cohesion, the effect of H on K_{ae} decreases.

5.1.7 Effect of the horizontal acceleration of seismic loading (K_h) on K_{ae}

In order to investigate the effect of K_h on K_{ae}, two values for K_h (0.35 and 0.7) were chosen. As can be seen in Fig. 15 at a constant wall height (H), friction angle (φ), cohesion (c) and K_v, increasing K_h causes an increase of K_{ae} such that a direct relation highlights the destructive effects of the horizontal acceleration of the earthquake compared to its vertical acceleration. Obviously, increasing the horizontal force increases the sliding area of the backfill soil and this in turn leads to a higher value of the dynamic active lateral pressure. Fig. 15 also reveals that increasing the soil cohesion decreases the significance of the influence of K_h on K_{ae}. At the top of the wall (Z/H = 0.05, 0.15), a cohesion growth of 25 or 100 kPa can decrease the increase rate of K_{ae} versus K_h by 5 and 10%, respectively.

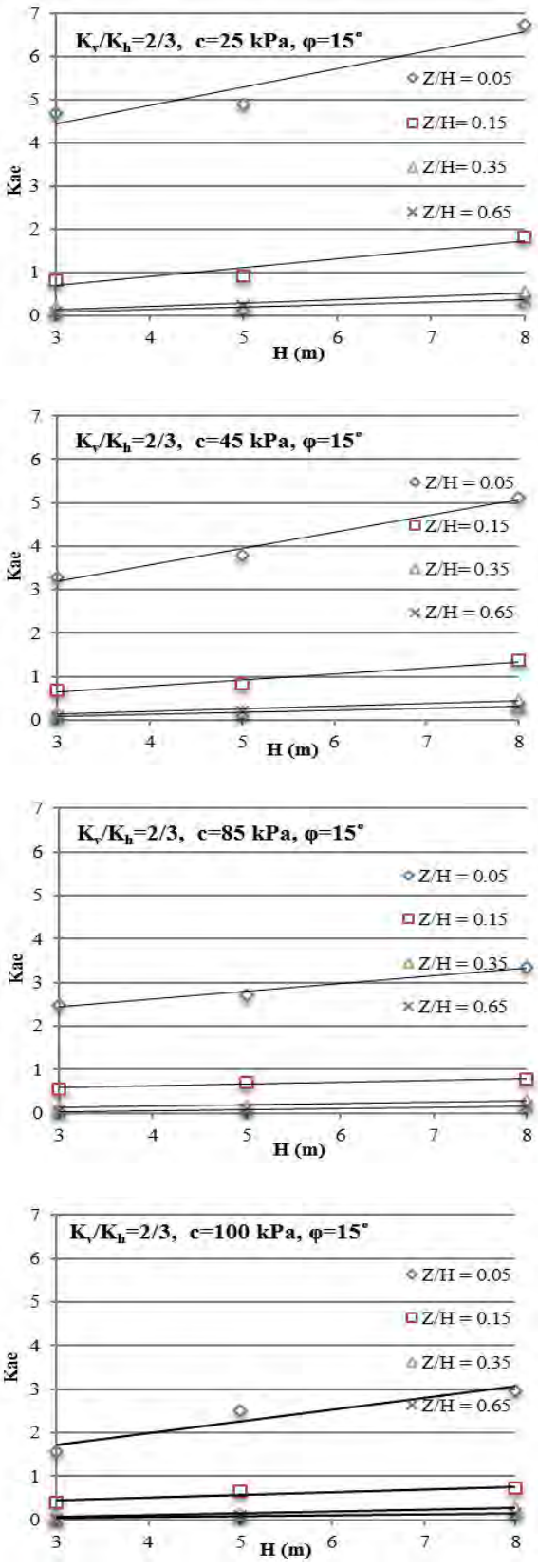

Figure 14. Variation of the dynamic active lateral pressure coefficient (K_{ae}) vs. wall heights (H) for different normalized depths Z/H and soil cohesions.

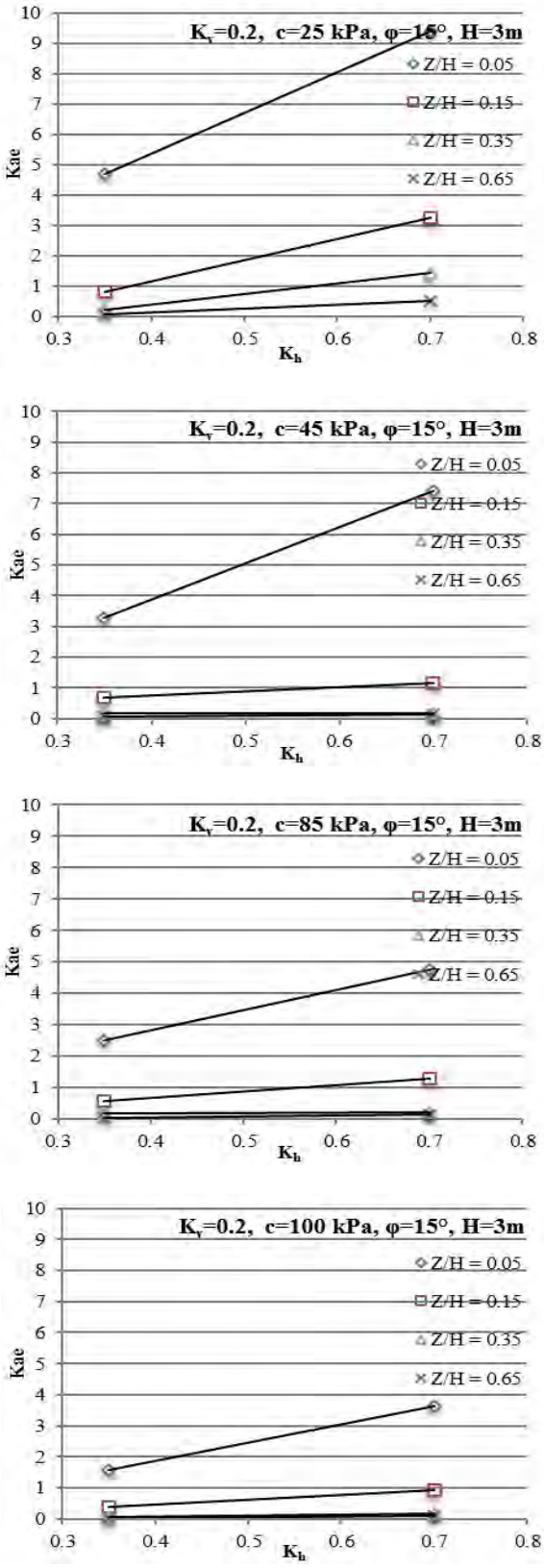

Figure 15. Variation of the dynamic active lateral pressure coefficient (K_{ae}) vs. horizontal acceleration coefficient (K_h) for different normalized depths Z/H and soil cohesions.

5.1.8 Effect of the backfill soil angle (i) on K_{ae}

Fig. 16 suggests that at constant K_v/K_h ratio, cohesion (c), friction angle (φ), height (H) and Z/H, an increase of the backfill soil angle with the horizon (i), makes K_{ae} increase almost linearly. It is clear that the horizontal

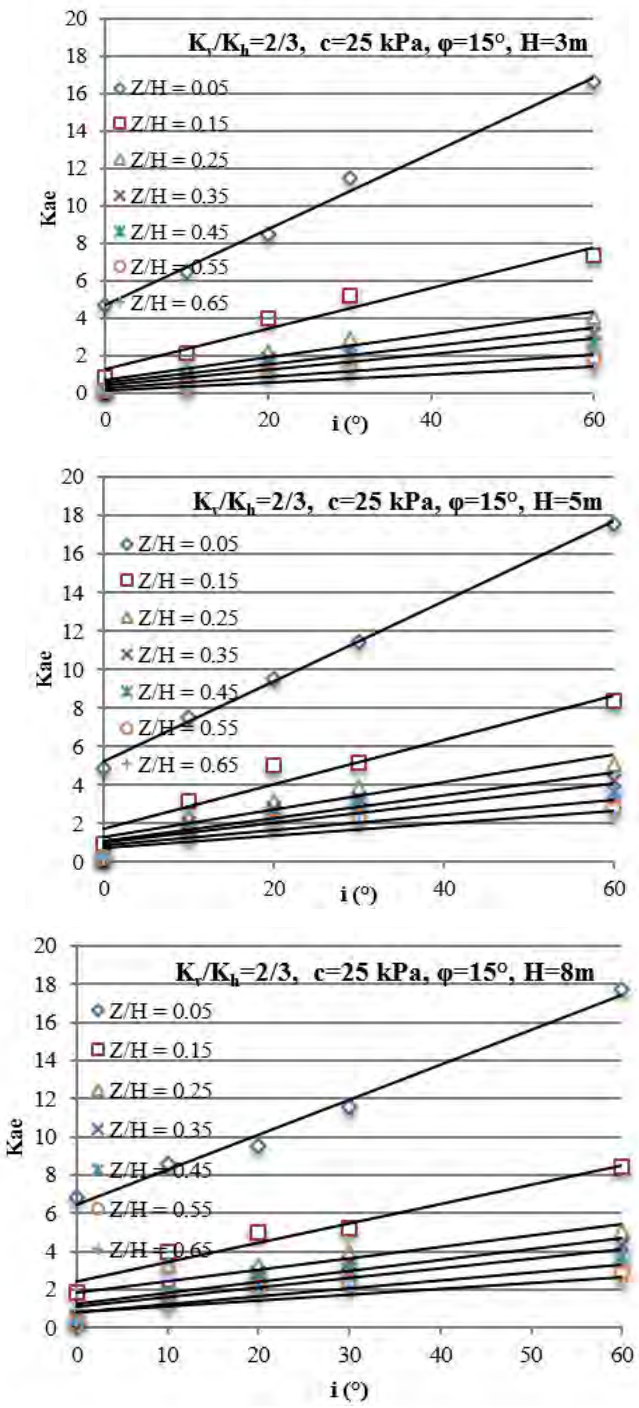

Figure 16. Variation of the dynamic active lateral pressure coefficient (K_{ae}) vs. backfill soil angles measured from horizontal (i) for different normalized depths Z/H ratios and wall heights (H).

acceleration component of the earthquake increases with the slope of the backfill soil and hence, increases K_{ae}. Fig. 16 also confirms that the effect of i on K_{ae} diminishes with the depth growth and the height of the wall does not have a significant effect on the variation of K_{ae} versus i. Moreover, in the upper section of the walls, for Z/H = 0.05 and 0.15, the variation of K_{ae} versus i is significant and the slope of this increment is approximately equal to 0.2 and 0.11 for all the walls, respectively. Accordingly, in the upper section of the wall, increasing the backfill soil angle from 0 to 60 degrees can increase K_{ae} linearly with the mentioned slope. Furthermore, going toward the depth, the effect of i on K_{ae} becomes negligible.

5.2 Three-dimensional graphs and two variable functions

In this section the effect of some critical parameters on K_{ae} is discussed, with the backfill soil surface being considered parallel to the ground surface (i = 0°), except in the section where i is a variable.

5.2.1 Effect of the K_v/K_h ratio and normalized depth (Z/H) on K_{ae}

Fig. 17 shows the effects of K_v/K_h and the normalized depth (Z/H) on K_{ae}, simultaneously. As can be seen clearly, for high depth ratios (K_v/K_h) the variation of K_v/K_h does not have a significant effect on K_{ae}. Whereas, for depth ratios less than about 0.15, K_{ae} becomes highly sensitive to K_v/K_h ratio variations with a potential increase possibility of up to a value of 6.

Eq. 7 is proposed to give an approximation for K_{ae} by certain values of K_v/K_h ratio and normalized depth (Z/H) (for depth ratios less than 0.75 and soil cohesion of 25 to 45 kPa);

$$K_{ae} = \frac{800}{\left[1+\left(\frac{\frac{k_v}{k_h}+3}{2.55}\right)^2\right]\left[1+\left(\frac{\frac{Z}{H}+0.04}{0.011}\right)^2\right]} \quad (7)$$

5.2.2 Effect of the ratio and soil cohesion on Kae

Fig. 18 is a combination of Fig. 11 and 12. As mentioned in the two-dimensional section, by increasing the K_v/K_h ratio and the soil cohesion, K_{ae} decreases. Fig. 18 clearly shows how the increase of the soil cohesion decreases the effect of the K_v/K_h ratio on K_{ae} variations. It is also apparent that for a low soil cohesion, K_{ae} is highly sensitive to a K_v/K_h ratio variation.

Considering the noticeable effect of the K_v/K_h ratio and the cohesion on K_{ae} in a two-dimensional study at the top of the wall, Eq. 8 is proposed to give an approximation for the active lateral earth pressure coefficient using certain values of the K_v/K_h ratio and the normalized soil cohesion (by 100 kPa) for depth ratios equal to and less than 0.05;

$$K_{ae} = \frac{680}{\left[1+\left(\frac{\frac{c(kPa)}{100}+3}{0.20}\right)^2\right]\left[1+\left(\frac{\frac{k_v}{k_h}+4}{2.6}\right)^2\right]} \quad (8)$$

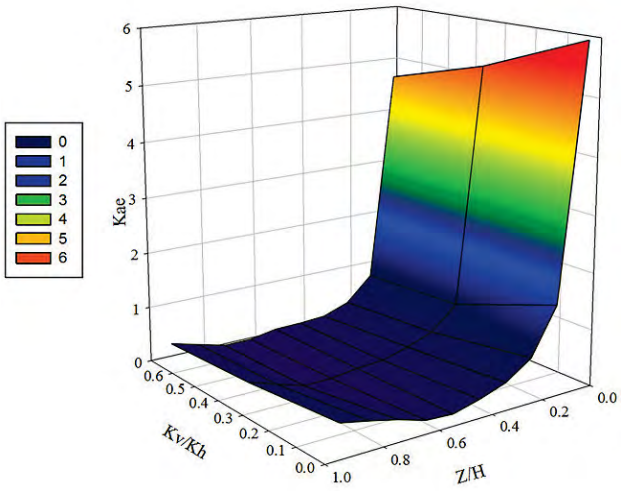

Figure 17. Variation of the dynamic active lateral pressure coefficient (K_{ae}) vs. K_v/K_h ratios and normalized depth Z/H in 3D perspective (i = 0°, φ = 15°, c = 25kPa).

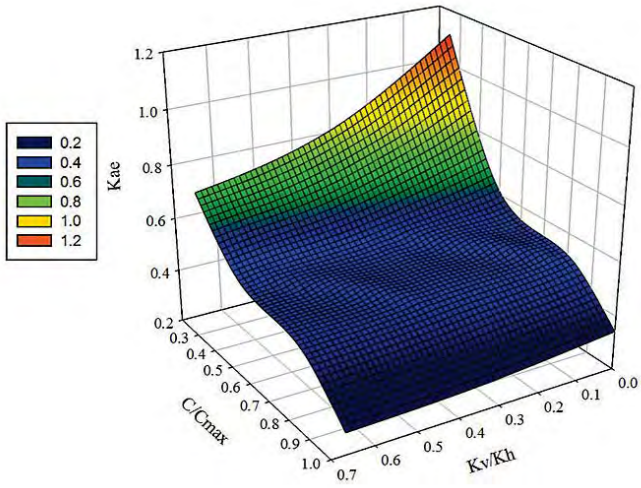

Figure 18. Variation of the dynamic active lateral pressure coefficient (K_{ae}) vs. K_v/K_h ratios and normalized soil cohesion c/c_{max} in 3D perspective (i = 0°, φ = 15°).

5.2.3 Effect of the normalized depth (*Z/H*) and the soil cohesion on K_{ae}

Fig. 19 shows the effect of the normalized soil cohesion and the depth ratio on K_{ae} It indicates that at high depth ratios the effect of the soil cohesion variation on K_{ae} is negligible. As discussed earlier in the two-dimensional section, the effect of soil cohesion on K_{ae} is significant at depth ratios of less than 0.15 (at the top the wall), with the possibility to increase K_{ae} up to a high value such as 5. This can be attributed to an increase of the tension cracks' depth due to the soil cohesion depression.

The 3D graph derived from the variations of K_{ae} versus the depth ratio and the normalized soil cohesion (by c_{max} = 100 kPa) shows a good fit to Eq. 9 for depth ratios (*Z/H*) less than 0.75 and K_v/K_h ratios between *1/3* and *2/3*;

$$K_{ae} = \frac{1675}{\left[\left[1+\left(\frac{\frac{Z}{H}+0.03}{0.015}\right)^2\right]\left[1+\left(\frac{\frac{c(kPa)}{100}+0.91}{0.36}\right)^2\right]\right]} \quad (9)$$

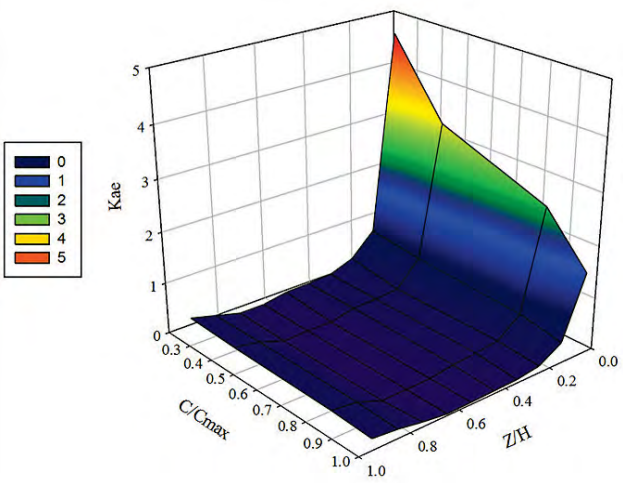

Figure 18. Variation of the dynamic active lateral pressure coefficient (K_{ae}) vs. normalized depth *Z*/*H* and normalized soil cohesion c/c_{max} in 3D perspective (i = 0°, φ = 15°).

6 CONCLUSION

The behavior of the retaining wall with cohesive backfill soil was evaluated using the finite-difference method (FDM), and the effects of different soil and loading properties on Kae were investigated. The following specific conclusions can be drawn:

1. The magnitude of K_{ae} for cohesive soils is larger than 1 at the top of the wall and becomes less than 1 at the middle and bottom of the wall.
2. Increasing the soil cohesion (c) in the range 25 to 100 kPa reduces K_{ae} by approximately 45% at the top of the wall (Z/H = 0.05) and by moving toward the bottom of the wall this reduction rate decreases.
3. By decreasing the K_v/K_h ratio, in the same zones of the wall height the effect of c on K_{ae} becomes more severe.
4. By decreasing the K_v/K_h ratio, the dynamic active lateral pressure coefficient increases insignificantly. Moreover, increasing the soil cohesion or depth makes this effect even more negligible.
5. With a reduction of the internal fiction angle from 15° to 5°, K_{ae} increases about by 10–15% at lower cohesions (c = 25 and 45 kPa) and around 5–7% at higher cohesions (c = 85 and 100 kPa).
6. Increasing the wall height by 60–70% can increase K_{ae} by about 10–38% at the top of the wall and by moving toward the middle of the wall this rate decreases.
7. By increasing the vertical acceleration relative to the horizontal acceleration in seismic loading (K_v/K_h ratio), the depth of tension cracks in backfill soil decreases.
8. By increasing the soil cohesion, the effect of K_h on variations of K_{ae} decreases. At the top of the wall (Z/H = 0.05, 0.15), a cohesion growth between 25 and 100 kPa can decrease the increscent rate of K_{ae} versus K_h between 5 and 10 percent.
9. By increasing the backfill soil angle with horizon (i), K_{ae} increases. The effect of i on K_{ae} decreases with the depth growth and the height of the wall does not have a significant effect on the variation of K_{ae} versus i.
10. K_{ae} is extremely sensitive to the variation of the soil and loading properties at the top of the wall (Z/H < 0.15).

Acknowledgement

The authors would like to show their gratitude to Koury Engineering & Testing, Inc. The authors also would like to thank Mr. Armin Jesmani for his hard work and help to provide the graphs, mathematical equations, and organizing the structure of this paper.

REFERENCES

[1] Coulomb, C.A. 1776. Essai sur une application des regles de maximia et minimis a quelques problemes de statique relatifs a l'architecture. Mem. Acad. Roy. Div. Sav. 7, 343-387.

[2] Rankine, W.M. J. 1857. On the Stability of Loose Earth. Philos Trans R Soc London, Part 1, pp. 9-27.
[3] Okabe, S. 1924. General theory of earth pressure and seismic stability of retaining wall and dam. Japan Soc. Civil Eng. 12, 1, 1277-1323.
[4] Mononobe, N., Matuso, H. 1929. On the determination of earth pressures during earthquakes. Proc. of the World Eng. Conf., Tokyo, Japan, 9, paper No. 388.
[5] Saran, S., Prakash, S. 1968. Dimensionless parameters for static and dynamic earth pressures behind retaining walls. Indian Geotech. J. 7, 3, 295 – 310.
[6] Zarrabi, K. 1973. Sliding of Gravity Retaining Wall During Earthquakes Considering Vertical Acceleration and Changing Inclination of Failure Surface. M.S. Thesis, Department of Civil Engineering MIT, Cambridge, MA.
[7] Wood, J. H. 1973. Earthquake-induced soil pressures on structures. Rep. EARL 73-05, Earthquake Engineering Research Laboratory, California Inst. Of Technol., Pasadena, California, pp. 175-186. DOI: 10.1061/(ASCE)GT.1943-5606.0000351
[8] Steedman, R.S., Zeng, X. 1990. The influence of phase on the calculation of pseudo-static earth pressure on a retaining wall. Geotechnique 40, 1, 103-112. DOI: 10.1680/geot.1990.40.1.103
[9] Richards, R., Elms, D. 1979. Seismic Behavior of Gravity Retaining Walls. J. Geotech Eng. 105(GT4), 449-464.
[10] Richards, R., Elms, D. 1990. Seismic Design of Retaining Walls. Proc. of ASCE Specialty Conf. on Design and Performance of Earth Retaining Structures, Geotechnical Special Publication 25, 854-871.
[11] Richards, R., Shi, X. 1994. Seismic lateral pressures in soils with cohesion. J. Geotech. Eng. 120, 7, 1230–1251. DOI: 10.1061/(ASCE)0733-9410(1994)120:7(1230)
[12] Velesos, A.S., Younan, A.H. 1994. Dynamic Modeling and Response of Soil-Wall Systems. J. Geotech. Eng. 120, 12, 2155-2179. DOI: 10.1061/(ASCE)0733-9410(1994)120:12(2155)
[13] Morrison, E.E., Ebeling, R.M. 1995. Limit equilibrium computation of dynamic passive earth pressure. Can. Geotech. J. 32, 481-487. DOI: 10.1139/t95-050
[14] Soubra, A.H. 2000. Static and seismic passive earth pressure coefficient on rigid retaining structures. Can. Geotech. J. 37, 463-478. DOI: 10.1139/t99-117
[15] Chen, Y. 2000. Practical analysis and design of mechanically-stabilized earth walls-I. Design philosophies and procedures Eng. Struct. 22, 7, 793-808. DOI: 10.1016/S0141-0296(99)00021-8
[16] Kumar, J. 2001. Seismic passive earth pressure coefficient for sands. Can. Geotech. J. 38, 876-881. DOI: 10.1139/t01-004
[17] Kumar, J., Chitikela, S. 2002. Seismic passive earth pressure coefficient using the method of characteristics. Can. Geotech. J. 39, 463-471. DOI: 10.1139/t01-103
[18] Green, R.A., Ebeling, R.M. 2002. Seismic analysis of cantilever retaining walls, Phase I. ERDC/ITL TR-02-3. Information technology laboratory, US army corps of engineers, Engineer research and development center, Vicksburg, MS.
[19] Saran, S., Gupta, R.P. 2003. Seismic Earth Pressure behind Retaining Walls. Indian. Geotech. J. 33, 3, 195-213.
[20] Cheng, Y.M. 2003. Seismic lateral earth pressure coefficients for C-φ soils by slip line method. J. Comput. Geotech. 30, 7, 661-670. DOI: 10.1016/j.compgeo.2003.07.003
[21] Yang, X.L, Yin, J.H. 2006. Estimation of seismic passive earth pressure with nonlinear failure criterion. Eng. Struct. 28, 342-348. DOI: 10.1016/j.engstruct.2005.08.007
[22] Choudhury, D., Nimbalkar, S.S. 2006. Psuedo-dynamic approach of seismic active earth pressure behind retaining wall. J. Geotech. Geolog. Eng. 24, 5, 1103-1113. DOI: 10.1007/s10706-005-1134-x
[23] Mylonakis, G., Kloukinas, P, Papatonopoulos, C. 2007. An alternative to the Mononobe-Okabe equation for seismic earth pressures. Soil. Dyn. Earthq. Eng. 27, 10, 957-969. DOI: 10.1016/j.soildyn. 2007.01.004
[24] Ghanbari, A, Ahmadabadi, M. 2010. Active earth pressure on inclined retaining walls in static and Psuedo-static condition. Int. J. Civil Eng. 8, 2, 159-172.
[25] Lambe, T.W., Whitman, R.V. 1979. Soil mechanics. SI version, Wiley, New York.
[26] Das, B.M. 1998. Principles of geotechnical engineering. Fourth Ed. PWS, Boston.

NAVODILA AVTORJEM

Vsebina članka

Članek naj bo napisan v naslednji obliki:

- Naslov, ki primerno opisuje vsebino članka in ne presega 80 znakov.
- Izvleček, ki naj bo skrajšana oblika članka in naj ne presega 250 besed. Izvleček mora vsebovati osnove, jedro in cilje raziskave, uporabljeno metodologijo dela, povzetek izidov in osnovne sklepe.
- Največ 6 ključnih besed, ki bi morale biti napisane takoj po izvlečku.
- Uvod, v katerem naj bo pregled novejšega stanja in zadostne informacije za razumevanje ter pregled izidov dela, predstavljenih v članku.
- Teorija.
- Eksperimentalni del, ki naj vsebuje podatke o postavitvi preiskusa in metode, uporabljene pri pridobitvi izidov.
- Izidi, ki naj bodo jasno prikazani, po potrebi v obliki slik in preglednic.
- Razprava, v kateri naj bodo prikazane povezave in posplošitve, uporabljene za pridobitev izidov. Prikazana naj bo tudi pomembnost izidov in primerjava s poprej objavljenimi deli.
- Sklepi, v katerih naj bo prikazan en ali več sklepov, ki izhajajo iz izidov in razprave.
- Vse navedbe v besedilu morajo biti na koncu zbrane v seznamu literature, in obratno.

Dodatne zahteve

- Vrstice morajo biti zaporedno oštevilčene.
- Predložen članek ne sme imeti več kot 18 strani (brez tabel, legend in literature); velikost črk 12, dvojni razmik med vrsticami. V članek je lahko vključenih največ 10 slik. Isti rezultati so lahko prikazani v tabelah ali na slikah, ne pa na oba načina.
- Potrebno je priložiti imena, naslove in elektronske naslove štirih potencialnih recenzentov članka. Urednik ima izključno pravico do odločitve, ali bo te predloge upošteval.

Enote in okrajšave

V besedilu, preglednicah in slikah uporabljajte le standardne označbe in okrajšave SI. Simbole fizikalnih veličin v besedilu pišite poševno (npr. *v*, *T* itn.). Simbole enot, ki so sestavljene iz črk, pa pokončno (npr. Pa, m itn.). Vse okrajšave naj bodo, ko se prvič pojavijo, izpisane v celoti.

Slike

Slike morajo biti zaporedno oštevilčene in označene, v besedilu in podnaslovu, kot sl. 1, sl. 2 itn. Posnete naj bodo v katerem koli od razširjenih formatov, npr. BMP, JPG, GIF. Za pripravo diagramov in risb priporočamo CDR format (CorelDraw), saj so slike v njem vektorske in jih lahko pri končni obdelavi preprosto povečujemo ali pomanjšujemo.

Pri označevanju osi v diagramih, kadar je le mogoče, uporabite označbe veličin (npr. *v*, *T* itn.). V diagramih z več krivuljami mora biti vsaka krivulja označena. Pomen oznake mora biti razložen v podnapisu slike.

Za vse slike po fotografskih posnetkih je treba priložiti izvirne fotografije ali kakovostno narejen posnetek.

Preglednice

Preglednice morajo biti zaporedno oštevilčene in označene, v besedilu in podnaslovu, kot preglednica 1, preglednica 2 itn. V preglednicah ne uporabljajte izpisanih imen veličin, ampak samo ustrezne simbole. K fizikalnim količinam, npr. *t* (pisano poševno), pripišite enote (pisano pokončno) v novo vrsto brez oklepajev. Vse opombe naj bodo označene z uporabo dvignjene številke[1].

Seznam literature

Navedba v besedilu

Vsaka navedba, na katero se sklicujete v besedilu, mora biti v seznamu literature (in obratno). Neobjavljeni rezultati in osebne komunikacije se ne priporočajo v seznamu literature, navedejo pa se lahko v besedilu, če je nujno potrebno.

Oblika navajanja literature

V besedilu: Navedite reference zaporedno po številkah v oglatih oklepajih v skladu z besedilom. Dejanski avtorji so lahko navedeni, vendar mora obvezno biti podana referenčna številka.

Primer: »..... kot je razvidno [1,2]. Brandl and Blovsky [4], sta pridobila drugačen rezultat…«

V seznamu: Literaturni viri so oštevilčeni po vrstnem redu, kakor se pojavijo v članku. Označimo jih s številkami v oglatih oklepajih.

Sklicevanje na objave v revijah:

[1] Jelušič, P., Žlender, B. 2013. Soil-nail wall stability analysis using ANFIS. Acta Geotechnica Slovenica 10(1), 61-73.

Sklicevanje na knjigo:
[2] Šuklje, L. 1969. Rheological aspects of soil mechanics. Wiley-Interscience, London
Sklicevanje na poglavje v monografiji:
[3] Mitchel, J.K. 1992. Characteristics and mechanisms of clay creep and creep rupture, in N. Guven, R.M. Pollastro (eds.), Clay-Water Interface and Its Rheological Implications, CMS Workshop Lectures, Vol. 4, The clay minerals Society, USA, pp. 212-244..
Sklicevanje na objave v zbornikih konferenc:
[4] Brandl, H., Blovsky, S. 2005. Slope stabilization with socket walls using the observational method. Proc. Int. conf. on Soil Mechanics and Geotechnical Engineering, Bratislava, pp. 2485-2488.
Sklicevanje na spletne objave:
[5] Kot najmanj, je potrebno podati celoten URL. Če so poznani drugi podatki (DOI, imena avtorjev, datumi, sklicevanje na izvorno literaturo), se naj prav tako dodajo.

Podatki o avtorjih

Članku priložite tudi podatke o avtorjih: imena, nazive, popolne poštne naslove, številke telefona in faksa, naslove elektronske pošte. Navedite kontaktno osebo.

Sprejem člankov in avtorske pravlce

Uredništvo si pridržuje pravico do odločanja o sprejemu članka za objavo, strokovno oceno mednarodnih recenzentov in morebitnem predlogu za krajšanje ali izpopolnitev ter terminološke in jezikovne korekture. Z objavo preidejo avtorske pravice na revijo ACTA GEOTECHNICA SLOVENICA. Pri morebitnih kasnejših objavah mora biti AGS navedena kot vir.

Vsa nadaljnja pojasnila daje:

Uredništvo
ACTA GEOTECHNICA SLOVENICA
Univerza v Mariboru,
Fakulteta za gradbeništvo, prometno inženirstvo in arhitekturo
Smetanova ulica 17, 2000 Maribor, Slovenija
E-pošta: ags@uni-mb.si

INSTRUCTIONS FOR AUTHORS

Format of the paper

The paper should have the following structure:

- A Title, which adequately describes the content of the paper and should not exceed 80 characters;
- An Abstract, which should be viewed as a mini version of the paper and should not exceed 250 words. The Abstract should state the principal objectives and the scope of the investigation and the methodology employed; it should also summarise the results and state the principal conclusions;
- Immediately after the abstract, provide a maximum of 6 keywords;
- An Introduction, which should provide a review of recent literature and sufficient background information to allow the results of the paper to be understood and evaluated;
- A Theoretical section;
- An Experimental section, which should provide details of the experimental set-up and the methods used to obtain the results;
- A Results section, which should clearly and concisely present the data, using figures and tables where appropriate;
- A Discussion section, which should describe the relationships shown and the generalisations made possible by the results and discuss the significance of the results, making comparisons with previously published work;
- Conclusions, which should present one or more conclusions that have been drawn from the results and subsequent discussion;
- A list of References, which comprises all the references cited in the text, and vice versa.

Additional Requirements for Manuscripts

- Use double line-spacing.
- Insert continuous line numbering.
- The submitted text of Research Papers should cover no more than 18 pages (without Tables, Legends, and References, style: font size 12, double line spacing). The number of illustrations should not exceed 10. Results may be shown in tables or figures, but not in both of them.
- Please submit, with the manuscript, the names, addresses and e-mail addresses of four potential referees. Note that the editor retains the sole right to decide whether or not the suggested reviewers are used.

Units and abbreviations

Only standard SI symbols and abbreviations should be used in the text, tables and figures. Symbols for physical quantities in the text should be written in Italics (e.g. *v*, *T*, etc.). Symbols for units that consist of letters should

be in plain text (e.g. Pa, m, etc.).
All abbreviations should be spelt out in full on first appearance.

Figures

Figures must be cited in consecutive numerical order in the text and referred to in both the text and the caption as Fig. 1, Fig. 2, etc. Figures may be saved in any common format, e.g. BMP, JPG, GIF. However, the use of CDR format (CorelDraw) is recommended for graphs and line drawings, since vector images can be easily reduced or enlarged during final processing of the paper.

When labelling axes, physical quantities (e.g. *v*, *T*, etc.) should be used whenever possible. Multi-curve graphs should have individual curves marked with a symbol; the meaning of the symbol should be explained in the figure caption. Good quality black-and-white photographs or scanned images should be supplied for the illustrations.

Tables

Tables must be cited in consecutive numerical order in the text and referred to in both the text and the caption as Table 1, Table 2, etc. The use of names for quantities in tables should be avoided if possible: corresponding symbols are preferred. In addition to the physical quantity, e.g. *t* (in Italics), units (normal text), should be added on a new line without brackets.
Any footnotes should be indicated by the use of the superscript[1].

LIST OF references

Citation in text

Please ensure that every reference cited in the text is also present in the reference list (and vice versa). Any references cited in the abstract must be given in full. Unpublished results and personal communications are not recommended in the reference list, but may be mentioned in the text, if necessary.

Reference style

Text: Indicate references by number(s) in square brackets consecutively in line with the text. The actual authors can be referred to, but the reference number(s) must always be given:

Example: "... as demonstrated [1,2]. Brandl and Blovsky [4] obtained a different result ..."

List: Number the references (numbers in square brackets) in the list in the order in which they appear in the text.

Reference to a journal publication:
[1] Jelušič, P., Žlender, B. 2013. Soil-nail wall stability analysis using ANFIS. Acta Geotechnica Slovenica 10(1), 61-73.

Reference to a book:
[2] Šuklje, L. 1969. Rheological aspects of soil mechanics. Wiley-Interscience, London

Reference to a chapter in an edited book:
[3] Mitchel, J.K. 1992. Characteristics and mechanisms of clay creep and creep rupture, in N. Guven, R.M. Pollastro (eds.), Clay-Water Interface and Its Rheological Implications, CMS Workshop Lectures, Vol. 4, The clay minerals Society, USA, pp. 212-244.

Conference proceedings:
[4] Brandl, H., Blovsky, S. 2005. Slope stabilization with socket walls using the observational method. Proc. Int. conf. on Soil Mechanics and Geotechnical Engineering, Bratislava, pp. 2485-2488.

Web references:
[5] As a minimum, the full URL should be given and the date when the reference was last accessed. Any further information, if known (DOI, author names, dates, reference to a source publication, etc.), should also be given.

Author information

The following information about the authors should be enclosed with the paper: names, complete postal addresses, telephone and fax numbers and E-mail addresses. Indicate the name of the corresponding author.

Acceptance of papers and copyright

The Editorial Committee of the Slovenian Geotechnical Review reserves the right to decide whether a paper is acceptable for publication, to obtain peer reviews for the submitted papers, and if necessary, to require changes in the content, length or language.
On publication, copyright for the paper shall pass to the ACTA GEOTECHNICA SLOVENICA. The AGS must be stated as a source in all later publication.

For further information contact:

Editorial Board
ACTA GEOTECHNICA SLOVENICA
University of Maribor,
Faculty of Civil Engineering, Transportation Engineering and Architecture
Smetanova ulica 17, 2000 Maribor, Slovenia
E-mail: ags@uni-mb.si

NAMEN REVIJE

Namen revije ACTA GEOTECHNICA SLOVENICA je objavljanje kakovostnih teoretičnih člankov z novih pomembnih področij geomehanike in geotehnike, ki bodo dolgoročno vplivali na temeljne in praktične vidike teh področij.

ACTA GEOTECHNICA SLOVENICA objavlja članke s področij: mehanika zemljin in kamnin, inženirska geologija, okoljska geotehnika, geosintetika, geotehnične konstrukcije, numerične in analitične metode, računalniško modeliranje, optimizacija geotehničnih konstrukcij, terenske in laboratorijske preiskave.

Revija redno izhaja dvakrat letno.

AIMS AND SCOPE

ACTA GEOTECHNICA SLOVENICA aims to play an important role in publishing high-quality, theoretical papers from important and emerging areas that will have a lasting impact on fundamental and practical aspects of geomechanics and geotechnical engineering.

ACTA GEOTECHNICA SLOVENICA publishes papers from the following areas: soil and rock mechanics, engineering geology, environmental geotechnics, geosynthetic, geotechnical structures, numerical and analytical methods, computer modelling, optimization of geotechnical structures, field and laboratory testing.

The journal is published twice a year.

AVTORSKE PRAVICE

COPYRIGHT

ODGOVORNOST

RESPONSIBILITY

www.fg.um.si

Univerza v Ljubljani

Fakulteta za gradbeništvo in geodezijo

Naravoslovnotehniška Fakulteta

www.fgg.uni-lj.si
www.ntf.uni-lj.si

www.sloged.si

www.ita-slovenia.si